University of Alberta

Molecular Separations Using Nanostructured Porous Thin Films Fabricated by Glancing Angle Deposition

by

Louis Wentzel Bezuidenhout

A thesis submitted to the Faculty of Graduate Studies and Research
in partial fulfillment of the requirements for the degree of

Doctor of Philosophy

in

Microsystems and Nanodevices

Department of Electrical and Computer Engineering

Spring 2011
Edmonton, Alberta

To my partner and best friend.

ABSTRACT

Biomolecular separation techniques are an enabling technology that indirectly influence many aspects of our lives. Advances have led to faster analyses, reduced costs, higher specificity, and new analytical techniques, impacting areas such as health care, environmental monitoring, polymer sciences, agriculture, and nutrition. Further development of separations technology is anticipated to follow the path of computing technology such that miniaturization through the development of microfluidics technology, lab-on-a-chip systems, and other integrative, multi-component systems will further extend our analysis capabilities.

Creation of new and improvement of existing separation technologies is an integral part of the pathway to miniaturized systems. The work of this thesis investigates molecular separations using porous nanostructured films fabricated by the thin film process glancing angle deposition (GLAD). Structural architecture, pore size and shape, and film density can be finely controlled to produce high-surface area thin films with engineered morphology. The characteristic size scales and structural control of GLAD films are well-suited to biomolecules and separation techniques, motivating investigation into the utility and performance of GLAD films for biomolecular separations.

This project consisted of three phases. First, chromatographic separation of dye molecules on silica GLAD films was demonstrated by thin layer chromatography.

Direct control of film nanostructure altered the separation characteristics; most strikingly, anisotropic structures provided two-dimensional analyte migration. Second, nanostructures made with GLAD were integrated in PDMS microfluidic channels using a sacrificial etching process; DNA molecules (10/48 kbp and 6/10/20 kbp mixtures) were electrophoretically separated on a microfluidic chip using a porous bed of SiO_2 vertical posts. Third, mass spectrometry of proteins and drugs in the mass range of 100-1300 *m/z* was performed using laser desorption/ionization (LDI) on silicon GLAD films, and the influence of film thickness, porosity, structure, and substrate on performance was characterized.

The application of GLAD nanostructured thin films to biomolecular separations is demonstrated and validated in this thesis. Chromatographic separation of dye molecules, electrophoretic separation of DNA molecules, and mass spectrometric isolation of small proteins and drug molecules by laser desorption ionization were demonstrated using GLAD films. All three methods yielded promising results and establish GLAD as a potential technology for biomolecular separations.

ACKNOWLEDGEMENTS

There are many people without whom this work would never have happened, or without whom I'd never have made it this far.

First I'd like to thank those who were directly involved with the work of my graduate studies. I had the great fortune to work with three pioneers in their respective, now well-established fields. First Dr. Michael J. Brett (glancing angle deposition), then Dr. Michael T. Taschuk (motivational fist-shaking and finger-pointing) and later Dr. D. Jed Harrison (microfluidics).

Mike Brett has built a fantastic working environment, with excellent people, funding, and equipment, giving us the freedom and confidence to focus on the research. He is the prototype of what a supervisor and principal investigator should be, and I thank him for the opportunity to work in his lab, for everything that entailed, and for everything he has done for me.

I don't know if I can properly thank Mike Taschuk without embarrasing him, and that's probably how he would want it. I don't know how I would've finished this without him – you can't really understand until you've experienced it. Thanks also to Dr. Jeremy Sit for his mentorship, guidance, support and also the use of his lab.

Much of my work depended on the strong collaboration formed with Abebaw Jemere and Neda Nazemifard. Without their work, ideas, motivation and discussions, I probably wouldn't have a thesis to write an acknowledgement for, so you can thank or curse them for that. Implicit in their and my work is Jed Harrison's support and advice and the use of his lab. I also want to thank Dr. Gerda Morlock for the opportunity to collaborate with her group.

Steven Jim has taken a project I started and transformed it into something I never dreamed of (and wouldn't be capable of if I had). I thank him for his support and the many debates and discussions we had regarding work and other very very important matters. Martin Kupsta, Katie Krause, and Jaron Van Dijken all helped

take critical SEM images and provided valuable discussions and data regarding my work, and along with Steve showed me what it means to work your ass off. George Braybrook and De-ann Rollings spent many hours with me taking excellent images while providing a friendly ear – I think the pretty pictures are the best part of this thesis. Mike Fleischauer's mentorship guided me many times along the way. Thanks also to Ben Bathgate for his expertise when things needed finding or fixing, and to Audrey Lin and Karen Hayward for keeping the lab operational.

I'm indebted to the entire NanoFab staff: Jeanine Autio, Stephanie Bozic, Bob Brebber, Jolene Chorzempa, Glenn Elaschuk, Eric Flaim, Keith Franklin, Melissa Hawrelechko, Michael Hume, Scott Munro, Les Schowalter, and Ken Westra. We have an excellent facility – with expert training and maintenance – that was essential to my research and I was privileged to be able to use it.

Someone had to pay for this work, and I am extremely grateful to the organizations who did: the Natural Sciences and Engineering Research Council of Canada, Alberta Innovates Technology Futures (formerly known as the Alberta Ingenuity Fund), the Informatics Circle of Research Excellence, Micralyne Inc., the Province of Alberta, and the University of Alberta.

Next I'd like to thank the 'supporting cast', the talented group of students in the lab who were along for the ride and whose friendship helped make the journey that much more enjoyable (in order of highest to lowest Scrabble score for their full names): Jaron, Matt, Nick, Josh K., Jon, James, Josh L., Jeff, Josh S., Mike Th., Andy, Mark, Sumudu, Steve, John, Martin, Ryan, Katie, Jason, Doug, Graeme, and Al.

Last but not the least, I'd like to thank those who may not have been in the lab, but helped get me to where I am. I treasure the many good times with friends and with the in-laws – Boris, Chris, Dan, Ben, and Becky – and am looking forward to many more.

Thanks to my parents, Andrea and Johan, who sacrificed so much to give their sons better opportunities in life, and also to my brothers Hannes and Daniel, for their constant love and support. Finally, thanks to Jacquie for her friendship, love, companionship, understanding, and support. This is the end of one exciting chapter and the beginning of another.

And of course, thanks to you, the reader! Best to put this down now while you're still ahead.

CONTENTS

LIST OF TABLES

LIST OF FIGURES

LIST OF ACRONYMS

A-NS	'Anisotropic' nanostructure ultrathin-layer chromatography
ACTH	Adrenocorticotropic hormone
ALD	Atomic layer deposition
CC	Cross-channel
DIOS	Desorption/ionization on silicon
DNA	Deoxyribonucleic acid
FMN	Flavin mononucleotide
GLAD	Glancing angle deposition
HPTLC	High performance thin layer chromatography
IC	In-channel
LDI	Laser desorption/ionization
LISMA	Laser-induced silicon microcolumn arrays
MALDI	Matrix-assisted laser desorption/ionization
MFP	Mean free path
MS	Mass spectrometry
NS-UTLC	Nanostructure ultrathin-layer chromatography
PDMS	Polydimethyl siloxane
PECVD	Plasma enhanced chemical vapor deposition
PVD	Physical vapor deposition
RIE	Reactive ion etching

S-NS	'Superimposed' nanostructure ultrathin-layer chromatography
SALDI	Surface-assisted laser desorption/ionization
SEM	Scanning electron microscope
TBE	Tris-borate ethylenediamine tetra-acetic acid buffer
TIRF	Total internal reflection fluorescence
TLC	Thin layer chromatography
TOF	Time-of-flight
UTLC	Ultrathin-layer chromatography
UV-O	Ultraviolet ozone

1 INTRODUCTION

The last few decades have witnessed tremendous growth in the field of biology, driven in part by new analysis technologies to help decipher and understand biomolecules such as DNA and proteins. Many of these technological advances have been made in the separation sciences, which address the problem of separating a mixture of compounds for any combination of end goals: isolation, purification, or identification. This invariably involves leveraging some combination of physical and chemical properties that distinguishes the components.

The Human Genome Project is demonstrative of these advances. The first full sequence was completed in 2003, revealing the code of human life in its entirety for the first time [1,2]. This marks an important step in our quest to better understand the human body; such understanding may help identify, treat, and cure many diseases that afflict the population. The separation of DNA molecules by size using capillary array electrophoresis was an essential element in the original sequencing effort, and advances in this area were instrumental to the project finishing two years early at a much lower cost than anticipated [3].

Molecular separation is a critical and enabling technology that extends beyond

biomolecular analysis. In industry, chemicals are separated to isolate and purify them for manufacturing processes; the products are separated and analyzed for quality and process optimization. Food producers use separations to monitor product content and quality. Pharmaceutical companies use separations on a large scale to isolate drugs during production and on a small scale to analyze the purity and efficiency of their processes. Forensic scientists use separations to isolate DNA from bodily fluids to help identify and incriminate suspects.

The advent of microfluidics has spurred a revolution in separation technology over the last two decades. In the broadest sense, microfluidics encompasses any system that manipulates fluids on a microscale, not necessarily through micron-sized fluidic channels. Shrinking the fluidic system down to the microscale has numerous benefits, including faster separation with higher efficiency, better resolving power, sensitive on-line detection methods, lower reagent use, and multi-process integration onto one device [4–9].

Engineered structure integration into microchannels for microfluidic separations has been actively investigated in recent years. Fabrication of such structures by micro- and nano-fabrication techniques permits control over the separating media by engineering the microstructure morphology and material along with the pore morphology, distribution and size [10,11]. This in turn has enabled a number of advances in the field, including better theoretical understanding of separation mechanisms and access to

new separation mechanisms along with the usual benefits of microfluidic integration: faster separations, higher sensitivity, and lower reagent volumes.

Miniaturization has provided advances in planar separations as well. Thin layer chromatography (TLC) is a fundamental chromatographic technique. Chemical compounds are separated during transit via capillary action through a porous film as a result of differing film-compound interactions. Thinner layers with finer particles of narrower size distribution decrease separation times, increase resolution and sensitivity, and reduce reagent consumption [12].

Molecular separations are often followed by mass spectrometry to analyze and identify the separated analytes. In addition to molecular separations, nanostructured materials have also proven advantageous in mass spectrometry. Direct laser interaction with nanostructures enables non-fragmenting laser desorption/ionization (LDI) of molecules from a target for subsequent insertion into a mass spectrometer, without the use of an intermediate matrix. This allows for detection of very low mass fragments that are usually obscured by the matrix ions, as well as the possibility of detecting very large fragments.

Glancing angle deposition (GLAD) is a powerful, elegant technique for fabricating nanostructures with engineered morphology, architecture, and porosity onto any flat substrate. The ability to finely tune the nanostructures along with a wide nanostructure and substrate selection makes GLAD a promising candidate for fabricating

nanostructures for analytical applications such as molecular separations and mass spectrometry. Chapter 2 provides a brief overview of the glancing angle deposition technique.

This thesis reports the investigation of GLAD films applied to biomolecular separations. Three areas were identified where GLAD nanostructured thin films could potentially provide unique benefits over existing technologies: electrophoretic separations, chromatographic separations, and laser desorption/ionization mass spectrometry.

The planar format and relatively simple experimental setup of TLC separations provided an attractive proof-of-concept that GLAD structures are viable as a chromatographic stationary phase. Chapter 3 describes how GLAD films were successfully applied as a TLC stationary phase, and the interesting anisotropic properties that arose as a result of engineered film morphology.

Miniaturization of separation methods has been a strong focus of research activity over the last two decades, as discussed above, motivated by the increased performance, decreased costs, and novel technologies associated with microfluidic systems. This potential, combined with successful TLC separations and the influence of anisotropic structures on these separations, motivated the integration of arbitrary GLAD structures into microfluidic channels and is discussed in Chapter 4. A technique for fabricating devices with GLAD-filled channels is discussed, and separation of DNA strands (5-48kbp) demonstrates the successful fabrication of a GLAD-based

microfluidic biomolecular separation device.

The ability to deposit porous silicon films similar to those used in desorption/ionization on silicon (DIOS) mass spectrometry made GLAD films a natural candidate for application to laser desorption/ionization. This was further motivated by the possibility of improving LDI performance through a combination of structural and material optimization. Chapter 5 discusses the performance of silicon GLAD films for DIOS. Film architecture and density were both found to have a significant impact on signal strength; very high sensitivities relative to existing LDI matrices were obtained with silicon GLAD films.

Concluding remarks and possible future directions for this work are given in Chapter 6.

GLANCING ANGLE DEPOSITION 2

Glancing angle deposition (GLAD) is a single-step, bottom-up nanofabrication tool used to engineer nano-columns with controllable architecture. A variety of nanostructures can be made by combining physical vapor deposition onto a flat substrate held at an angle to the vapor with computer-controlled biaxial substrate rotation. Materials suitable for GLAD films include insulators (e.g., SiO_2, Al_2O_3, TiO_x, MgF), semiconductors (e.g., Si, Ge), metals (e.g., Ti, Cu, Al, Pt), and organic materials (e.g., Alq_3, Znq_2, CuPc) [13]. The GLAD process was developed by our group at the University of Alberta [14, 15].

2.1 GLAD Film Growth

GLAD film structures are tailored on nanometer scales by manipulating self-shadowing effects that arise when vapor flux arrives at highly oblique angles during physical vapor deposition. The following is an introductory discussion intended to provide a rudimentary understanding of how the growth of GLAD films is possible.

2.1.1 Thin Film Growth

Physical vapor deposition (PVD) coats substrates with a thin film of material through condensation of atoms arriving from a vapor source. Vaporized atoms collide with the substrate and adsorb on the surface, where they either find a resting place or desorb. Film structure is determined in part by the energies of adsorbed atoms (adatoms) on the substrate surface when deposited at normal incidence angles, where incoming atomic flux is normal to the substrate surface. The structure also depends on the substrate energy, an effect that has been well-characterized by the Movchan & Demchishin zone model [16], which relates film structure to the ratio of substrate temperature to material melting point (T/T_M) (ref. Fig. 2.1). Substrate and adatom energy are related since adsorbing atoms transfer kinetic and thermal energy to the substrate.

Three distinct film structure types form, separated by boundaries at T/T_M of 0.3 and 0.5. The structures consist of well-defined, individual columns in the first zone ($T/T_M < 0.3$); it is this zone that encompasses the lower energy range typical of evaporation (0.1-0.5 eV) and sputtering (10-50 eV) onto unheated substrates [17]. Atoms arriving and adsorbing on the substrate are initially mobile, finding a final resting place at low energy sites. At these low energies, initial adatom mobility is low, and as a result, initial film growth occurs as an "islanding" process, where individual

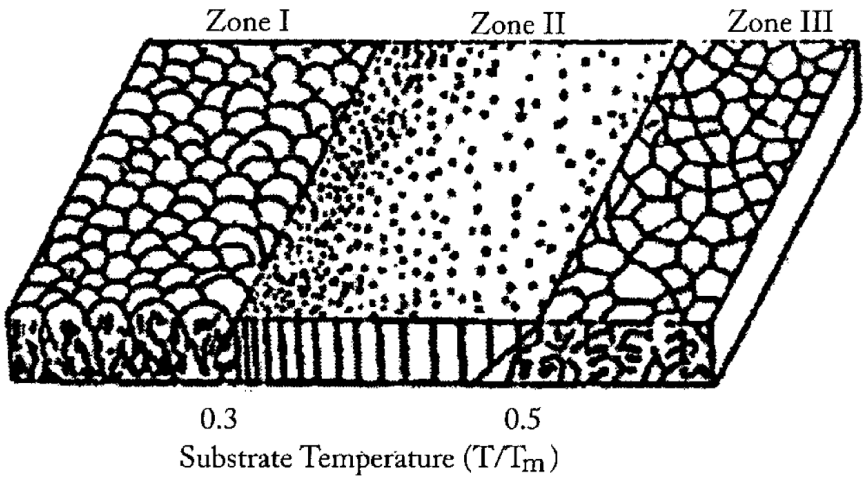

Figure 2.1: Movchan & Demchishin zone model of evaporated thin film growth, relating film nanostructure to the substrate temperature. Reprinted with permission from [16]. © 2010 Annual Reviews, Inc.

clusters of atoms accumulate at randomly-located sites over the surface topology, rather than through formation of a smooth solid layer. The adatom mobility is determined by a number of factors, including initial energy acquired by the atom in the vaporization process, substrate temperature, and substrate topology. As more atoms arrive at the substrate, the nuclei grow in size, until they coalesce to form a solid film. The coalescence is not perfect, however, and there is a boundary that forms as individual nuclei grow against each other, causing the solid defected columnar structure typical of Zone I evaporated and sputtered films. This boundary is the result of low adatom mobility which favors growth at the top of the islands where a majority of the flux is captured and where atoms can settle in a low energy state, as opposed to adatom diffusion away from the islands to areas where there is a lower

concentration of source atoms but higher energy between substrate and atoms. Low adatom diffusion (i.e. Zone I growth) is critical for GLAD structure formation.

Growth in the second zone ($0.3 < T/T_M < 0.5$) is characterized by finer, less defined columns in conjunction with increasing grain sizes relative to Zone I growth, as a consequence of increased adatom surface diffusion. In Zone III ($T/T_M > 0.5$), bulk diffusion is dominant and film growth is dense, crystalline, and characterized by large grains and disappearance of the columnar morphology witnessed in the first two zones. Zone II and III growth occur outside the range of substrate to melting point temperature ratios typically seen in glancing angle deposition, and consequently are not of interest in this work.

Evaporation and sputtering are the most common methods for depositing GLAD films. The films in this thesis were deposited exclusively by evaporation. With evaporation, the target material to be deposited is heated by resistive heating (thermal evaporation), or by transfer of energy from an impinging high-energy electron beam (electron beam evaporation). At sufficient temperatures, some materials will melt while others will sublimate. In both cases, atoms are ejected from the source material; barring collisions with other source atoms or residual gas, these atoms will travel ballistically (line-of-sight) to the substrate where they are adsorbed and integrated in the growing film.

A high vacuum environment is critical in this process for a number of reasons,

including:

- Molecules released from the source surface will travel ballistically until they collide with other molecules that force them from this path, or with some surface where they lose sufficient energy to adsorb to the surface without subsequent desorption. Collisions with other molecules cause target molecules to arrive at the substrate at a variety of angles and energies. This is not necessarily an issue when depositing a solid thin film, provided the molecules arriving at the substrate have sufficient energy to produce the desired film structure as described by the zone model. With GLAD, however, collimation of the incoming molecules is essential to proper film growth, necessitating the use of high vacuum chambers for film deposition. The higher the vacuum, the fewer molecules are present to collide with and scatter released target molecules as they travel toward the substrate. Pressures below $\sim 10^{-5}$ Torr are sufficient for GLAD, as the mean distance travelled between collisions (mean free path, MFP) is greater than a meter and thus exceeds the deposition chamber dimensions [17]. The requirement for a long MFP will become clear when GLAD film growth is discussed in Section 2.1.2.

- Residual gas molecules (constituting the system base pressure) can collide with the substrate, where they may be integrated in the film as impurities. The rate at which such impurities deposit on the film is directly related to the number

of molecules, and thus pressure, present in the system. The higher the vacuum, the purer the deposited film will be.

2.1.2 GLAD Thin Film Growth

The nanostructures grown with GLAD arise when the substrate is tilted relative to the source flux (Fig. 2.2). As with deposition onto a substrate held normal to the flux, atoms cluster together at low-energy nucleation sites during early stages of film growth. At oblique incidence angles, ballistic deposition causes these clusters to shadow the substrate from incoming molecules. Consequently, the molecules preferentially deposit on the nuclei's upper surface, with preference towards the side nearest to the flux. Adatom diffusion is low, and the film grows as tightly-packed columns, tilted towards the incoming atomic flux at an angle between the vapor arrival angle and the substrate normal, β (see Figure 2.2) [18]. At large deposition angles ($>\sim 80°$) the film grows as distinct separate columns tens to hundreds of nanometers in diameter, with the spacing and column diameter increasing with deposition angle [19]. This increase in spacing and column diameter is a direct result of the larger shadows cast by nuclei at larger deposition angles. The density and porosity of the growing film can thus be manipulated by tilting the substrate during deposition [19, 20]. Figure 2.3a shows an example of such a slanted post GLAD film.

Biaxial control of the substrate provides the ability to sculpt the growing columns

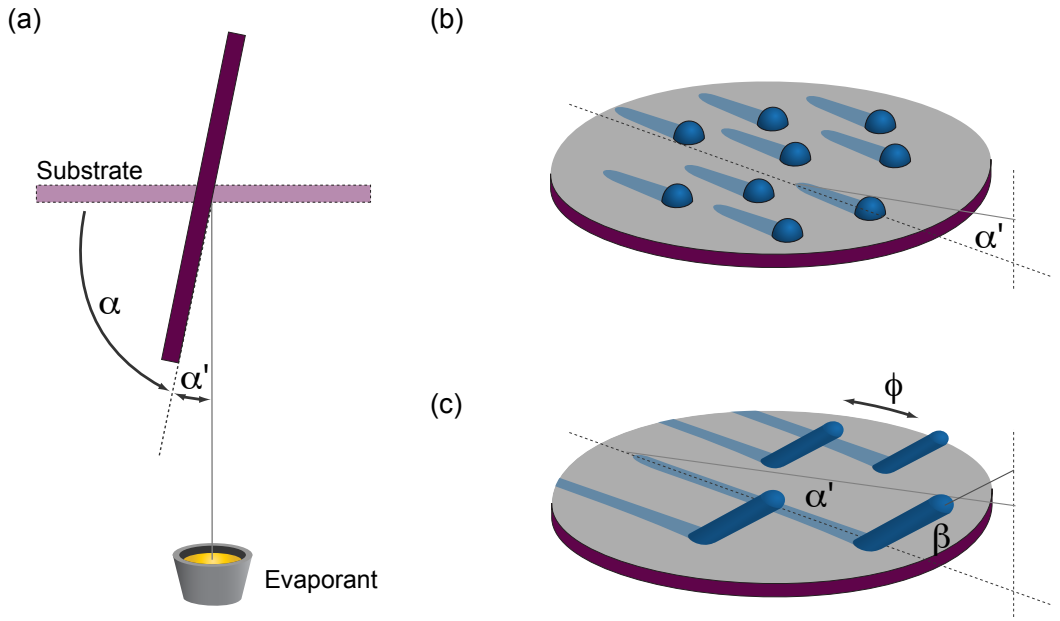

Figure 2.2: (a) In glancing angle deposition, the substrate is tilted so that the incoming atomic flux arrives at an oblique angle, α, to the substrate normal. (b) Nuclei that form during initial film growth cast shadows that lead to preferential nuclei growth and extinction. (c) As the film grows, individual columns form, tilted at an angle β relative to the substrate normal, which can be shaped by rotating the film around the substrate normal, ϕ. Nuclei and columns shown are exaggerated and not to scale.

into more complex shapes than slanted posts as they grow. Since the columns always grow towards the incoming flux of atoms, the column architecture can be manipulated by rotating the substrate around its normal axis, ϕ. This substrate reorientation to the incoming flux will alter the direction of column growth. As an example, rotating ϕ at a constant rate will produce helices when rotated slowly (Fig. 2.3e) and vertical posts when rotated at a faster rate (Fig. 2.3b); rotating ϕ discreetly in 60° or 180° increments will produce hexagonal spiral staircase and chevron (zig-zag) films, respectively (Figs. 2.3 c and d).

The substrate tilt can also be changed during film growth to change the density and porosity along the height of the columns. Figure 2.3f shows a porous film (hexagonal spiral) capped by a solid layer. The cap is formed by slowly rotating α to normal towards the end of the deposition, resulting in densification of the growing film until a solid layer forms when α reaches 0°. Simultaneous control of ϕ and α during film growth provides a wide spectrum of possible architectures.

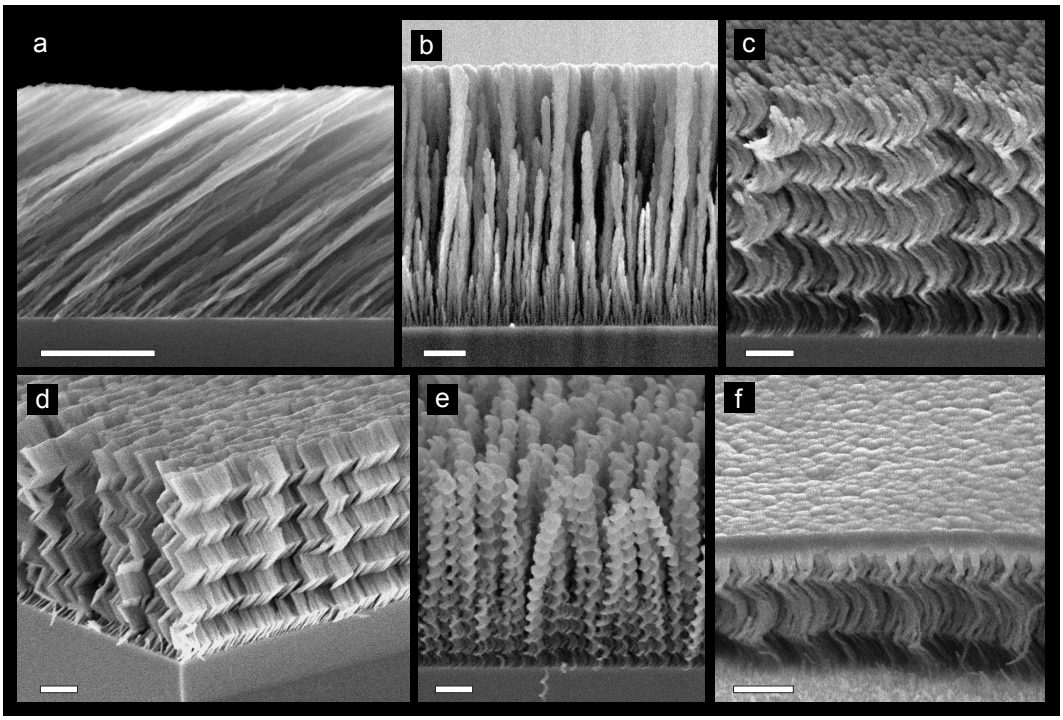

Figure 2.3: A representative sampling of structures that can be made with GLAD: (a) Si slanted posts, (b) Si vertical posts, (c) SiO_2 hexagonal spirals, (d) SiO_2 chevrons, (e) SiO_2 helices, and (f) an SiO_2 hexagonal spiral film with a solid cap. Scale bars indicate 250 nm for (a) and 1 μm for (b)–(f).

GLAD Deposition System

The fine control over film structure achievable with GLAD is possible due to a computerized feedback system that controls two stepper motors which move the substrate through α and ϕ. Film growth, and hence column height, is monitored during deposition by measuring the deposition rate using a quartz-crystal microbalance. This rate is fed into a software program that moves the substrate according to a pre-written deposition profile specifying the desired changes in α and ϕ along the height of the columns. The GLAD structures used for the work in this thesis were deposited in a custom-built deposition chamber, shown in Figure 2.4.

The self-shadowing required for GLAD film growth also necessitates collimation of atoms arriving at the substrate. This makes GLAD film growth more reliable in evaporation systems than in sputtering systems – sputtering requires higher pressures to maintain a plasma discharge, and hence more scattering, for proper operation. A few strategies are used in GLAD systems to collimate atoms arriving at the substrate. The simplest method is to use long-throw deposition where the substrate is located far enough from the source material that the solid angle occupied by the substrate (and hence the angular distribution of incident particles) is reduced. This technique works well with high vacuum conditions, although deposition rates and efficient material use are reduced. The system in Figure 2.4 had a substrate-source separation of 45 cm.

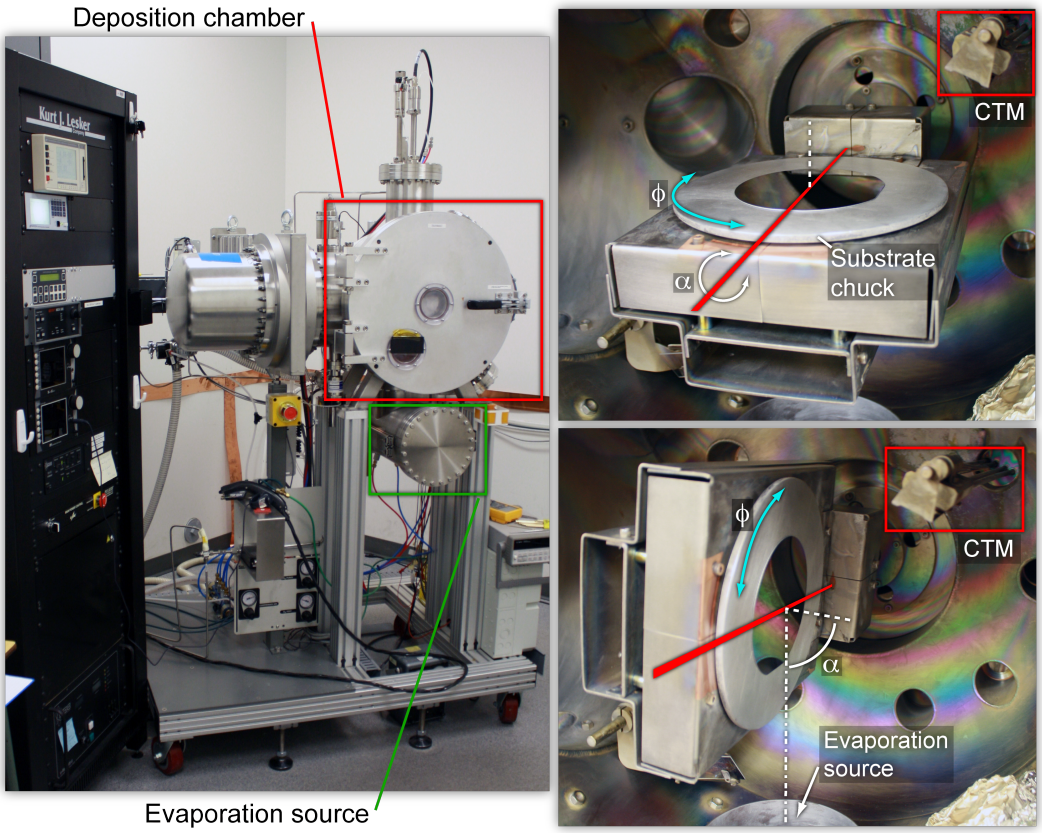

Figure 2.4: High vacuum deposition system with biaxial substrate position control and crystal thickness monitor for depositing GLAD films.

2.1.3 Advanced GLAD Film Growth

PhiSweep

GLAD structures will broaden while growing [21, 22]. For example, vertical posts grow fatter (larger diameter) with increasing height, while slanted posts fan out (grow wider) during growth. This expansion in structural dimensions with film height has been explicitly studied in vertical post films, and has been described as power-law

growth [13], due to the power-law relation between column height h and width w: $w \propto h^{p(\alpha)}$. This broadening is a result of geometric self-shadowing on each growing column, further aggravated by non-ideal collimation of incoming atoms [23–25]. During slanted post growth, columns are shadowed from incoming flux by those nearer to the source. This shadowing causes broadening in a direction perpendicular to the flux, as there is no shadowing in that direction. As a result, the columns fan out during growth. During vertical post growth, a similar effect combined with continuous substrate rotation causes widening of growing pillars.

All traditional GLAD structures can be described as some assembly of vertical post and/or slanted post segments, and consequently all are subject to column broadening with increasing height. This broadening can be reduced in the slanted post component of films using the PhiSweep technique [18, 26]. Slanted post segments are traditionally grown with the substrate held stationary at some fixed angle ϕ, with the slanted post growing towards the vapor source. For example, one rotation of a square spiral is grown by stacking four slanted post segments on top of one another, with ϕ held at 0°, 90°, 180°, and 270° for each subsequent segment.

PhiSweep superimposes a subtle oscillation over each fixed segment held at angle ϕ by sweeping out an angle γ on either side of ϕ [18]. Consecutive short segments of height z are grown at equal angular offsets of $\phi + \gamma$ and $\phi - \gamma$, with a quick sweep between the two offsets. The net columnar growth direction remains the same as if the

substrate were held stationary, but the structure does not. Continuous reorientation of the substrate reduces broadening by introducing shadowing perpendicular to the deposition plane. This 'resets' the broadening of each segment as the reoriented columns cast a shadow on adjacent columns and effectively expose a new smaller surface area face to the incoming vapor. The lateral broadening of traditional slanted posts is diminished as a result. Optimal conditions for limiting broadening with PhiSweep are structure- and material-dependent, but z is typically selected in the low tens of nanometers and γ typically ranges between 15° and 45°.

Substrate Seeding

GLAD films deposited onto bare substrates grow as randomly distributed columns. Spatial arrangement of GLAD columns on the substrate can be predetermined by deposition onto topographic features such as bumps, referred to as 'seeds' that are patterned on the substrate prior to deposition [13, 27, 28]. Seeds selectively capture incoming vapor flux by shadowing the substrate during initial film growth, localizing columnar growth to sites predetermined by seed location. As a result, column growth locations can be fixed by purposeful patterning of substrates prior to deposition. This substrate seeding can be used to create ordered, regularly spaced arrays of GLAD structures over a large area. Seeded GLAD structures also tend to be more uniform in size and diameter than unseeded structures. Figure 2.5(a) shows a square spiral film

fabricated by deposition of Si onto a regularly spaced array of seeds, creating an array of regularly-spaced columns in the seeded region, and an adjacent irregularly-spaced GLAD film in the non-seeded region. Figure 2.5(b) shows another square spiral film, deposited with PhiSweep to create a very uniform array of GLAD structures. Seed distribution, size, and geometry have to be carefully designed to satisfy shadowing and column architecture requirements [28]. For example, if the seeds are spaced too far apart, the inter-seed space will not be completely shadowed and additional columns will grow in between the seeds. If the seeds are too wide, multiple columns will grow on each seed.

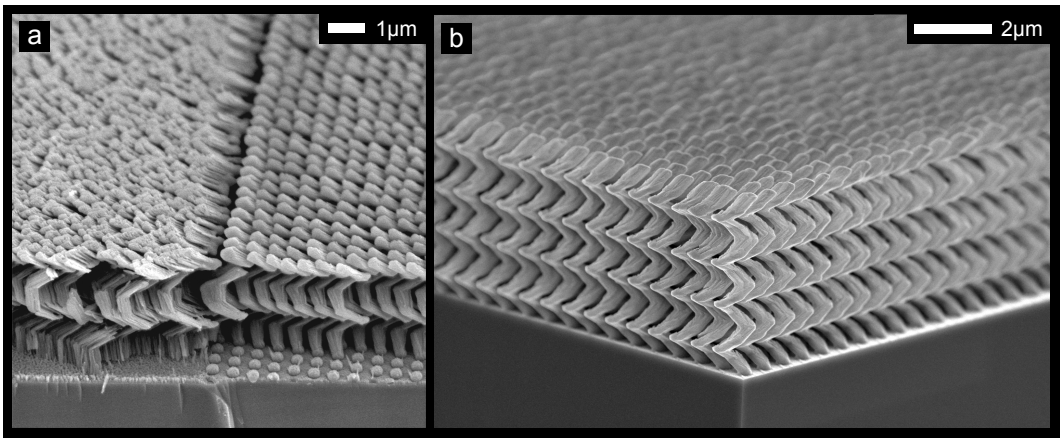

Figure 2.5: Substrate seeding is used to create arrays of GLAD posts with predesigned spatial location on the substrate. (a) The transition in film structure and orientation between seeded (right) and unseeded (left) substrate regions is clear in this scanning electron micrograph. (b) Substrate seeding combined with PhiSweep to create a thick GLAD film with uniform, regularly spaced square spirals. Reprinted from (a) [29] and (b) [30] with kind permission from the authors.

2.2 Applications of GLAD Films

The wide array of possible structures and materials that can be engineered at a nanometer scale with GLAD and the subsequent ability to tune film properties through control over film density and morphology has made the technology attractive for applications in a variety of fields. The design and applications of GLAD films have been well-documented in recent reviews and texts [13, 20, 31–33].

As examples, the optical properties of GLAD films may be controlled by varying the film density, film thickness and growth orientation [20, 34]; this has been applied to make gradient index optical filters [35], high-speed humidity sensors [36] and photonic band gap crystals [37]. Porous GLAD films can be engineered to create highly-insulating thermal barrier coatings [38], high-density capacitors [39] and surfaces for catalysis of hydrocarbon oxidation [40]. The rough surface and material selection of GLAD has motivated cell and protein adhesion studies on platinum [41] and parylene [42] GLAD structures.

Their high surface area along with optimizable structures and materials make GLAD films particularly suited for sensing applications. Vapors such as water [43] and hydrocarbons [40] are detectable with GLAD metal oxide and platinum films, respectively. The high porosity and surface areas produce a very sensitive and rapid response to target molecules. Localized surface plasmon resonance on silver [44]

and gold and multilayer [45] nanoparticles fabricated with GLAD has been used for specific detection of biomolecules such as immunoglobulins in solution. Respiratory virus signatures [46] and bacteria [47,48] have also been sensed with GLAD-fabricated films.

3 THIN LAYER CHROMATOGRAPHY[1]

3.1 Introduction

Thin layer chromatography (TLC) is a well established planar chromatographic technique, with diverse applications including identification of drugs and toxic substances in biological fluids, monitoring water supplies for pesticides, analysis of pharmaceutical products, and evaluation of the flavor potential of plant materials [50].

3.1.1 Thin Layer Chromatography

Thin layer chromatography is a subset of the larger separation science field of chromatography [51]. In its most general form, chromatography separates a mixture of molecules (analytes) in one phase based on their differing physical/chemical interactions with another phase. For example, in liquid chromatography the molecules are dissolved in a liquid phase that moves over and/or through a solid phase. Differing affinities of each analyte for the solid and liquid phase results in diferent rates of transit through the solid phase, resolving the analytes both spatially and temporally.

In TLC, the analytes and liquid phase are moved through a solid phase via capillary

[1] A version of this chapter has been published in Ref. [49].

action. Distinct terminology is used to distinguish the two phases. The solid phase remains immobile during the separation and is referred to as the *stationary phase*. A TLC plate consists of a substrate (e.g. glass, aluminum, plastic) coated with the stationary phase, a thin porous layer. The *mobile phase* contains the mixture to be separated and is capillary-driven, moving through the stationary phase during the separation. Solvated analytes are applied along the bottom of the TLC plate as small spots and allowed to dry. The bottom of the plate is immersed in the mobile phase without submerging the analyte spots. This allows the mobile phase to wick up the plate by capillary action, dissolving and carrying along the analytes.

Each analyte in the mixture will have some affinity for the mobile phase and some affinity for the stationary phase; the ratio of these affinities differ for each analyte, depending on the nature of the mobile and stationary phases. As the mixture of analytes move up the plate, the analytes migrate at different rates based on these affinities – more retained analytes have higher relative affinity for the stationary phase and lag behind less retained analytes. Consequently, the analytes are separated into distinct spots or bands on the TLC plate. When the analytes are more easily dissolved in a polar solution, a polar stationary phase (hydrophilic) is used – this is normal phase TLC. In reversed phase TLC, the analytes are more easily dissolved in a non-polar solution, and the stationary phase is more non-polar (hydrophobic).

Normal phase silica gel is the best established and most widely used stationary

phase, with little modification since TLC's origins in 1956 [12, 52]. The most significant change came in the 1970s with the introduction of High Performance TLC (HPTLC) plates. Compared to TLC plates, HPTLC plates have thinner layers containing finer particles with a smaller size distribution, providing shorter migration distances, faster separations, and lower reagent and solvent consumption [12, 52].

3.1.2 Ultrathin-layer Chromatography

Ultrathin-layer chromatographic (UTLC) plates were introduced in 2001 to improve on the performance of TLC and HPTLC plates [53, 54]. UTLC plates are made by coating a glass substrate with a monolithic silica gel, creating a 10 μm thick sorbent layer characterized by 1 μm - 2 μm macropores and 3 nm - 4 nm mesopores. Figure 3.1 shows the structure of such a layer (UTLC Glass Plate, Merck KGaA, Darmstadt, Germany). Separations on UTLC plates are faster and require smaller reagent and sample volumes than HPTLC and TLC. In most cases, UTLC plates have a lower limit of detection; however, they also exhibit lower resolution due to shorter development lengths and lower available specific surface area [54]. UTLC plates have been shown to provide a better interface in coupled TLC-mass spectrometry, where the thinner adsorbent layer on UTLC plates improved the sensitity of TLC atmospheric pressure matrix-assisted laser desorption ionization mass spectrometry (TLC-MALDI-MS) by 10-100 times over HPTLC plates [55].

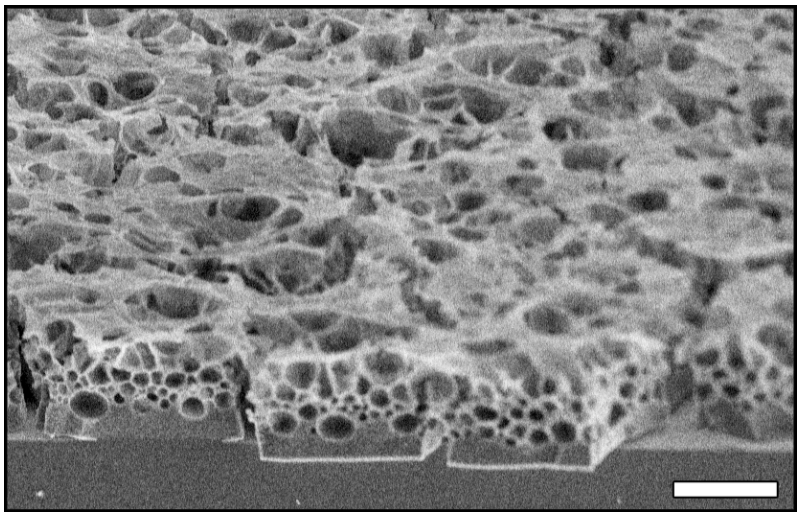

Figure 3.1: Scanning electron micrograph of a commercial ultrathin-layer chromatography plate stationary phase. Scale bar indicates 10 μm.

It is well established that the porosity of TLC plates has a direct impact on their performance characteristics [50, 52]. The ability to engineer film porosity and nanostructure coupled with the proven benefits of plate miniaturization makes GLAD films a promising candidate to produce better performing UTLC plates. Nanostructured SiO_2 UTLC (NS-UTLC) plates were fabricated to investigate TLC separations on GLAD films. The ability of silica nanostructured thin films to act as a stationary phase for TLC is demonstrated qualitatively using a standard dye mixture. Furthermore, it is demonstrated that altering the nanostructure architecture will change the separaration characteristics of the silica layer, and that an anisotropic film has different characteristics depending on the direction of development on the plate relative to the anisotropic structures.

3.2 Experimental

3.2.1 TLC Plate Fabrication

In our initial study, two types of NS-UTLC plates with different nanostructures were fabricated. All films were made by depositing SiO_2 (99.99% pure, Cerac Inc.) onto 1" square glass substrates (Schott B270, S.I. Howard Glass) by electron-beam evaporation using GLAD. The first type of plates had columns shaped into six-sided spirals, formed by holding ϕ fixed for 180 nm segments of film growth, and rotating the substrate by 60° in-between segments. Five micrometer thick plates were made with α fixed at either 45°, 76°, 80°, 84° or 86°. Table 3.1(a) summarizes the different isotropic plates fabricated for this study. Figure 3.2 shows top and side view scanning electron microscope (SEM) images of these plates. Additionally, 1 μm, 3 μm, 5 μm, and 7 μm thick hexagonal spiral plates were made with α fixed at 84°. SEM images of these films can be seen in Figure 3.3. In all cases, the tendency of columns grown at large deposition angles to broaden as they grow in height was limited by using the PhiSweep technique during deposition [26].

The second type of plates had anisotropic columns shaped by growing 500 nm segments of film at a fixed deposition angle of 84°, periodically alternating between ϕ fixed at 0° or 180°. Films grown this way were characterized by columns that have been extended into long 'rows' of silica with zig-zag shaped walls, seen in

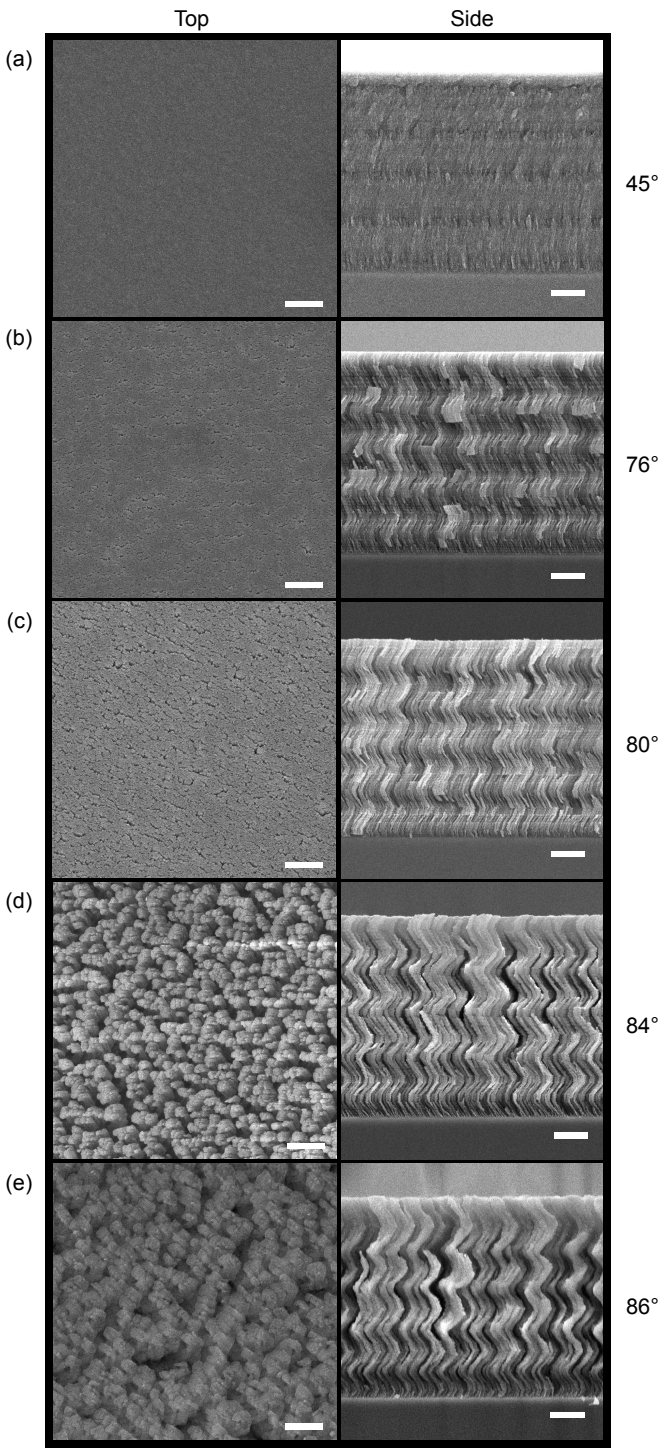

Figure 3.2: Top and side view micrographs of 5 μm thick nanostructured TLC plates deposited at deposition angles of (a) 45°, (b) 76°, (c) 80°, (d) 84°, and (e) 86°. Scale bars are 1 μm.

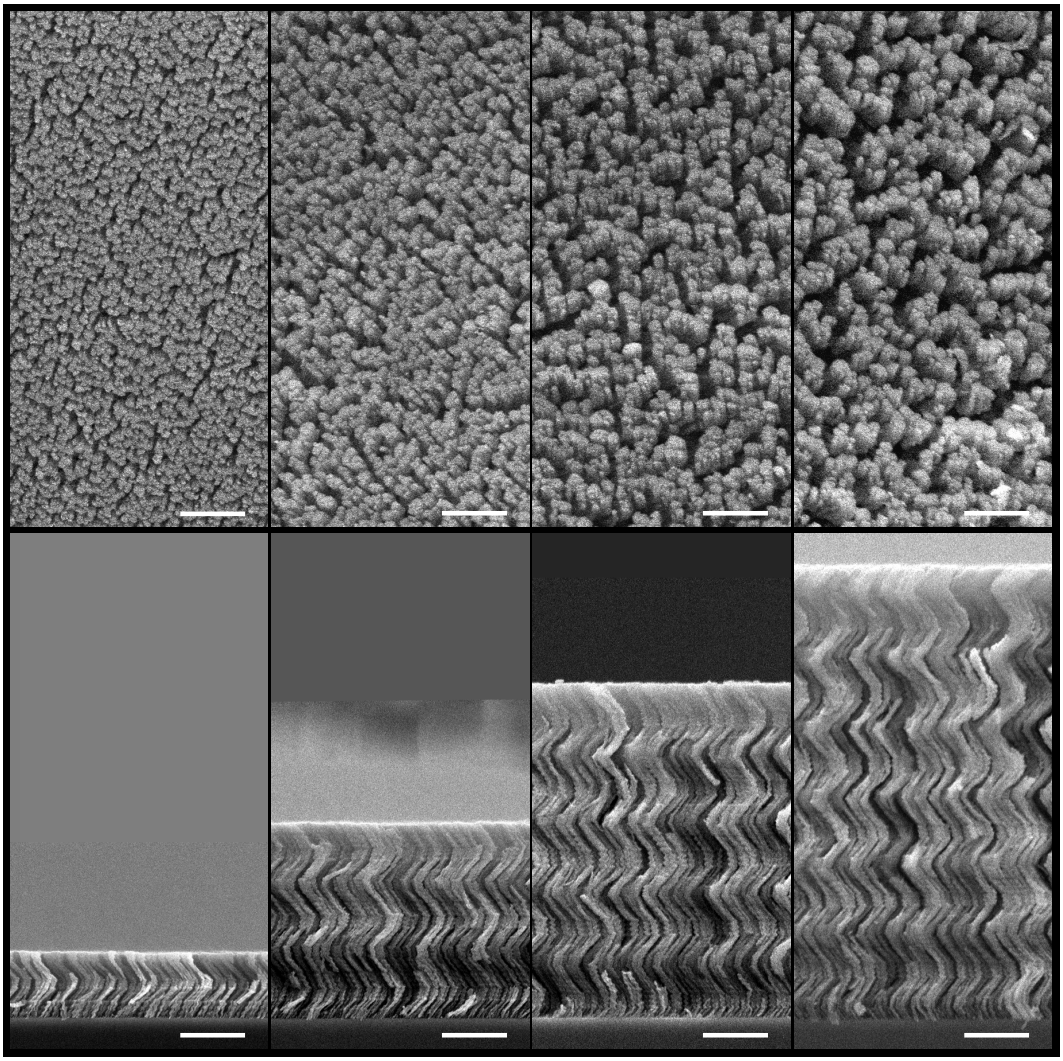

Figure 3.3: Top and side view micrographs of (a) 1 μm, (b) 3 μm, (c) 5 μm, and (d) 7 μm thick nanostructured TLC plates deposited at a deposition angle of 84°. Scale bars are 1 μm.

Figure 3.4(a)-(d). Another set of anisotropic films were made by slightly altering the deposition technique and superimposing a 60° ϕ sweep component over the previously described zig-zag structure. A detailed description is as follows: ϕ is held at −30° for 25 nm of growth, then it is swept from −30° to 30° over the next 50 nm of growth, is held at 30° for 25 nm of growth, and finally it is swept back to −30° over another 50 nm of growth. This superimposed pattern is continued for the full 525 nm segment height. The next segment is similarly grown by sweeping between ϕ = 150° and 210°. The deposition parameters for the two films are shown in Table 3.1(b). Figure 3.4(e)-(g) shows that films grown this way had zig-zag shaped columns very similar to those above, but with less pronounced 'channels' when viewed from the top. The stationary-ϕ films will be referred to as the 'anisotropic' nanostructured (A-NS) plates, while the swept-ϕ films will be referred to as the 'superimposed' NS (S-NS) plates.

3.2.2 Thin Layer Chromatography

Undiluted Analtech Test Dye I (Analtech Inc.) containing 1.0 mg mL^{-1} each of Fast Green FCF, Rhodamine B, Bismark Brown Y and Sudan IV was separated on NS-UTLC plates using the following procedure:

The plates were made using the process described above. Dye mixture was spotted 5 mm from the bottom of the plates using a 30 ga stainless steel blunt-end needle

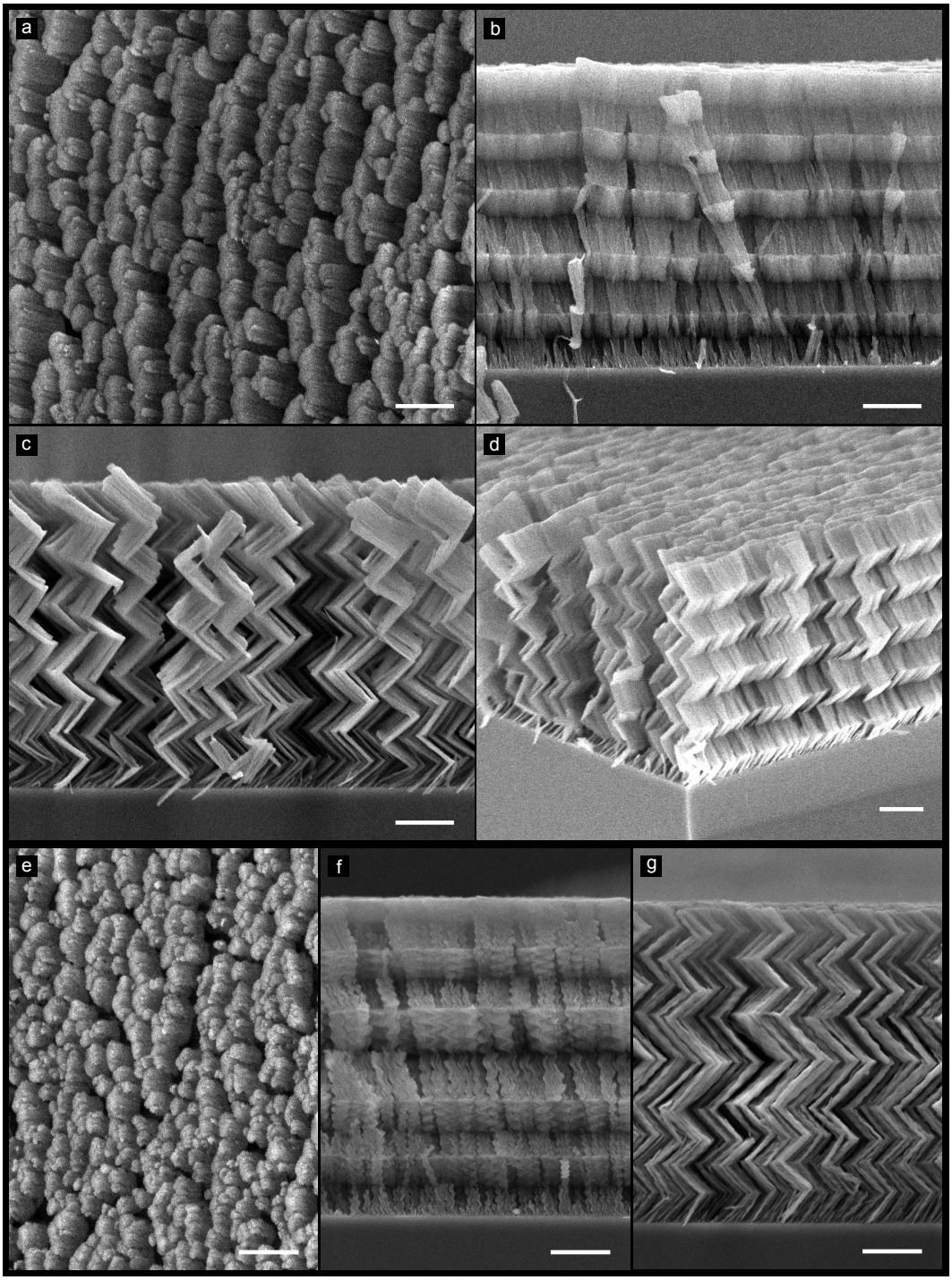

Figure 3.4: Micrographs of anisotropic nanostructured plates. (a) Top view, (b) and (c) orthogonal side views, and (d) oblique view of fixed-ϕ (A-NS) plates. The incident flux is from the left and right in (a). (e-g) Top and side views of the plates with a superimposed-ϕ component (S-NS). Scale bars are 1 μm.

Table 3.1: Summary of the different (a) isotropic and (b) anisotropic plates deposited and used for thin layer chromatography in this chapter.

(a) **Isotropic plates**

Different Deposition Angles					
Deposition angle α	45°	76°	80°	84°	86°
Nominal film thickness	5 μm	5 μm	5 μm	5 μm	5 μm
Different Thicknesses					
Deposition angle α	84°	84°	84°	84°	
Nominal film thickness	1 μm	3 μm	5 μm	7 μm	

(b) **Anistropic plates**

Structure	α	*Nominal th.*	*Pitch*	*Sweep angle*	*Sweep height*	*Pause height*
A-NS	84°	5 μm	500 nm	–	–	–
S-NS	84°	5 μm	525 nm	60°	50 nm	25 nm

(I&J Fisnar Inc.) and a 3-axis robotic arm (IJ2200 Dispensing Robot, I&J Fisnar Inc.) (Fig. 3.5(a)). Each spot had a volume of less than 10 nL. Since this is a qualitative comparison, more precise calibration of volumes was unnecessary. The mobile phase was ethanol-toluene-H_2O (35:60:3.5, v/v/v). The plates were developed in sealed 50 mL beakers containing 2 mL of the mobile phase solution, with 30 minutes allowed for vapor-phase equilibriation prior to separation (Fig. 3.5(b)). Beakers were used instead of development chambers due to the small size of the plates, and a glass insert in the bottom of the beaker ensured a consistent lean angle during development. Development times typically ranged between 3.5 minutes and 10 minutes, with migration distances between 3 mm and 10 mm. Development times were selected based on the shortest distances that produced acceptable resolution without significant band broadening. The plates were allowed to dry after development, and digitized

using a flat-bed scanner (600dpi x 1200dpi, CanonScan LiDE20, Canon Canada Inc.). Chromatograms were obtained from the digitized images using videodensitometry software (Sorbfil TLC Videodensitometer, OOO IMID). The chromatograms produced plot the plate color density over the separation track, where each point of color density is calculated as a summation of pixel saturation across each line of pixels of a defined track.

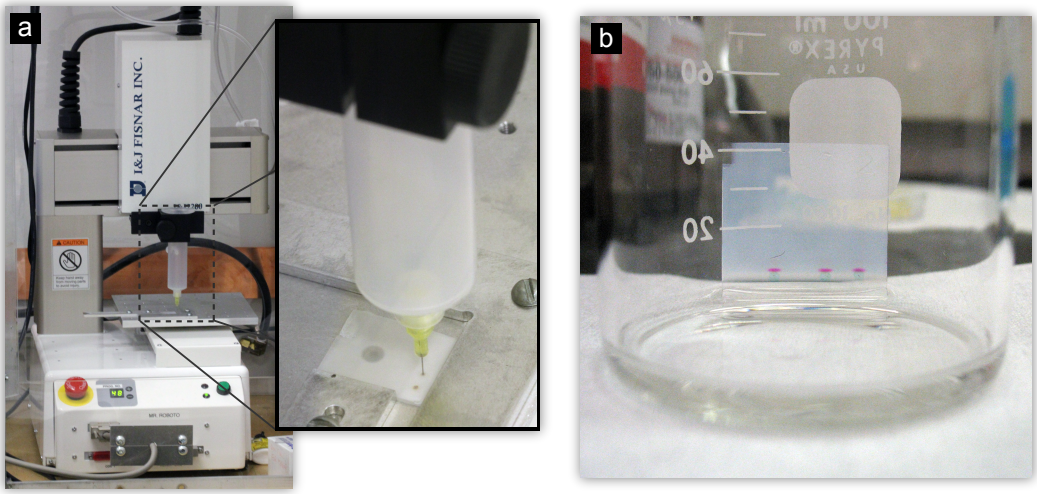

Figure 3.5: (a) I&J Fisnar 3-axis robotic arm with blunt-end needle used to spot UTLC plates with analyte mixture. (b) A GLAD UTLC plate being developed in a glass beaker.

3.3 Results

3.3.1 NS-UTLC Plate Structures

Figure 3.2 reveals how the NS-UTLC sorbent structure changed as the deposition angle was increased from 45° to 86°. A columnar structure is evident in all five films.

As the angle increased past 80°, the columns became well-separated, forming isolated spiral columns, with an accompanying increase in the column diameter and in the size of the inter-column pores, moving from mesopores (2 nm - 50 nm) to macropores (> 50 nm). It has been previously reported that in GLAD films each column is comprised of multiple agglomerated bifurcating fibers that are tens of angstroms in diameter; this structure is largely independent of deposition angle [56]. As a result, individual columns have a consistent microporous (< 2 nm) structure. Consequently, these films all have consistent, column-dependent micro- and mesoporous structures, accompanied by an increasing availability of macropores as the deposition angle is increased past 80°.

The column diameter and structure, and consequently the pore structure, were not constant along the height of the film, which is evident in Figure 3.3. As the films grew, some columns became larger in diameter while others disappeared, increasing the mean column diameter along with the mean macropore size. This characteristic of GLAD thin film growth is well documented and is caused by some columns being extinguished while surrounding columns intercept more incoming flux [21, 26, 56]. The effect is minor at lower α, and becomes significant as α is increased beyond 80°.

The anisotropic films had columns with two entirely different in-plane structures, which could be exploited by choosing the TLC development direction. The plates were grown such that, when viewed on one edge, the film takes on the zig-zag appearance

seen in Figures 3.4(c) and (g), with the spaces in-between columns forming channels running up the film. When turned 90° from the zig-zags and viewed on edge, the film takes on the denser appearance seen in Figures 3.4(b) and (f). This is also evident in the oblique view shown in Figure 3.4(d). The channels were not as well defined with less continous walls in the S-NS films compared to the A-NS films (Figures 3.4(a)&(e)). Since the mobile phase travels in the plane of the film, two different effective structures could be presented for development: in-channel (IC) development, where the mobile phase travels up the channels between zig-zags (i.e. upwards in Figures 3.4(a)&(e)), and cross-channel (CC) development, where the mobile phase has to move through the pores in the channel 'walls' (i.e. sideways in Figures 3.4(a)&(e)).

3.3.2 Separation on 5 μm Films With Different Deposition Angles

The quality of separation on 5 μm thick films was found to be highly dependent on deposition angle. The test dye was resolved into its four colour components using plates grown at angles of 84° and 86°. The plate grown at 80° showed poor separation of the dye components, with all four spots overlapping, while the plate grown at 76° did not show noticeable solute movement as the solvent front moved past the application spot. For the relatively dense and close-packed plate grown at 45°, the mobile phase was unable to wick up the film. We observed that the mobile phase velocity increased with increasing deposition angle. Figure 3.6 shows the dye

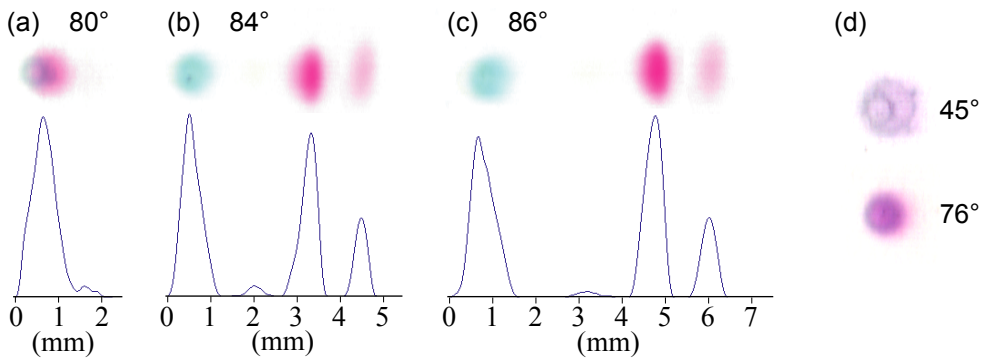

Figure 3.6: Representative examples and accompanying chromatograms of separations performed on plates with different deposition angles. (a)-(c): α = 80°, 84°, 86°. Development times were 6 min, 4.5 min, and 5 min, respectively. (d) No separation was observed on plates with α = 45° or α = 76° within 10 min development times. The Y-axis is colour density, with the peak intensity normalized across the three graphs.

separations successfully performed on these plates, along with their accompanying chromatograms; the unresolved spots on plates grown at 45° and 76° are also shown without chromatograms.

3.3.3 Separation on Films of Increasing Thickness

Dye separations performed on 1 μm, 3 μm, 5 μm, and 7 μm films grown at a deposition angle of 84° can be seen along with their chromatograms in Fig.3.7. The 1 μm film was unable to resolve the dye components. Separation on the 3 μm film was improved; however, significant band broadening was observed, limiting component resolution. All four dye components could be resolved in a short distance (less than 5 mm) on both the 5 μm and 7 μm films, requiring elution times of less than 5 minutes. Thinner films required longer development times, due to lower mobile phase velocities.

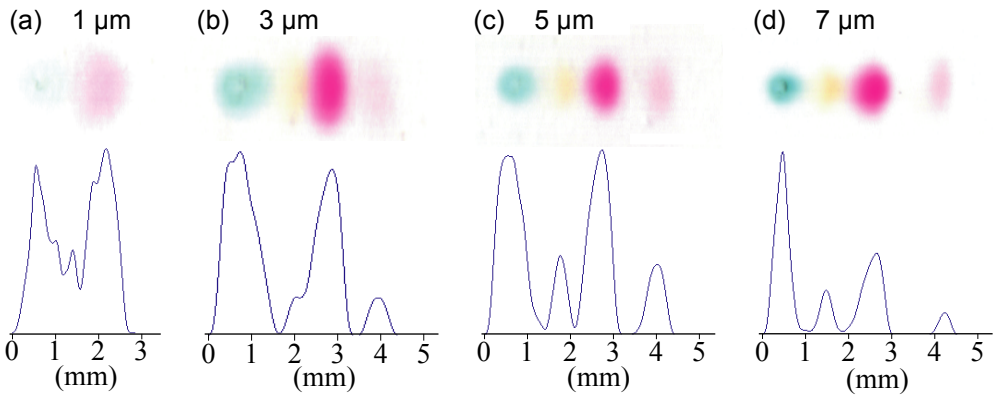

Figure 3.7: Representative examples and accompanying chromatograms of separations performed on plates with increasing stationary phase thickness. (a)-(d): 1 μm, 3 μm, 5 μm, and 7 μm. Development times were 8.5 min, 4.5 min, 5 min, and 5 min, respectively. The Y-axis is colour density, with the peak intensity normalized across the three graphs.

3.3.4 Separation on Anisotropic Nanostructured Plates

Anisotropic plate structures had a distinct effect on the dye separation. The dye was well separated by in-channel development for both A-NS and S-NS plates, but not by cross-channel development (Figure 3.8). The distinct channels in the A-NS plates led to marked diffusion along the development direction during in-channel development, leading to long oval-shaped spots. Suppressing the distinct channels while maintaining the anisotropic structure resulted in better IC separations on the S-NS plates, with less spot broadening in the mobile phase flow direction. In both cases, mobile phase velocity was slow during CC development as a result of the dense film structure in that direction, and the subsequent separations were poor.

Figure 3.8(f) shows a unique, interesting effect achieved with anisotropic plates. In this case, the plate was developed such that the mobile phase flow direction was

diagonal to the anisotropy – that is, at a 45° angle to both the IC and CC directions. While the mobile phase moved upwards as expected, the spots separated along the IC direction. On this film, the mobile phase movement and the solute spot movement – which on regular TLC and UTLC plates are identical (upwards) – was decoupled by the nanostructured sorbent layer. Figure 3.9 illustrates the solvent front and spot movement relative to the film structure.

3.4 Discussion

The results show that silica thin films deposited by GLAD are effective as planar chromatography stationary phases. The improved separation quality with increasing deposition angle can be explained by the changes in film morphology and the resulting porosity changes. As the deposition angle increased, the average column diameter and inter-column spacing increased, in turn increasing the size of macropores in the films. At the same time, the specific surface area decreases as the deposition angle increases beyond ~70° [57, 58]. The net effect is that larger deposition angles produce coarser particle layers, with larger macroporosity but similar mesoporosity. This allows for increased solvent front velocities at higher deposition angles, with a smaller change in spot diffusion rates between films. As a result, the development length increased and resolution improved.

Increased solvent front velocities, combined with an increase in available surface

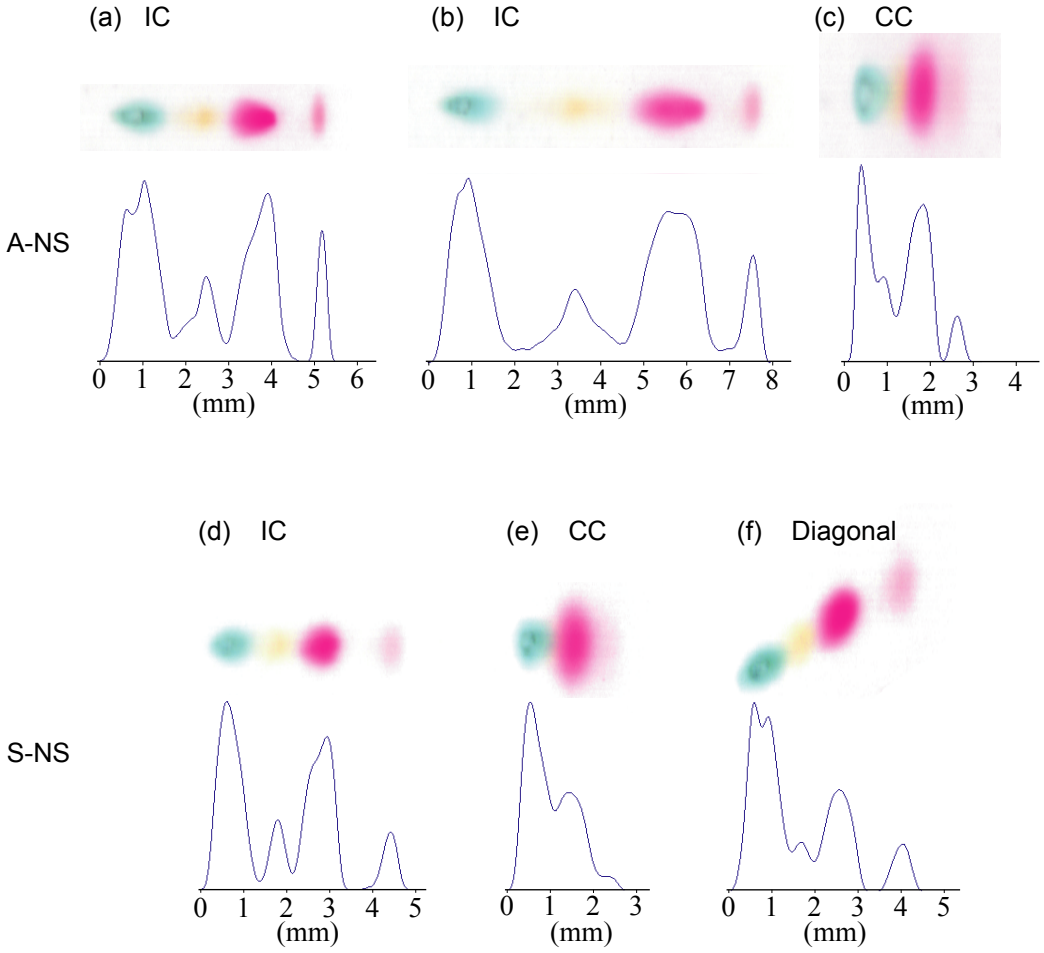

Figure 3.8: Representative examples and accompanying chromatograms of separations performed on anisotropic nanostructured plates. Top row: The A-NS plate developed in the in-channel (a)-(b) and cross-channel (c) directions (2.5 min, 4.5 min and 10 min development times, respectively). Bottom row: The S-NS plate developed in the in-channel (d), cross-channel (e) and diagonal (f) directions (4.5 min, 4 min and 10 min development times). In the orientations shown, elution was horizontal for all plates, including (f). The Y-axis is colour density, with the peak intensity normalized across the three graphs.

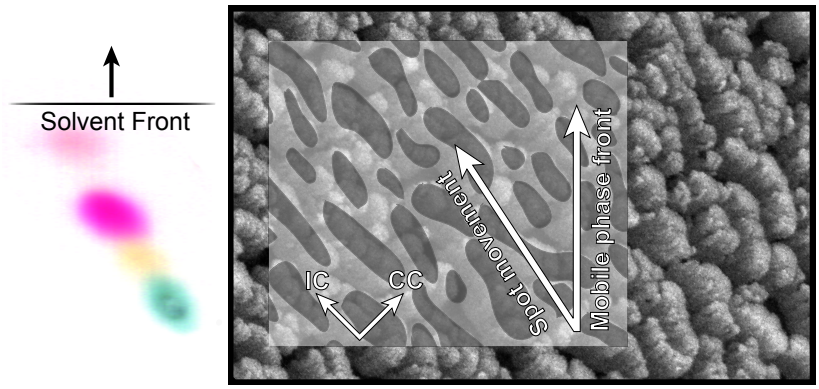

Figure 3.9: The spot and solvent front directions are decoupled when the solvent is eluted diagonally to the IC and CC directions (left). The spots do not move parallel to the solvent front, instead following the IC direction (right).

area, are thought to be responsible for the improved separations as the film thickness was increased. The higher macroporosity of the thicker film does not directly affect the solute spot diffusion, but does increase the front velocity. This increased velocity results in faster separation of spots along with lower overall development times that reduces diffusion-related spot broadening. Consequently spots were better separated with higher resolution in the thicker films. The increase in total surface area with thicker films is also thought to be a factor in the improved separations. Decreased spot sizes were observed as the film was made thicker, due to a larger vertical area (and hence smaller lateral area) occupied by the constant-volume spot. The larger spot sizes on the thinner plates effectively reduces separation resolution, as the overlap of spots is greater for the same distance of physical separation along the plate. This improved resolution on thicker plates, combined with higher solvent front velocities that lead to larger physical separation of spots and lower diffusional broadening, leads

to better separation efficiency.

There was a significant retention difference observed between silica gel TLC plates and NS-UTLC plates. Attempts to separate the dye on NS-UTLC plates with the EtOAc:MeOH:H_2O (80:20:20 v/v/v) mobile phase recommended for separation on HPTLC plates were largely unsuccessful. The compounds were weakly retained, migrating to the solvent front as lines rather than spots, and only the pink and blue dye spots could be distinguished, with poor resolution and in reversed order. To achieve better separations, we used the PRISMA optimization system to determine a more suitable mobile phase [59]. This involves a systematic adjustment of the solvent strength (a measure of polarity) and type (based on Snyder's classification system) using the elution order and retention factors as the criteria for adjustment [60].

The solvent strength had to be reduced by moving to an ethanol: toluene: H_2O mobile phase (35:60:3.5, v/v/v), which has a total solvent strength of 3.35, compared to 5.48 for the EtOAc:MeOH:H_2O mobile phase. This represents a significant reduction considering that the stationary phase material was silica in both cases. While the cause is not known, differences in the available surface area of NS-UTLC plates relative to standard TLC plates may play a role. Recent measurements have shown that the specific surface area of SiO_2 GLAD films grown at 85° is approximately 500 $m^2\,g^{-1}$, which is similar to that of HPTLC plates [58]. However, the effective surface area available to analytes in GLAD posts may still differ due to fewer available

SiO_2 moieties on the surface as a result of the fabrication process, and due to the tortuous internal pore structure [61] of the GLAD posts that may not be accessible to solvated analyte molecules. The lower effective surface area provides fewer sites for interaction between the solute and stationary phase, leading to weak solute retention and subsequent fronting.

Alternatively, the retention difference between NS-UTLC plates and UTLC/HP-TLC/TLC plates could be due to the difference in film morphology between our plates and standard plates. The macropores are different in NS-UTLC plates compared to other stationary phases, in that there is not a network of macropores connected by smaller pores, but rather convoluted 'channels' of macropores that extend along the surface of the plate. The mobile phase velocity is higher as a result, decreasing the interaction time between solute and stationary phase at a given time interval of development. The separations on anisotropic films support this reasoning. The specific surface area on the film is the same regardless of the development direction, but the mobile phase velocity and solute retention depended heavily on the direction, suggesting that the macroporous 'channels' play a significant role in solute retention.

These initial results are promising, and it is expected that separations on NS-UTLC plates can be further optimized. The lower resolution of NS-UTLC compared to HPTLC separations was not unexpected, as this was previously observed in UTLC plates due to the reduced separation distance [54]. The resolution was also limited by

the large applied spot sizes, a restriction of our current equipment. Volumes much smaller than the ~5 nL applied in this work should be sufficient for analysis, while significantly reducing spot size and the demand for analyte. There was no attempt to further optimize development conditions, which would also be expected to improve separation efficiency.

Further investigation into the effect of different nanocolumn compositions and morphologies may reveal additional improvements in separation efficiency and resolution. It may be possible to exploit the effects of plate anisotropy to improve separation quality or even introduce new separation capabilities compared to current TLC plates. As an example, the different porosities – and hence effective particle sizes – encountered along different development directions could potentially be used to enhance 2-D TLC [62]. Sorbent material selection is also greatly enlarged due to the large variety of materials that can be deposited by GLAD. The openness of the structure from the substrate to the surface of the stationary phase and the ability to form thinner layers than monolithic silica UTLC plates may also prove beneficial in coupled TLC-MS techniques, such as UTLC-AP-MALDI-MS [55].

Other notable results have been reported since completion of the work presented in this chapter. Morlock *et al.*, in collaboration with our lab, compared the performance of GLAD and commercial UTLC plates in development of an 'Office Chromatography' concept [63]. Office Chromatography integrates and automates all the

steps of thin layer chromatograpy – analyte spotting, plate development, plate image capture, conversion to chromatogram and chromatogram analysis – on a printer-sized benchtop system, and is centered on the faster, more compact separations possible with UTLC. Analyte deposition is performed with an inkjet, permitting deposition of more precise and lower volume spots with no damage to the UTLC plate, improving separation resolution.

Development and engineering of UTLC plate technology has been continued in our lab by Steven Jim and Michael Taschuk. Jim *et al.* characterized the anisotropic behaviour and performance of chevron structures along with two new plate structures: isotropic vertical posts and anisotropic 'blades' grown using the serial bideposition technique [64]. Deviation of the separation track from the mobile phase movement observed here for anisotropic chevron plates (Fig 3.9) was also observed on the anisotropic plates grown with serial bideposition. Table 3.2 shows the limits of detection, plate numbers and plate heights obtained with vertical post, chevron, and serial bideposited GLAD UTLC plates. The limits of detection measured by Jim *et al.* are an order of magnitude larger than those achieved using other UTLC media, while the plate numbers and plate heights were found to be lower than recently reported electrospun polymer UTLC plates [65] but comparable to or better than normal phase TLC, HPTLC, and monolithic silica gel UTLC plates.

Table 3.2: Limits of detection (LOD), plate number and plate height calculated by separation of dimethyl yellow (undiluted and 50% diluted) on vertical post, chevron, and serial-bideposited (SBD) GLAD plates. Reprinted in modified form with permission from S. Jim *et al.* [64]. © 2010 American Chemical Society.

Plate structure	LOD (ng)	Plate number N		Plate height H (μm)	
(dev. direction)		undiluted	diluted	undiluted	diluted
vertical posts	10 ± 4	540 ± 50	270 ± 25	12 ± 1	21 ± 2
chevron (along-ch.)		170	150 ± 5	22	23.5 ± 0.5
chevron (diag. ch.)			167 ± 6		18 ± 1
SBD (along-ch.)	11 ± 3	480 ± 140	260 ± 25	21 ± 6	28 ± 2
SBD (diag. ch.)		340 ± 20	330 ± 50	16 ± 1	17 ± 2

3.5 Concluding Remarks

Nanostructured thin films have been used as an effective thin layer chromatography stationary phase. It has also been shown that the separation characteristics can be easily altered by changing the nanostructure architecture and morphology. The in-plane column symmetry was found to have a notable effect on the separation, as the solvent front movement and spot development directions are decoupled on sorbent layers with in-plane anisotropic nanostructures. It is expected that further study and optimization of these GLAD fabricated NS-TLC plates will extend their applicability in simple TLC, and possibly in more complex applications including 2-D TLC, coupled techniques, and microfluidics. In particular, the pronounced effect anisotropic structures had on separations suggests that careful engineering and modification of the plate nanostructure could introduce new techniques for controlling or optimizing separations. Continuing work by Jim and Morlock has

shown that unoptimized plates provide performance similar to existing technology, without consideration for the ability to further structure and modify GLAD UTLC plates. These results are very encouraging and motivate ongoing engineering and optimization of GLAD UTLC plates.

MICROFLUIDIC CHANNELS WITH EMBEDDED GLAD-FABRICATED NANOSTRUCTURES[1]

4

4.1 Introduction

Microfluidic system capabilities and applications have grown rapidly over the past two decades [4, 5, 67, 68]. Porous structure integration into microchannels has enhanced existing and introduced new microfluidic applications, particularly in electrophoretic and chromatographic biomolecular separations [6, 10, 11, 69]. Several different techniques have been developed for creating such porous channels, including micro- and nanofabricated pillars, solid particle packings, and porous monolith polymerization [6, 10, 69]. Direct fabrication of porous structures permits control of pillar/pore distributions, sizes, arrangements, homogeneity and architectures. This has led to faster and higher resolution separations [70] and has also provided access to unique separation mechanisms [71–73].

Volkmuth *et al.* first used microfabricated pillars in silicon dioxide to create an artificial agarose gel with controllable and known porosity for studying the electrophoretic migration of DNA through porous matrices [74]; Duke *et al.* extended this technique to fractionate DNA streams by pulsed-field electrophoresis [75]. Constant

[1] A version of this chapter has been submitted for publication [66].

or pulsed field electrophoretic DNA separations were performed in channels containing artificial sieves instead of porous gels, using microfabricated silicon, silicon dioxide or PDMS pillars [76–81]. Magnetically aligned vertical columns of superparamagnetic beads [82] and an ordered three-dimensional porous network (formed by a self-assembled colloidal array) have been used for the same purpose [83]. Nanopillars fabricated in silicon and quartz using electron-beam lithography and plasma etching techniques have also been used to electrophoretically separate DNA [84, 85].

Design and fabrication of separating media permits unique separation methods not achievable with traditional media. Creating pores smaller than a polymer's radius of gyration forces deformation at an entropic cost; this has been used to separate DNA by entropic recoil [86, 87] and entropic trapping [88] in nanopillar arrays. Careful design of a 2-dimensional entropic trap array along with appropriate buffer selection and separating conditions allowed independent control over separation speed and resolution, via either entropic trapping or Ogston sieving, on a single device [71, 89]. The diffusional and thermodynamic characteristics of DNA and other molecules are exploited in separations on carefully designed "laterally asymmetric diffusion arrays", also known as Brownian ratchets [75, 90, 91]. Similarly, arrays can be designed and fabricated to create bifurcated laminar streams around pillars; micron-sized particles are then separated without diffusive band broadening by deterministic lateral displacement that arises due to differences in particle sizes [73, 92].

Nanofabricated pillars and porous alumina (fabricated by anodization) have been used to separate DNA via electrophoresis-driven size exclusion chromatography [93, 94]. Baba *et al.* used two different configurations of sub-micron pillars to demonstrate separation of the same DNA mixture by either size exclusion chromatography or electrophoresis [84]. Artificial packed bed structures have been fabricated in quartz, silicon and PDMS to optimize and study the ideal performance of capillary electrochromatography [70, 95–97] and pressure-driven liquid chromatography [98, 99]; these devices were used to separate peptides, fluorescent dyes, and pyoverdines from a complex mixture.

Micro and nanofabricated porous structures have also been applied to ZnO/TiO_2 nanorod microreactors [100], PMMA pillar-based catalysis beds [101], oxidized Si pillars for capturing, purifying, and concentrating DNA [102], and a polymeric micropillar array device with a microreactor terminating in a clog-free nozzle for electrospray ionization mass spectrometry [103].

Our group previously reported the integration of microstructures fabricated using GLAD into microchannels [104, 105]. The integration of GLAD films in microfluidic systems is attractive for a number of reasons: precisely controlled morphology, compatibility with multiple materials, and demonstrated application to many systems. Films can have very high surface areas [58] and both the porosity and architecture can be finely controlled in three dimensions, e.g. porosity and structure can be varied in

the plane of the device as well as through the thickness of the film (and consequently through the depth of the channel) [106]. Many materials can be used, including insulators (e.g. SiO_2, Al_2O_3, TiO_2), semiconductors (e.g. Si, Ge) and metals (e.g. Ti, Zn, Cu); furthermore, heterostructures that combine different materials can also be grown [13, 107]. GLAD films have been applied to applications that could benefit from integration with microfluidic systems, such as sensing [43, 46, 47], thin layer chromatography [64], and matrix-free laser desorption ionization [108].

However, GLAD film growth requires an obliquely-held substrate. This complicates the process of depositing porous GLAD films into pre-fabricated microchannels [105]. Kiema *et al.* circumvented this issue by fabricating regular arrays of posts in a channel surrounded by dense nanofibrous walls [104]. While effective in creating a good seal between post-tops and channel ceiling, the required bi-modal porosity engineering algorithm limits the variety of possible structures that can be made [26]. This method requires time-consuming electron-beam lithography to pattern seed arrays on the substrate accompanied by precise seed spacing conditions, allows only certain architectures as a result of the PhiSweep algorithm, limits the materials that can be used, and produces porous, albeit dense, nanofibrous channel walls.

Sacrificial etching techniques have been used to integrate micron and sub-micron sized fabricated pillar arrays into microchannels. Turner *et al.* created an artificial gel for DNA separation, using standard microlithography techniques to fabricate

sub-micron SiN pillars by wet etching of a sacrificial polysilicon layer [109]. Chen *et al.* created large area PMMA nanopillar arrays by cast molding into a nanoporous aluminum oxide template that could be removed through subsequent etching [101]. Kim *et al.* used a similar nanoporous aluminum oxide templating strategy to fabricate PDMS nanopillar arrays [110]. Yun *et al.* used sacrificial removal of photoresist to fabricate three-dimensional structures and multilevel microchannels in PDMS [111]. Sacrificial techniques are suited to creating channels containing GLAD-deposited structures as the issues accompanying varying film heights and structures and the rough film surface topology can be circumvented.

In this chapter, a flexible sacrificial etching technique is described that can be used to integrate GLAD-grown films into PDMS microfluidic channels with little limitation on film material and no limitation on film structure. The versatility of this technique is demonstrated by filling channels with structures of different materials and architectures. Demonstrating the applicability of our process, we have performed DNA separation by fractionation in a pulsed electric field, using devices filled with SiO_2 GLAD porous films.

The work presented in this chapter was performed in collaboration with Dr. D. Jed Harrison's lab in the Department of Chemistry at the University of Alberta. Neda Nazemifard assisted with all aspects of the DNA separation experiments other than device fabrication. Abebaw Jemere consulted on experimental setup and procedure.

My contribution was the origination and development of the fabrication process, device fabrication, film characterization, and experimental interpretation.

4.2 Materials and Methods

4.2.1 Chemicals and Materials

Films were deposited onto Corning 0211 glass substrates (10 cm x 10 cm, 0.5 mm thick, Corning Inc. Technical Materials, Corning, NY, USA) cut to appropriate sizes (typically 2.5 cm x 2.5 cm) with a dicing saw, onto microscope cover glass (0.17 mm thick, Fisher Scientific Company, Ottawa, ON, CAN), or onto silicon wafers (Test Grade, 10 cm diameter, University Wafer, Boston, MA, USA). Evaporated materials, SiO_2 (> 99.99% pure), Si (> 99.999% pure), TiO_2 (> 99.9% pure), Al_2O_3 (> 99.99% pure) and Ag (> 99.99% pure) were purchased from CERAC, Inc. (Milwaukee, WI, USA). Polydimethyl siloxane (PDMS) base and curing agent (Sylgard 184 silicone elastomer base and curing agent, Dow Corning Corporation, Midland, MI, USA) and the following chemicals were used during the fabrication process: HPR 506 and HPR 504 positive photoresist (Fujifilm Electronic Materials USA Inc., North Kingstown, RI, USA); AZ P4620 positive photoresist (AZ Electronic Materials USA Corp., Somerville, NJ, USA); Microposit 351 Developer (Shipley Company, L.L.C., Marlborough, MA, USA) diluted 1:4 on-site with deionized water; Microposit Remover 1165 (Shipley Company); methanol (> 99.8% pure).

DNA samples, NoLimits™DNA fragments (6 kbp, 10 kbp, 20 kbp, Fermentas Canada Inc., Burlington, ON, CAN) and λ-DNA (48 kbp, New England Biolabs Ltd., Pickering, ON, CAN) were stained by Molecular Probes YOYO-1 (Invitrogen Canada Inc., Burlington, ON, CAN) with a dye-to-base ratio of 1:10. Pulsed field electrophoresis was performed in 4× TBE buffer (356 mM tris-borate, 8 mM ethylenediamine tetra-acetic acid, pH 8.3) to suppress electroosmotic flow, with 4% v/v 2-mercaptoethanol added to reduce photobleaching. Pulsed electric fields were generated by homebuilt high-voltage amplifiers triggered by square wave signals from a synthesized function generator (Wavetek, San Diego, CA, USA). The separation chamber was connected to reservoirs where pulsed electric potentials were applied using platinum electrodes. The applied pulsed electric potentials generated asymmetric obtuse-angle pulsed fields, E_1 and E_2, across the separation chamber, where the angle between the pulsed fields is ~ 135° and $E_2 = 1.4\,E_1$ in all our experiments.

DNA samples were excited by a 488-nm argon ion laser beam, and the fluorescent emission was collected by a CCD camera through a 505DRLP dichroic mirror and a 515 nm long-pass filter. For separation imaging, a 4× objective (0.1 N.A., Olympus Canada Inc., Markham, ON, CAN) was used. For single DNA imaging, a motorized total internal reflection fluorescence (TIRF) microscopy system was used with a 60× oil-immersion objective (Nikon Canada Inc., Mississauga, ON, CAN). TIRF microscopy is specially designed to enable single molecule visualization with a high

signal to noise ratio.

Scanning electron micrographs were taken of devices during and after fabrication with an Hitachi S-4800 field emission scanning electron microscope.

4.2.2 Fabrication Process

A sacrificial etch process was used to fabricate microfluidic devices with GLAD structure-filled channels (Figure 4.1). First, the desired micro/nanostructures are deposited onto a clean, flat substrate. The porous film is filled with photoresist by spin application, and the resist is photolithographically patterned to define the microfluidic channels. The entire substrate is coated with PDMS, which is then cured. Fluid reservoirs that also serve as access holes for the sacrificial etch are punched or cut out of the PDMS. A sacrificial etch is used to remove the photoresist from the microfluidic channels, and the device is dried to complete the fabrication process. Each process step is described in detail as follows:

GLAD deposition: All substrates were cleaned prior to deposition using a Piranha etch (3:1 sulfuric acid and hydrogen peroxide) and air dried. GLAD films were deposited to the desired thickness by electron-beam evaporation of the target material (SiO_2, Si, TiO_2, Al_2O_3, or Ag) with an established base pressure of $8x10^{-5}$ Pa or lower. Corning 0211 glass was used to make functional transparent devices amenable to laser induced fluorescence, thin microscope slide cover glasses were used to make devices

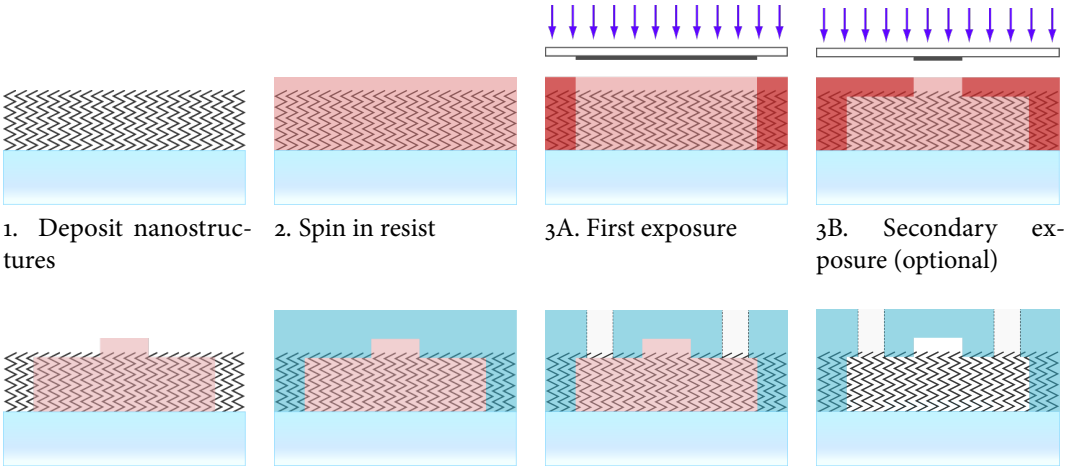

Figure 4.1: Process used to fabricate microchannels with embedded GLAD-deposited micro- and nanostructures. (Figure is illustrative and relative scaling between GLAD structure and channel feature sizes is not representative of true dimensions).

for TIRF microscopy, and silicon was used to produce samples that could be easily cleaved for scanning electron microscopy imaging. SEM imaging has verified that film growth and structure are the same on smooth glass substrates as on the thin native oxide on the silicon substrates. Deposition rates as measured for a normal-oriented substrate by a quartz crystal microbalance varied between 1.2 nm s^{-1} and 2.0 nm s^{-1}; effective deposition rates are lower at oblique deposition angles. The films presented here ranged in thickness from 4 μm to 7 μm.

Photoresist application: HPR 506 was spun into the films at two different velocities for a spread-spin application. For each film, a 500 rpm, 10 s spread phase was followed by a 40 s spin phase with a rotation rate dependent on the film structure, film thickness, film porosity and the desired resist thickness. Typically, a rate between 1500 rpm

and 2000 rpm was used for films 5 μm to 6 μm tall. The substrate and photoresist were baked for 90 s at 115°C to remove residual solvent and were left to equilibrate to room humidity for more than 30 minutes. The resist completely infiltrates the GLAD film [105, 112], and an overburden of photoresist typically remains on top of the structures after spinning in the resist, shown schematically in Figure 4.1(2).

Photoresist patterning: The desired microchannel pattern was transfered to the photoresist using standard photolithography techniques (chromium mask, 405/365 nm filtered mercury arc lamp). When needed, a second exposure was performed either without a mask, or through a second mask aligned to features defined by the first mask – these features were visible in the slight change in resist color following the first exposure. This second exposure was used to fine tune the height of the channels by altering the resist thickness through a combination of spin-in velocity and secondary exposure time. In this fashion structures could either be sealed to the ceiling of the device, or a space could be left between the tops of the structures and the device ceiling (both illustrated in Fig. 4.1(3)). Exposed resist was etched away by agitation in developing solution for 35 s, followed by a deionized water rinse and drying with nitrogen.

PDMS application: PDMS was prepared by mixing the base and curing agent in a 10:1 ratio and degassing under house vacuum (~ 7 bar). The PDMS was then

slowly poured onto the devices to the desired thickness, typically 1–3 mm thick. It was contained by clamping an aluminum ring and rubber gasket to a silicon wafer resting on an aluminum plate, with the devices taped down on the wafer. The PDMS penetrates into the exposed inter-pillar spaces and surrounds the photoresist-filled channels. Curing was accelerated by baking the assembly in an oven at 50°C for four hours.

Sacrificial material removal: PDMS plugs were removed from the devices to create fluid reservoirs; plugs were either gently punched out using a metal punch pushed into the PDMS until it reached the top of the substrate, or were cut into the PDMS using a scalpel. These reservoirs also served as access ports for dissolution and removal of the sacrificial photoresist. The devices were soaked for 24 h in 1-methyl-2-pyrrolidone (Microposit Remover 1165) followed by a second 16 h soak in a fresh batch of 1165. A final 16 h soak in methanol was used to rinse any remaining resist and remover from the channels. The methanol was allowed to evaporate from the channels, and the devices were stored until use.

4.2.3 Alternative Fabrication Strategies

The fabrication process described above was developed after careful consideration of the number of different approaches that could be used to embed GLAD nanostructures in microchannels. As already mentioned, the simplest strategy of direct

deposition into microchannels is not an ideal solution. The self-shadowing required for GLAD growth necessitates building the microfluidic channel around the GLAD film, either during or after deposition. Alternative strategies considered included microembossing, a "liquid lid", and deposition of a capping layer.

Microembossing: Microembossing is normally used to transfer nano- and microstructures patterned on a metal mold to a polymer material by embossing the heated polymer with the mold. This same technique could provide a simple method for encapsulating GLAD films in microchannels, outlined in Figure 4.2. The channels are first patterned in the GLAD film. This can be achieved using several different strategies, including lithography or physical etch masks combined with dry or wet etching techniques, or sacrificial lift-off layers. The films are then directly embossed in the polymer to encapsulate and seal off the channels. Access/reservoir holes can be created before or after embossing. In contrast with standard embossing, the "mold" or GLAD film in this case is left embedded in the polymer layer rather than removing it for more embossing cycles.

The advantage of this technique is that a sacrificial material is not required. Elimination of the sacrificial material would greatly simplify and speed up the fabrication process. With appropriate design, infiltration of polymer into the GLAD film would be negligible. For example, if the polymer viscosity is maintained high enough, or if the chemistry is right, the polymer will remain excluded from the nanoporous GLAD

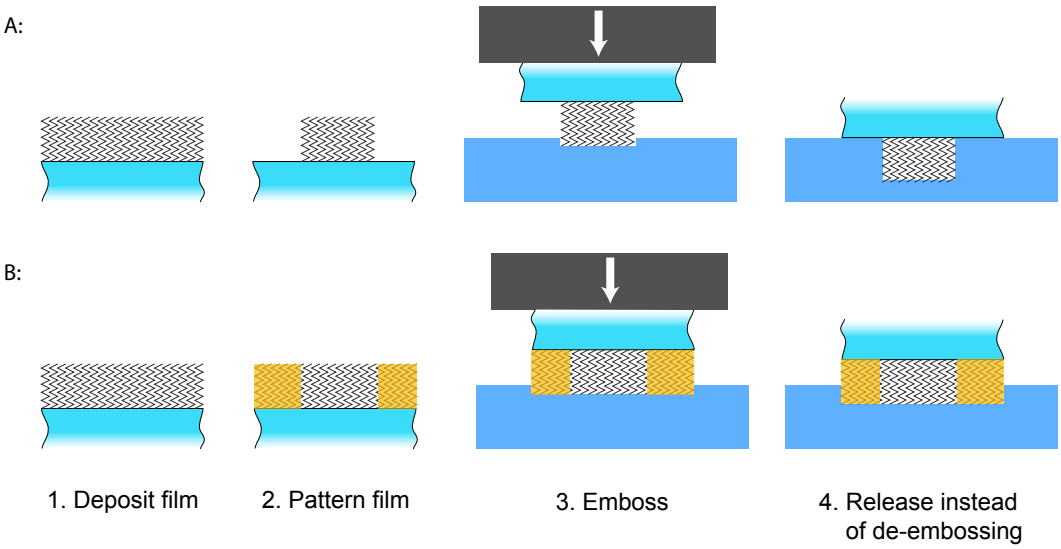

Figure 4.2: Microchannel fabrication by microembossing. GLAD films with patterned channels are forced into a heated polymer to fully encapsulate the channels. Patterning can include removal of unwanted film (A) or infill of unwanted film (B).

film. Alternatively, a capping layer (discussed further below) could limit infiltration to the sides of the channels, which in turn could be limited by short embossing times. Dense supporting walls could be fabricated (e.g. with chemically resistant SU-8 photoresist) before embossing to help relieve the pressure exerted on the film during the embossing procedure. Initial experiments were promising in that the polymer only partially penetrated the GLAD film during embossing. However, film damage was extensive, and thermal expansion mismatch between the GLAD film and the polymer resulted in delamination of the polymer. With significant further development, this technique may be suitable for device fabrication.

Liquid lid: Fabrication of microfluidic channel walls in GLAD films prior to en-

capsulation via a lid is a relatively simpler technique. For example, polymers can be applied to the GLAD film and patterned lithographically to define GLAD-filled channels that are accessible from the top (Fig 4.3(a)). Such channels can then be sealed by placement of a lid over the substrate. The challenge with such a design is creating a good seal between the lid and device. This is complicated by the difficulty in fabricating channel walls that are perfectly level with the intra-channel GLAD structures, and with particulate debris deposited on the surface during the fabrication process. One potential method for circumventing this problem is using a soft or 'liquid' lid that can accommodate small changes in surface topography without complete infiltration of the GLAD-filled channel, as illustrated in Figure 4.3. A photo- or thermo-curable polymer or a self-curing resin (e.g. two-part epoxy) could be an appropriate choice for this approach. This method was considered but has not been attempted.

Capping layer: It is possible to directly cap GLAD films during deposition by rotating the substrate to a near-normal deposition angle, thus depositing a dense film on top of the porous GLAD film [113]. An already-capped GLAD film enables a number of microchannel fabrication strategies. For example, channels can be directly patterned in the film using dry or wet etching techniques. Walls can then be added using strategies such as embedding in viscous liquid polymers or heated solid polymers. Alternatively, deposition onto raised features creates self-sealed chambers [114]; subsequent capping

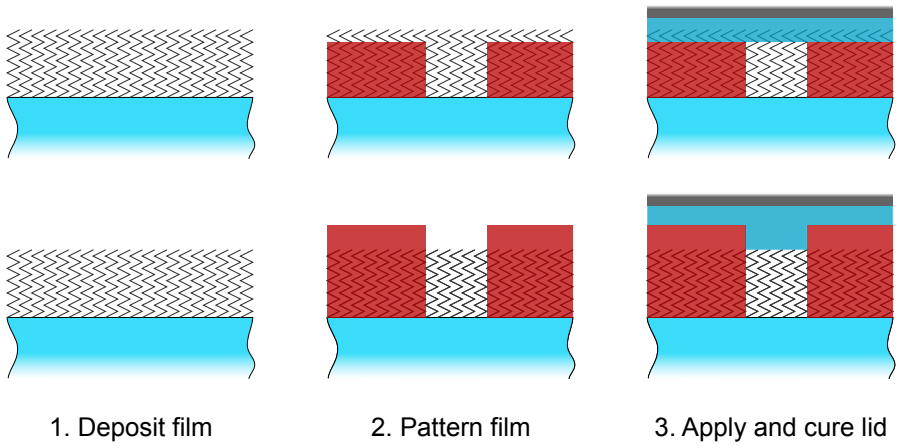

Figure 4.3: Microchannel fabrication by application of an adhesive or fluid capping layer, accommodating patterned channel walls that are either the same height (top) or higher (bottom) than the GLAD structures.

and reinforcement of the walls and lid would present a simple method for fabricating channels.

Formation of capping layers is complicated by compressive and tensile stresses within the solid cap. Figure 4.4 shows three SiO_2 films displaying the effects of tensile stress (a) and compressive stress on a thick (b) and thin (c) capping layer. SiO_2 is widely used for microfluidic devices due in part to a well characterized surface chemistry, availability of an array of versatile fabrication methods, large electrical resistivity, and optical transparency. However, SiO_2 is very susceptible to stresses arising primarily from three sources [115, 116]: thermal stresses due to expansion mismatches between film and substrate, intrinsic stress related to film growth (e.g. film density), and water-induced extrinsic stress caused by water molecule absorption in pores of the film (where finer pores, and hence denser films, create greater compressive stress due

to higher inter-molecular repulsive forces).

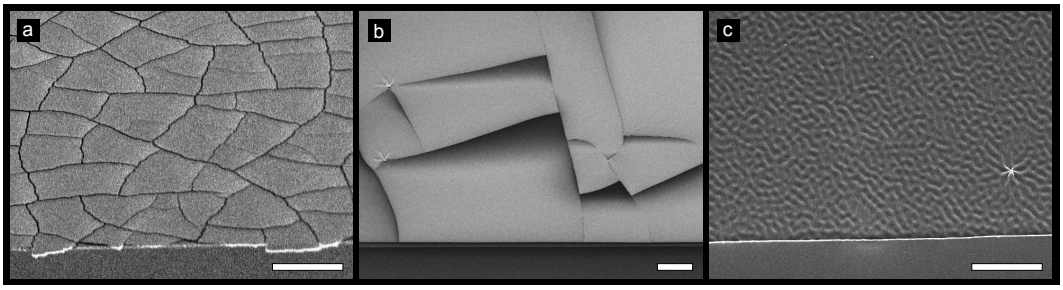

Figure 4.4: Three capped SiO_2 films with tensile (a) and compressive (b), (c) stress in the soild capping layer. Solid layer thicknesses were 400 nm (a), 670 nm (b) and 215 nm (c). Scale bars indicate 50 μm.

Thermal expansion mismatches are not a concern for GLAD capping layers as they are suspended above the substrate by the very porous GLAD film; however, thermal stresses can contribute to deformation of capping layers. The intrinsic and water-induced extrinsic stresses are more significant in the case of SiO_2 capping layers. The intrinsic stress can be controlled via adjustment of film density by altering either the chamber pressure or substrate temperature during film deposition [115]. A transition from compressive to tensile stress occurs as the pressure is increased or the substrate temperature is reduced. This provides a method for depositing stress-free SIO_2 capping layers, where the deposition conditions are adjusted to create a cap under tensile stress, striking a balance with water-induced compressive stress.

Figure 4.5 shows films with either a thick or a thin capping layer, deposited at different chamber pressures. All six films were deposited using the same deposition algorithm (2 μm thick two-turn hexagonal spirals with a ~200 nm solid cap), and

for the indicated films a thick capping layer was created by depositing an additional 200 nm layer at normal incidence. Compressive stresses within the solid layer caused the films to buckle, creating a dimpled orange-peel like surface on top of the films. Concurrent damage to the underlying GLAD film due to compression or stretching of the posts (correlated with location under a fall or rise of the capping layer) was also observed. A second order of buckling can be seen for the films with thicker capping layers (bottom row). A transition from compressive to tensile stress was present with increasing pressure from 1.4×10^{-4} Torr to 4×10^{-4} Torr, as evidenced by the change from a buckled cap (Fig. 4.5(b)) to a cap consisting of isolated mesas separated by fissures in the solid layer (Fig. 4.5(c)). Figure 4.5(f) shows a film that is near the transition but still under compressive stress, with reduced buckling compared to the lower-pressure films (Fig. 4.5(d), (e)).

A thorough empirical study may identify the ideal conditions for depositing a stress-free SiO_2 capping layer. However, the film stress continues to evolve with time, becoming more tensile over a span of days and months, so optimal conditions will change depending on intended device use. Alternatively, a material with lower intrinsic stress and lower susceptibility to water-induced stress could be used as the capping layer. For example, Kupsta *et al.* recently reported growth of low stress TiO_2 GLAD capping layers fabricated with substrate heating [117]. The entire film could be made from this material, or if the specific properties of a certain material are

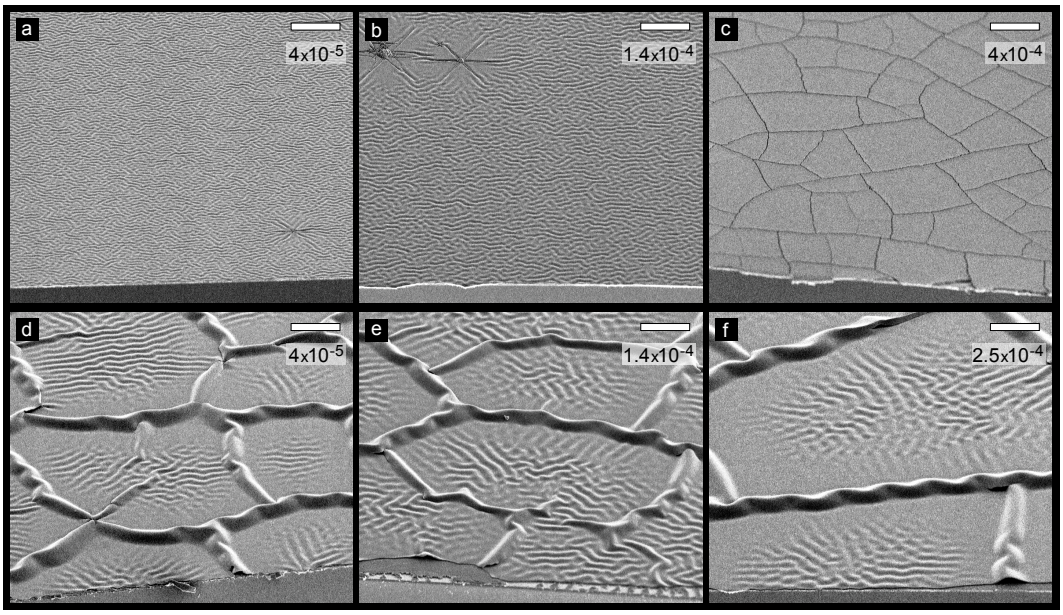

Figure 4.5: SiO_2 two-turn hexagonal spiral films (2 μm thick) with thin (~200 nm) capping layers (top row) or thick (~ 400 nm) capping layers (bottom row) deposited at increasing chamber pressures (pressures, in Torr, are shown for each film). Chamber pressure was regulated by adjusting oxygen gas inflow rate. Scale bars indicate 50 μm.

desirable, a bimaterial film could be deposited with a stress-free film capping the desired structures and material.

A final concern with capping layers involves particulate debris on the substrate, which could cause voids in the cap, causing a leak in the microfluidic channels. Such a defect is a concern in any microfluidic channel fabrication strategy, but in the case of capping layers could be addressed by sealing the caps with a viscous material or by vapor deposition of a thicker solid film. While a promising candidate for microchannel fabrication, the capping layer approach requires significant development before becoming a viable alternative to the approach used in this chapter.

The sacrificial method presented in this chapter proved to be the most versatile and reliable fabrication method of those considered. With further development, other methods may also prove to be suitable for microchannel fabrication, further expanding the GLAD microfluidics toolbox.

4.2.4 DNA Separation

To perform a molecular separation, we fabricated DNA fractionators based on the design by Zeng *et al.* [83], replacing the self-assembled porous colloidal array with SiO_2 GLAD structures. A vertical post film was deposited by continuously rotating the substrate at a rate of one revolution per 50 nm of film growth, at a deposition angle of 85°. This film has a porosity of approximately 80% [58]. The posts were then encapsulated in PDMS channels using the procedure outlined above. A brief mask-less second exposure during lithography removed a thin layer of photoresist, exposing the tips of the posts; these tips were subsequently embedded in the PDMS channel ceiling, creating a seal that prevented fluid shunting between the ceiling and top of the posts.

The device fluid reservoirs were filled with 4× TBE solution to reduce electroosmotic counterflow. The PDMS hydrophobicity prevented TBE from entering dry channels; this problem was circumvented by first wetting the channels with methanol, then replacing methanol in the fluid reservoirs with TBE solution. DNA mixture –

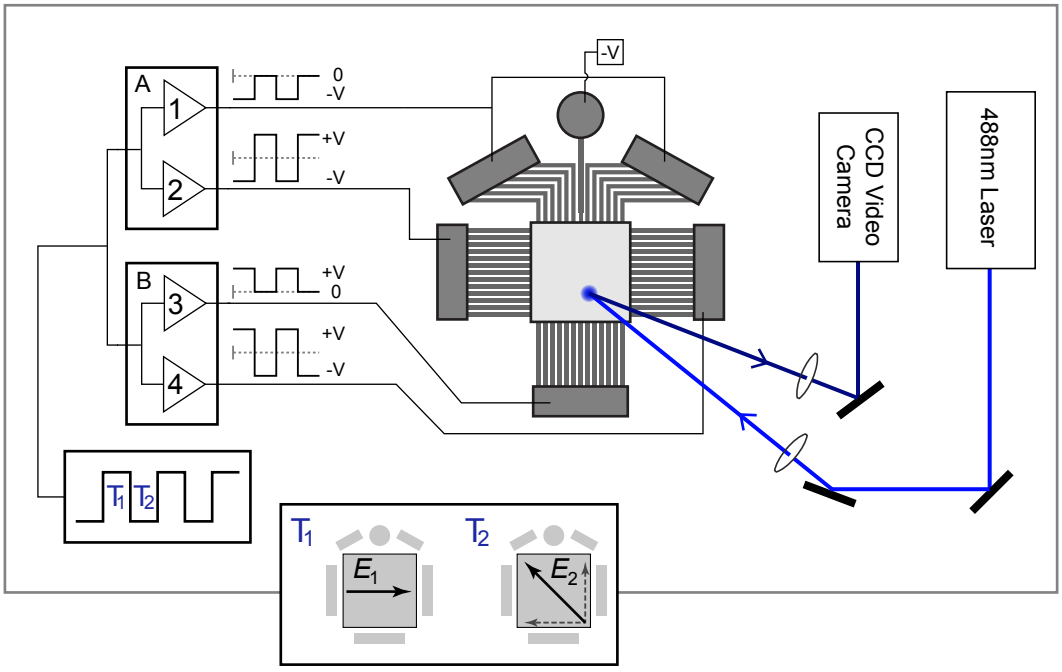

Figure 4.6: Schematic of the electrical and optical apparatus used for DNA fractionation. DNA is injected into the square separation array at the center of the device by application of a negative potential via the round reservoir at the top. A square wave signal is modulated and amplified, and the output is applied to four buffer wells (outputs 1–4) on the fractionation chip. This establishes two alternating net fields (shown in inset) over the square separation array in the center of the device that effect the DNA separation. The dye-stained DNA is visualized via laser excitation and subsequent CCD video camera image capture through a microscope objective. The optical interrogation area can be rasterized over the chip surface via a mechanical two-axis stage.

6/10/20 kbp or 10/48 kbp – was added to the inlet reservoir.

The apparatus and separation protocol, developed by Zeng and Harrison, have been discussed in detail elsewhere [83, 118] and are briefly introduced here. Figure 4.6 shows a schematic of the instrumental setup. DNA is continuously injected by an applied electric field into a square chamber containing a sieving matrix .

When describing DNA movement through such a porous matrix, it is useful to

model the DNA strand as a semi-flexible polymer composed of multiple stiff segments of length p – the persistence length – chained together by flexible joints. This length depends on a number of factors including repulsive electrostatic forces within the chain and the ionic strength of the solution the DNA is in, and is typically about 50 nm (150 base pairs) [119]. This is often recast in terms of Kuhn lengths, $l_{Kuhn} = 2p$, where a DNA molecule of length L consists of a number of Kuhn lengths, $L = l_{Kuhn}N_{Kuhn}$. A free-floating DNA molecule in solution will coil and fold up into a spherical 'blob' with an average radius $R_G = l_{Kuhn}N_{Kuhn}^{1/2}$ (the radius of gyration).

DNA strands are negatively charged as a result of charged phosphate groups that form the backbone linking together the nucleotides. This charge permits migration of DNA in solution by application of an electric force. However, the electrophoretic mobility of large DNA molecules free in solution is independent of size due to screening of the backbone charges by counterions in the solution [119]. Consequently they are not easily separated by electrophoresis in free solution, but this can be rectified by migration through a porous matrix instead.

Electrophoretic movement and separation of DNA through a porous matrix depends on the relative size of matrix pores and the DNA radius of gyration. The movement is described by the Ogston sieving regime when R_G is smaller than the pores, the biased reptation regime when R_G is larger than the pores, and the entropic trappic regime when the two sizes are approximately equal. Discussion of the three

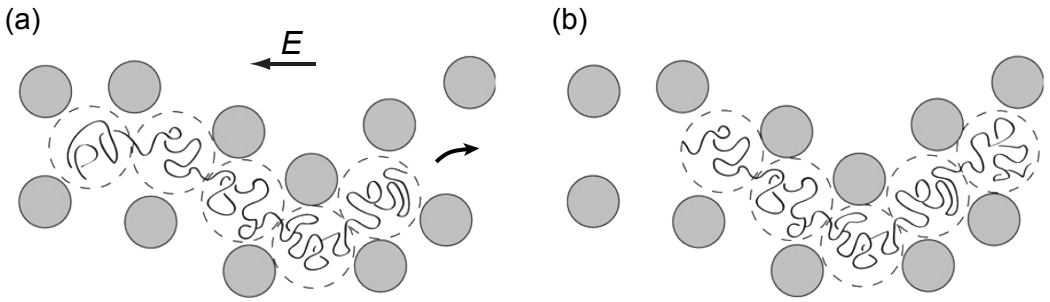

Figure 4.7: DNA forms multiple 'blobs' when confined to pores smaller than its radius of gyration. The DNA moves under an applied electric field through the porous matrix by reptation – a snake-like movement – in the opposite direction of the field [119]. Reproduced by permission of The Royal Society of Chemistry.

regimes is beyond the present scope, but a solid introduction and overview of the topic can be found in reference [119]. In the present device, DNA movement can be described by the biased reptation model, as the radius of gyration is larger than the pore size, b ($R_G > \approx 1400$ nm and $b \approx 100$ nm). The semi-flexible DNA polymer can conform to pores smaller than R_G when confined to the porous matrix by assuming a tube-like configuration of multiple connected 'blobs' (Figure 4.7) [119]. The DNA chain reptates (moves snake-like) through this tube under the applied electric force, moving head-first with the head forming new 'blobs' as the tail 'blobs' disappear – that is, the electric field causes biased reptation of the negatively-charged DNA in the direction opposite to the applied field. When the field reverses, the migration direction reverses, with the tail becoming the head under the reversed field.

Reptation of the DNA through the porous matrix results in a size-dependent electrophoretic mobility, and as a result DNA molecules of different sizes can be

separated by electrophoretic migration through a porous matrix under a constant field [119]. However, when the molecule sizes exceed approximately 1 kbp, resolution decreases and the separation times become impractical [119, 120]. Many alternate approaches have been developed to separate larger DNA molecules, such as pulsed field gel electrophoresis and the DNA fractionator device used here (also known as a DNA prism), which provides fast and continuous separation and sorting [83, 120].

An alternating asymmetric electric field applied across the separation chamber fractions the DNA into streams of different DNA sizes. The electric field changes its direction between one which is perpendicular to the DNA inlet (E_1) and the second one which is oriented 135° relative to the first one, with a vertical component pointing towards the DNA inlet (E_2).

Fractionation is a direct result of the relative displacement that occurs when DNA strands of different lengths but similar mobility in the sieving matrix are ratcheted by asymmetrical fields (illustrated in Figure 4.8) [118]: once the electric field is applied, DNA molecules stretch and migrate in the opposite direction of the field, led by one of their ends. When the electric field direction is changed, the molecules start to reorient themselves and backtrack to the new direction led by the head that was previously the tail. As a result, DNA molecules backtrack to different positions based on their molecular size; larger DNA molecules deflect more compared to the smaller molecules, so different DNA sizes can be separated.

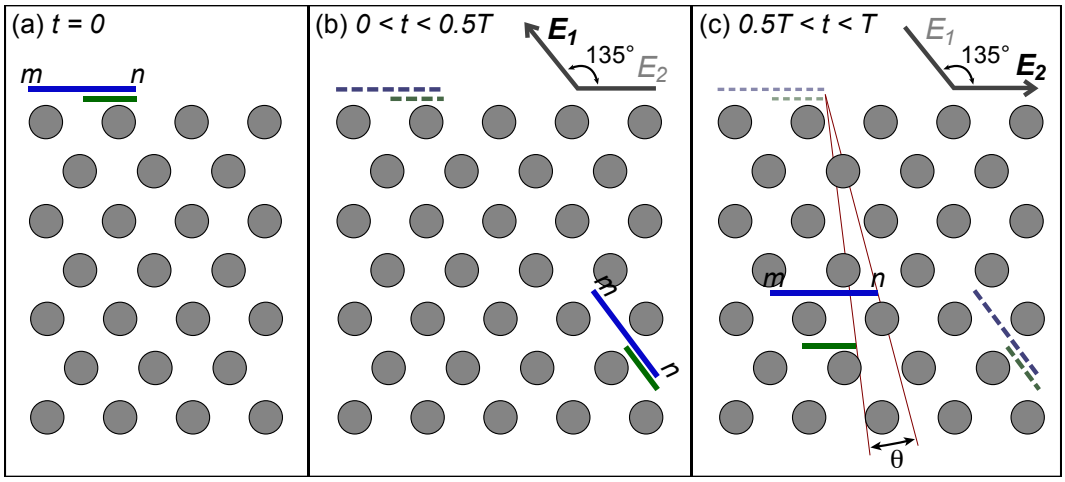

Figure 4.8: DNA molecules with similar mobility but different size are separated under a periodic asymmetrical field by a ratcheting mechanism in the fractionator. (a) Two molecules of different size start at the same origin at time $t = 0$. (b) A diagonal field in the interval $0 < t < 0.5T$ pulls the molecules down and to the right, led by end n. (c) A horizontal field in the interval $0.5T < t < T$ pulls the molecules to the left, now led by end m. This ratcheting motion results in gradual horizontal separation of the two molecules as they move downwards; in the device this is evident by formation of angularly separated DNA streams (θ). Reproduced in modified form with permission from [118]. © 2009 Wiley-VCH Verlag GmbH & Co. KGaA.

In all of our experiments $E_2 = 1.4\,E_1$. The electric field (E_1) was varied between 85 and 260 V cm^{-1}, while the frequency was varied between 0.1 and 20 Hz to obtain optimum separation resolution.

4.3 Results and Discussion

Complete infiltration of photoresist into GLAD films is necessary for the sacrificial process presented here. Figure 4.9 shows two different GLAD films filled with HPR 506 photoresist before and after short UV exposures and subsequent development. The deposited structures are firmly embedded in the photoresist. The figure also

demonstrates how short exposures can be used to controllably reveal the structure's top. In Figure 4.9(a), the tips of SiO_2 vertical posts are increasingly exposed as the exposure time increases from 0.4 s to 1.2 s; Figure 4.9(b) shows the overburden being removed from a Si chevron film by exposure for 1.2 s through a chrome mask (with no exposure on the masked left side) and subsequent development of exposed resist. The overburden thickness can similarly be controlled by adjusting the exposure time. Figure 4.10(a) shows how AZ P4620 thickness on a bare substrate could be adjusted by increasing exposure times prior to development. Figures 4.10(b)-(c) show similar control over the thickness of AZ P4620 spun into a GLAD film. The change in thickness with exposure time is shown graphically in Fig. 4.10(e), illustrating the fine control available with this process. Similar results were obtained for HPR resists.

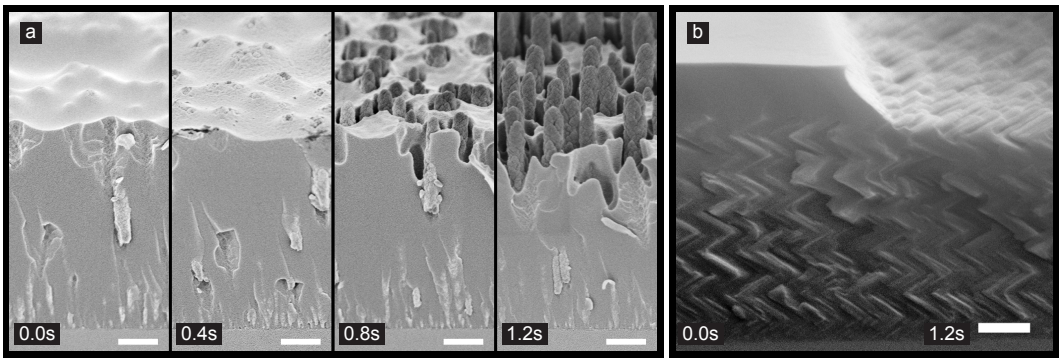

Figure 4.9: Scanning electron micrographs showing how the amount of photoresist removed to reveal the underlying structures changes with UV exposure times (shown in seconds) for (a) vertical posts grown at $\alpha = 88^\circ$ with little overburden and (b) chevrons grown at $\alpha = 85^\circ$ with noticeable overburden. Scale bars indicate 1 μm.

The photoresist overburden thickness remaining on top of the structures after spinning in the resist depended on a number of film properties, including porosity (i.e.

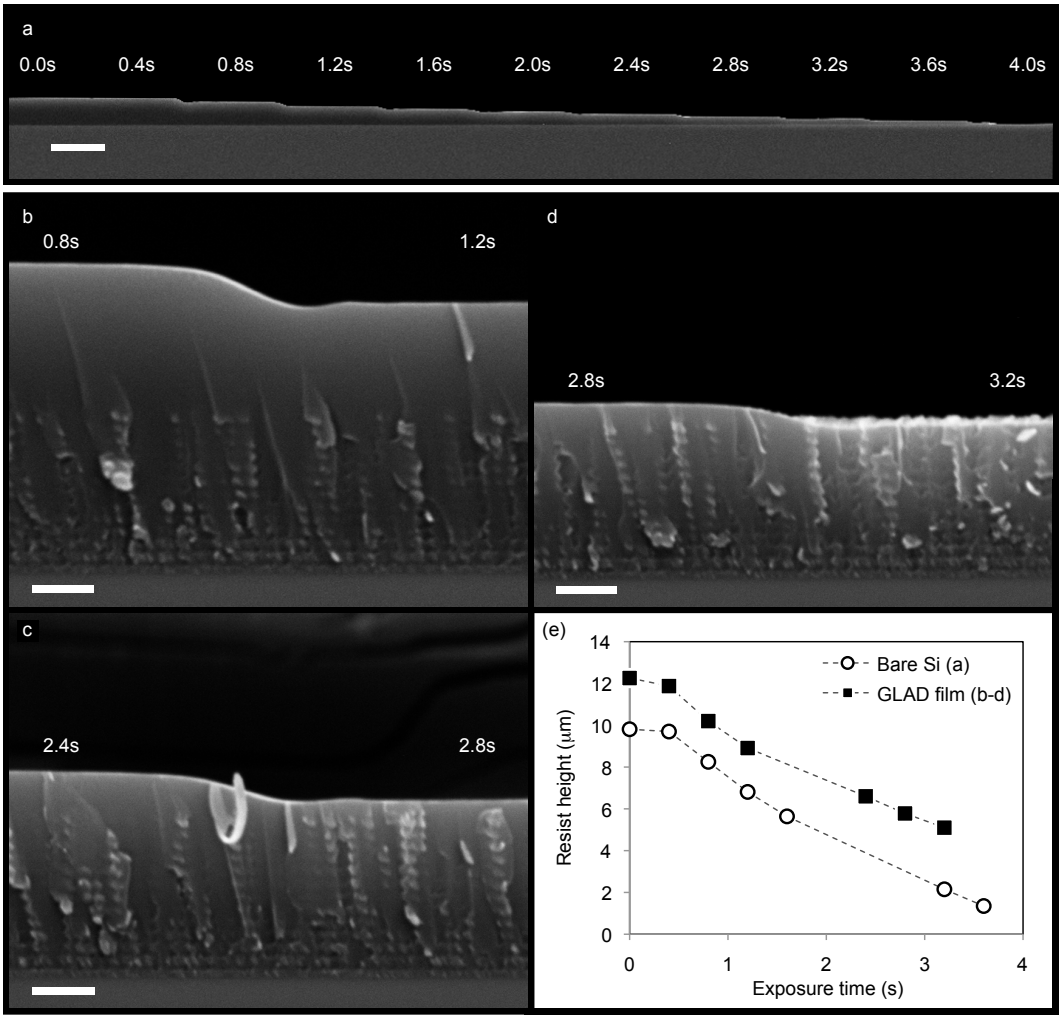

Figure 4.10: (a)-(d) SEMs demonstrating how short exposures and subsequent development will remove small, controllable amounts of photoresist from the top of the overburden. (a) AZ P4620 spun onto a bare Si wafer, exposed for the indicated times and developed for 40s. (b)-(d) AZ P4620 spun into an SiO_2 GLAD film. (e) Graph of the photoresist height after development, for the two substrates shown in (a)-(d). Scale bars indicate 20 μm in (a) and 2 μm in (b)-(d).

deposition angle), material, architecture, and height. For a given film, the overburden thickness depended on the spin speed and resist viscosity. The overburden was reduced with thicker and/or more porous (lower density) films, less viscous resists, or faster application speeds. The devices discussed in this report were fabricated using HPR 506 resist, which left a thin overburden on films approximately 5 μm high. Other resists such as HPR 504 (a less viscous resist) and AZ P4620 (a more viscous resist) have also been successfully used for this process. For the film thicknesses used here, the less viscous resist sometimes caused compressive deformation of the films, discussed below, or incompletely filled the film, while the more viscous resist formed an unnecessarily thick overburden.

As the spin-in speed was increased, the overburden thickness decreased, until a threshold speed was reached where almost no overburden remained. At this threshold, there is a transition from an overburden to a thin layer of photoresist that coats the top of the GLAD film. Increasing the speed further did not reveal increasing amounts of film; instead, we observed film compression by the thinning photoresist layer at higher speeds. Figure 4.11 shows edge-view SEMs of HPR 504 spun at increasing speeds into chevron GLAD films deposited at 80°, 84°, and 85°. The transition from overburden to thin coating of photoresist can be seen in the films deposited at 84° and 80°, when moving from 2500 rpm to 400 rpm. Compression is clearly visible at spin-in speeds of 5500 rpm.

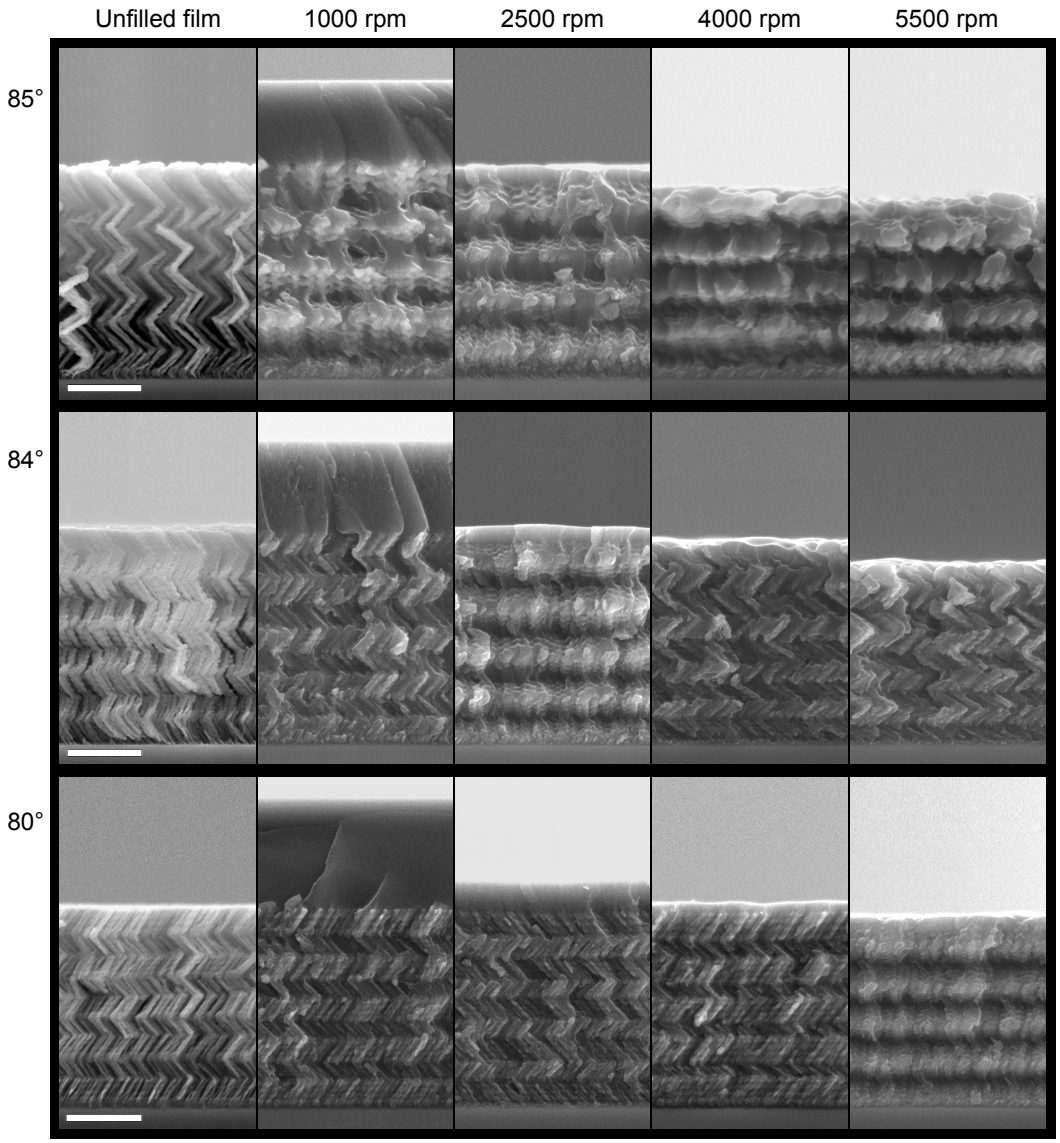

Figure 4.11: Scanning electron micrographs of chevron films deposited at $\alpha = 85°$ (2.9 μm thick), 84° (3.0 μm thick) and 80° (2.7 μm thick), before (unfilled) and after spin-in application of HPR 504 at 1000 rpm, 2500 rpm, 4000 rpm and 5500 rpm. Scale bars indicate 1 μm; magnifications are identical across each row.

The centrifugal forces did not noticeably alter the vertical orientation of the GLAD structures at low spin speeds, where an overburden remained. However, the film compression observed at speeds past the overburden threshold indicated that some deformation was likely present at higher speeds. Examination by scanning electron microscopy suggests that the source of this compression depended on film architecture, and was possibly due to deformation of the film by spring-like compression, tillting of the columns in the case of incompressible structures (e.g. vertical posts), or a combination of the two mechanisms.

Further visual evidence of this compression is given in Figure 4.12 for two separate films. Exposure and development of the compressed film released the structures, seen most clearly in Figs. 4.12(c) and (f). The measured heights of the developed regions corresponded with the original film heights, whereas the photoresist-filled areas were thinner. This confirms that the observed change in height was the developed film returning to its original height rather than expanding past that height.

The resist thickness, and the amount of compression, depended on the film thickness and the film porosity. Figure 4.13(a) shows the HPR 504 resist thickness as a function of spin-in speed for films deposited at 84° to thicknesses of 1.0 μm, 3.0 μm, and 4.7 μm. Figure 4.13(b) shows the resist thickness normalized to the pre-spin-in height, showing compression of the two thicker films as the normalized thickness dips below unity. As one would expect, the thicker film is compressed to a greater

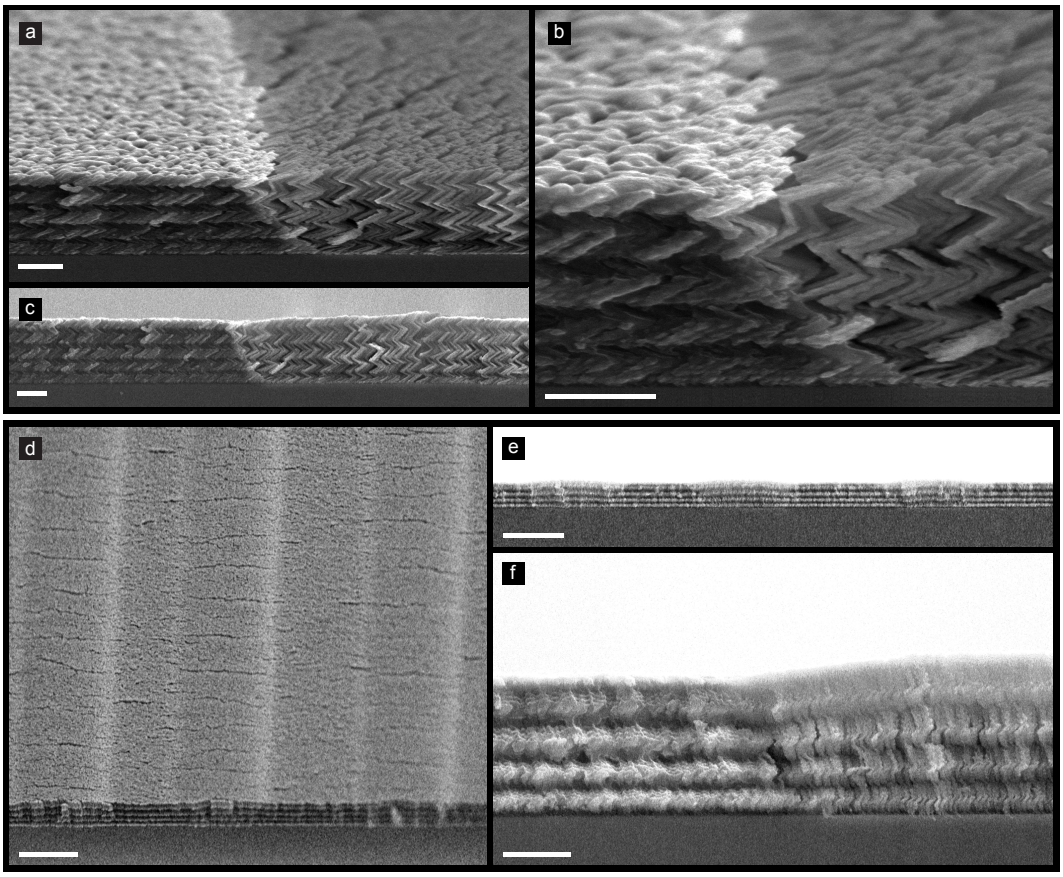

Figure 4.12: Compression and decompression of GLAD films by photoresist: (a) Oblique view SEM of an SiO_2 chevron film after photoresist patterning and development, showing slight film decompression of the developed (right) area compared to the compressed (left) area. The photoresist was spun-in at a speed of 5.5 krpm. (b) Magnified view of the transition between photoresist filled and emptied areas. (c) Lower magnification edge view SEM of the region in (a). (d)-(f) Similar views of an SiO_2 rectangular spiral deposited at 84°, where the photoresist was spun-in at a speed of 5.5 krpm. Scale bars indicate 1 μm in (a)-(c), (f), and 5 μm in (d)-(e)

extent. The overburden was also much thicker on the thinner film, remaining at a thickness of 500 nm even at a speed of 5500 rpm. The 4.7 μm film was compressed at speeds as low as 1000 rpm; consequently more viscous HPR 506 was used for films 4 μm and thicker.

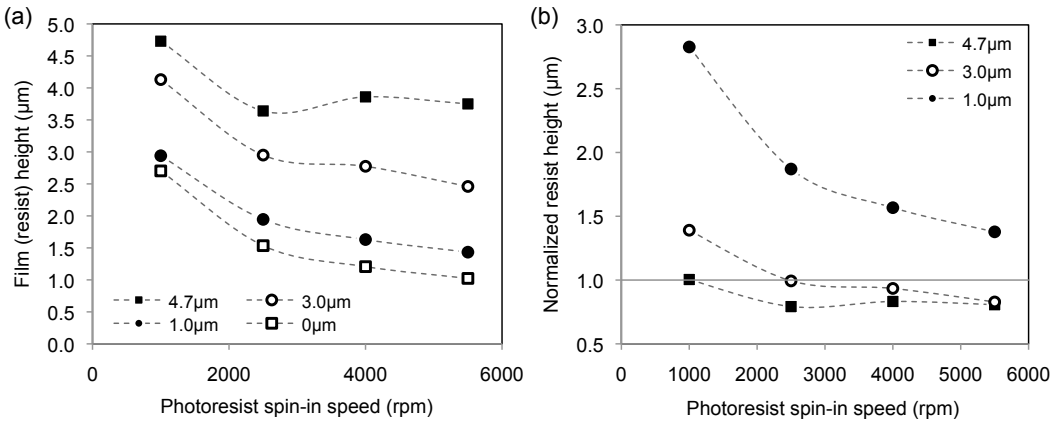

Figure 4.13: (a) Measured heights of chevron films deposited at an angle of 84° to three thicknesses (1.0 μm, 3.0 μm, and 4.7 μm) and a bare silicon wafer (0°), after spin-in application of HPR 504 at 1000 rpm, 2500 rpm, 4000 rpm and 5500 rpm. (b) Measured heights divided by the unfilled film height, showing compression of films with a ratio below 1.0 (as indicated by the horizontal grey line).

The dependence of resist height on film porosity is seen in Figure 4.14, where HPR 504 was spun into films ~3 μm thick, deposited at 80°, 84° and 85°. The resist is thicker on the 80° film, suggesting that the overburden thickness is related to the film porosity – the larger the volume available in the GLAD film for resist penetration, the thinner the overburden layer, for equivalent heights of film. At the same time, onset of compression came later for the more dense film, as can be seen with the normalized resist heights (Fig. 4.14(b)). The observed lower compression of the denser film was

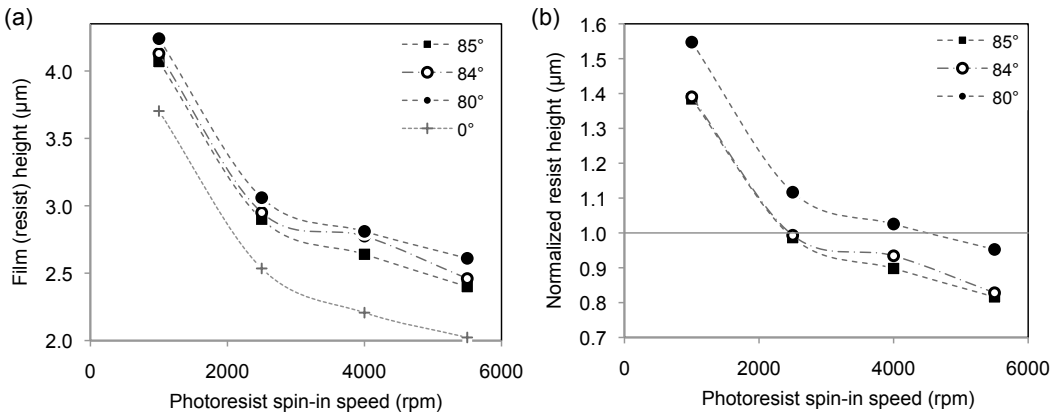

Figure 4.14: (a) Measured heights of chevron films deposited at deposition angles of 85° (2.94 μm thick), 84° (2.97 μm thick) and 80° (2.74 μm thick), and a bare silicon wafer (0°), after spin-in application of HPR 504 at 1000 rpm, 2500 rpm, 4000 rpm and 5500 rpm (SEM of films are shown in Figure 4.11). The 0° line has been shifted up by 1 μm to facilitate comparison. (b) Measured heights divided by the unfilled film height, showing compression of films with a ratio below 1.0 (as indicated by the horizontal grey line).

expected, given that the increased amount of material present in the film will increase its compressive strength. The curves are remarkably similar regardless of compression (comparing 84° and 85° to 80°), which would indicate that the film height has a diminished role compared to the porosity in determining the resist thickness for these very porous films.

While evidence of compression is clear, the mechanism responsible for this effect is still uncertain. Photoresist is applied to the substrate as a solvated polymer or resin (primarily novolac dissolved in ethyl lactate in the case of HPR 504 resist, with a 35% solids concentration). One possible mechanism of compression is formation of a 'skin' or more viscous layer on top of the resist during spin-in as a consequence of solvent evaporation from the surface. Such a skin could exert a downwards force on the film

as the resist layer thickness decreases, but evidence suggests that solvent evaporation during spin-in is negligible [121] and thus this mode of compression is unlikely. The majority of solvent is removed by the soft bake that follows resist spin-in, resulting in significant shrinkage of the photoresist layer [122]. This shrinkage is a more likely source of the observed compression.

Figure 4.15 shows cross sectional scanning electron micrographs (SEMs) of fabricated channels before and after resist dissolution, revealing how both the photoresist and PDMS completely infiltrated the GLAD film, with a clear boundary forming between the two polymers. Resist removal was selective, leaving behind GLAD structures surrounded by PDMS walls. The structures in Figure 4.15(a) are slightly embedded in the PDMS ceiling and no deformation or clumping of the film was observed other than a few posts dislodged by the SEM sample preparation process. The top ~ 1 μm of the vertical posts in Figure 4.15(b) are firmly embedded in the PDMS. The posts in the foreground were fractured during the cleaving process with the top half removed along with the PDMS; these short posts subsequently clumped during the drying process. It is difficult to see the inter-pillar spaces in the exposed vertical post film due to the mixed-detection mode necessary to limit charging effects that can saturate the detector during SEM imaging of this sample; however, close inspection of the pillar surfaces revealed the roughened morphology characteristic of SiO_2 GLAD posts, confirming removal of the photoresist polymer from the channel.

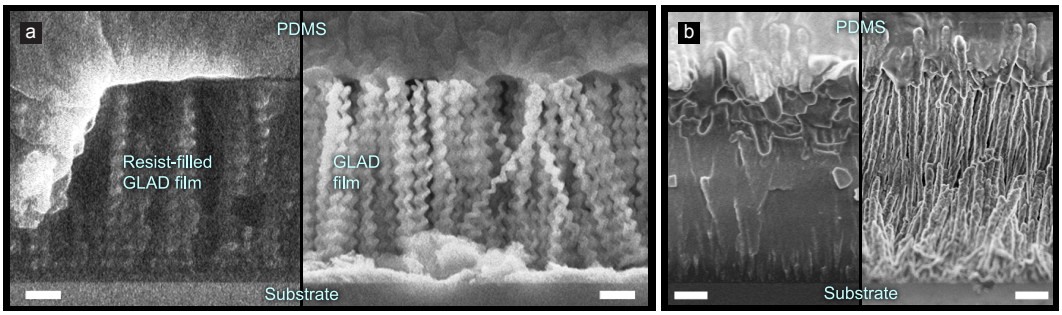

Figure 4.15: A microchannel containing GLAD-deposited (a) SiO_2 hexagonal spirals (α = 84.5°) and (b) SiO_2 micropillars (α = 83.5°) before (L) and after (R) removing the sacrificial photoresist. Scale bars indicate 1 μm.

Figure 4.16 shows various GLAD structures embedded in PDMS microchannels, demonstrating the flexibility of the process in making arbitrary structures for embedding in microchannels. Vertical posts such as those shown in Figures 4.9(a), 4.15(b), and 4.16(a) are most similar to structures that can be made using other methods such as microfabrication, where a geometry is etched downwards into the substrate. Figures 4.16(b)-(f) demonstrate how film architecture can be controlled during deposition to give various structures. Figure 4.16(g) and (h) shows a trimaterial, triarchitectural structure, where silver slanted posts have been sandwiched between silicon dioxide hexagonal staircase spirals and aluminum oxide square spirals. Figure 4.16(g) shows the emptied channel alongside the PDMS-filled film area that constitutes the channel wall. The film in Fig. 4.16(h) has been fractured at the Ag-SiO_2 interface during SEM sample preparation, with the square spirals embedded and retained in the elevated channel ceiling. It should be emphasized that in most cases, the material and structures are interchangeable – that is, the film shown in Figure 4.16(a) could

have been made with Si or TiO_2, and likewise the film in Figure 4.16(g) could have been made with the same structure but a different combination of materials. As with Figure 4.15(b), the interpillar spaces are difficult to see in Figures 4.16(c), (g) and (h) due to the SEM detection mode used to limit charging effects.

Figures 4.15(b) and 4.16(a) illustrate how the porosity for a given film architecture can be adjusted by changing the deposition angle – in this case, from 83.5° to 88°. As the deposition angle decreases, the intercolumn pores and column diameters become smaller. At the same time, the surface area increases to a maximum at approximately 60°, depending on film material [58]. In this way, devices can be tuned for specific applications: very high surface areas may be more desirable for some microreactors, small pores may be optimal for separating small molecules, whereas large pores may be best for separating large DNA strands or proteins. A combination of high surface area and large pores can be obtained by altering the deposition angle throughout film growth, shown in Figure 4.16(d).

The structures in Figures 4.16(b), (e) and (f) have in-plane anisotropy built into the film structure during deposition. Vertical pores in between the blade-like structures in (b) extend through the height of the film, but one can see from this image that the width of these pores depend on the direction one takes across the substrate (and hence through the film), with maxima and minima orthogonal to each other. The PDMS layer has been peeled off prior to photoresist removal, resulting in clumping of

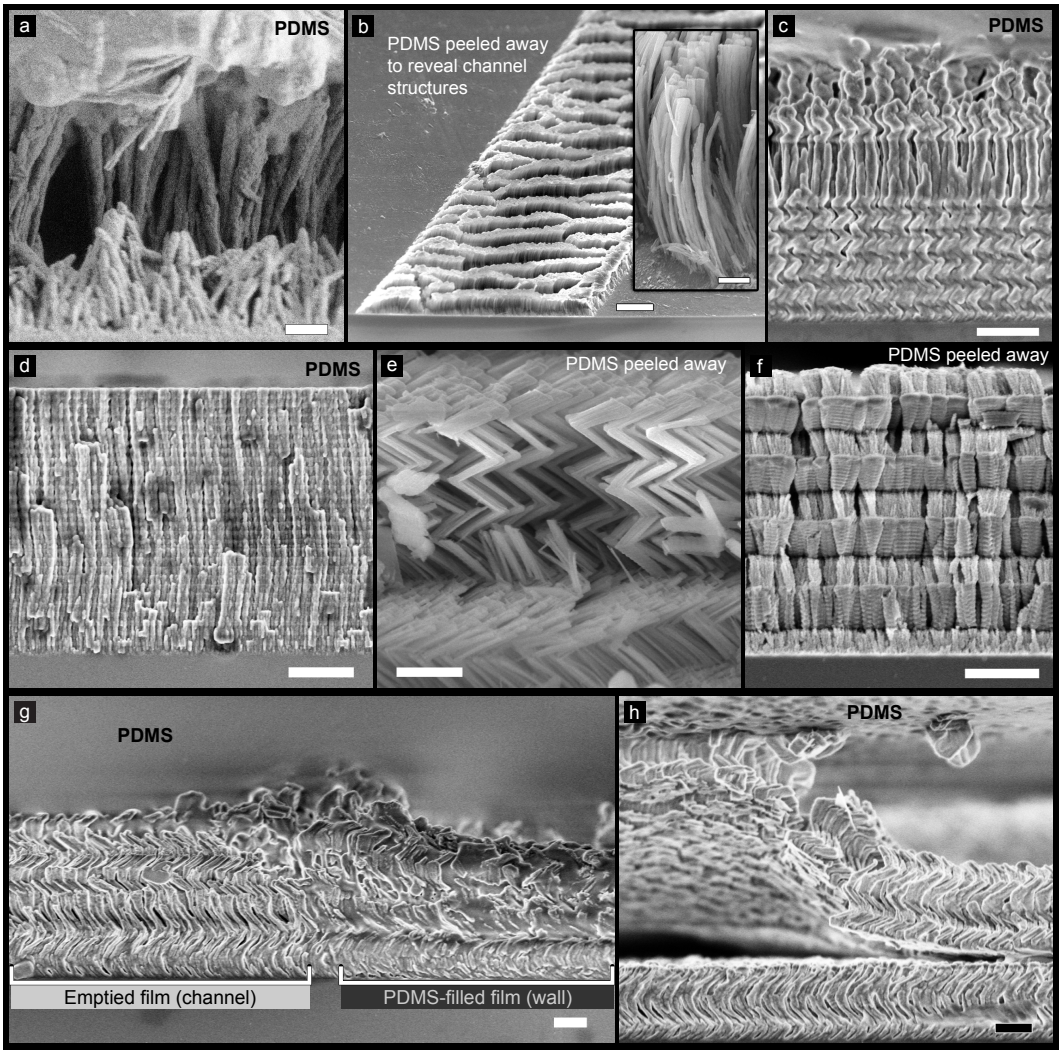

Figure 4.16: A few examples of structures that can be integrated in microchannels using glancing angle deposition: (a) SiO_2 vertical posts (α = 88°), (b) SiO_2 'blades' (α = 87°, inset shows magnified view of structures), (c) SiO_2 helix/vertical post/helix heterostructure (α = 84°), (d) TiO_2 periodically graded density film (α oscillating between 60° and 80°), (e,f) Si chevrons (α = 85°) and (g,h) SiO_2 hexagonal spiral / Ag slanted post / Al_2O_3 square spiral heterostructure (α = 85°). Scale bars indicate 1 μm in (a),(b,inset) and (c)-(h), and 10 μm in (b).

the bladed nanostructures, shown in closer detail in the inset. The blades are oriented with their flat faces pointing in the direction of the channel (vertically), and clumping is preferential between these high surface area flat sides resulting in the formation of horizontal lines of clumped structures. The chevron structure in (e) and (f) has a more pronounced in-plane porosity difference, with narrow pores along one direction (f) and wide, almost channel-like pores in the perpendicular direction (e). This kind of lateral asymmetry in microfabricated devices has been shown to provide novel separation schemes; for example, Fu *et al.* fabricated two-dimensional devices with laterally asymmetric channel heights to create a 2-D array for separation by either entropic trapping or Ogston sieving [71].

Changes in the substrate orientation during deposition can alter the film structure dramatically. This provides control over the column architecture throughout the height of the channel, as seen in Figures 4.16(c) and (e)–(h). Porosity differences arising from altering the deposition angle during growth correspond with density changes in the film, which in turn alter the effective optical index of refraction. Periodically graded density optical filters that transmit a pre-determined wavelength of light [35] and porous optically responsive humidity sensors [36] have been made using this effect. Figure 4.16(d) shows such a periodically graded density structure integrated into a microchannel. This film structure was created by oscillating the deposition angle between 60° and 80° to produce layers of high and low film density,

respectively. In this way, porous optical elements that can potentially respond to changes in the penetrating fluid can be built directly into microchannels. While not shown here, these porosity changes can be combined with architectural changes such as those in Figs. 4.16(c), (e) and (g) for an added dimension of structural control.

High aspect ratio micro- and nanostructures tend to clump or cluster together upon drying after immersion in liquids, possibly due to capillary forces acting on the structures as the fluid evaporates [101, 123]. Post-deposition ion-milling of posts [124] or specialized drying procedures, such as freeze drying [101] or critical point drying, can be used to minimize or eliminate this phenomenon. This kind of clumping in GLAD films has been shown to be predictable and dependent on film architecture [125], and thus may be exploited in some microfluidic applications where a bimodal micro/nano-porous pore distribution is desirable. The fabrication process presented here also provides another option for eliminating clumping when it is undesirable. When the tops of the columns are embedded in the PDMS ceiling (e.g Fig. 4.15(b)), clumping is eliminated. Fixation at the top and bottom prevents capillary forces from pulling columns together during the drying process. In Figure 4.16(a) and (h), SEM sample preparation fractured the films, and the subsequent post clumping after drying is evident in these images, but absent in the fixated posts in Fig. 4.16(c) and (g). One can also observe the holes left behind in the PDMS ceiling from the embedded posts that were ripped out during the cleaving process in Fig. 4.16(h).

The tendency for PDMS to swell when immersed in solvents [126] has to be taken into consideration in this fabrication process. Swelling from certain solvents, e.g. isopropanol and acetone, was found to be severe enough to cause delamination of PDMS from the substrate surface for some of our devices. We found that neither 1-methyl-2-pyrrolidone nor methanol caused an appreciable amount of swelling, even after soaking PDMS over a number of days. Consequently 1-methyl-2-pyrrolidone was used instead of acetone to dissolve the sacrificial photoresist, and methanol was preferred for removing 1-methyl-2-pyrrolidone from the channels. As with any PDMS-based device, this has implications on the solvents suitable for regular use within the device.

4.3.1 DNA Separation

We fabricated a fractionation device that confirmed GLAD posts could act as a porous matrix for DNA separation. Figure 4.17 reveals the porous vertical post film used for this separation, prior to integration into microchannels. Figure 4.18(a) shows a schematic of the microfluidic chip, where the separation chamber was filled with the GLAD posts shown in Fig. 4.17 as a sieving matrix. Using this device, a mixture of 10 kbp and 48 kbp DNA[2] was separated into individual streams, as shown in Figure 4.18(b). These streams can be collected into different channels at the end of

[2] Contour lengths are approximately 3.4 μm for 10 kbp DNA and 16 μm for 48 kbp DNA.

the separation chamber. Arrows indicate the direction and relative magnitude of the asymmetric electric fields applied across the chamber via the buffer reservoirs to effect the separation.

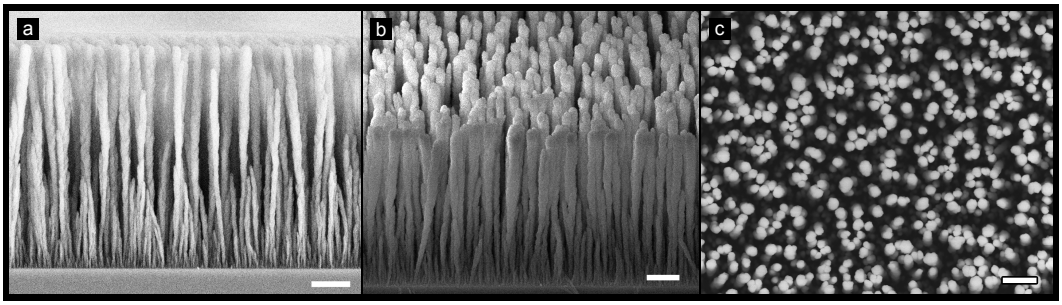

Figure 4.17: Scanning electron micrographs showing (a) side, (b) oblique, and (c) top views of the vertical post nanostructured thin film used for separating DNA. Scale bars indicate 1 μm.

Separation resolution is dependent on the pulsed field frequency; on this particular device, an optimum separation of 13.5° between 10 kbp and 48 kbp DNA was obtained at a frequency of 2 Hz (see Figure 4.19). Using an identical device (same porous film and fabrication process), we were also able to separate a mixture of 6, 10 and 20 kbp DNA into three separate streams at an optimum frequency of 15 Hz (data not shown).

TIRF microscopy was used to observe the migration mechanism of DNA molecules through the GLAD posts. Figure 4.18(c) shows seven sequential fluorescence images extracted from a captured real time movie of an isolated 48 kbp DNA molecule moving under fields of E_1 = 80 V cm^{-1} and E_2 = 112 V cm^{-1} at a frequency of 1.0 Hz, As seen in these images, DNA molecules stretch and move in an opposite direction to the applied field, usually led by one of their ends. Once the direction of the electric

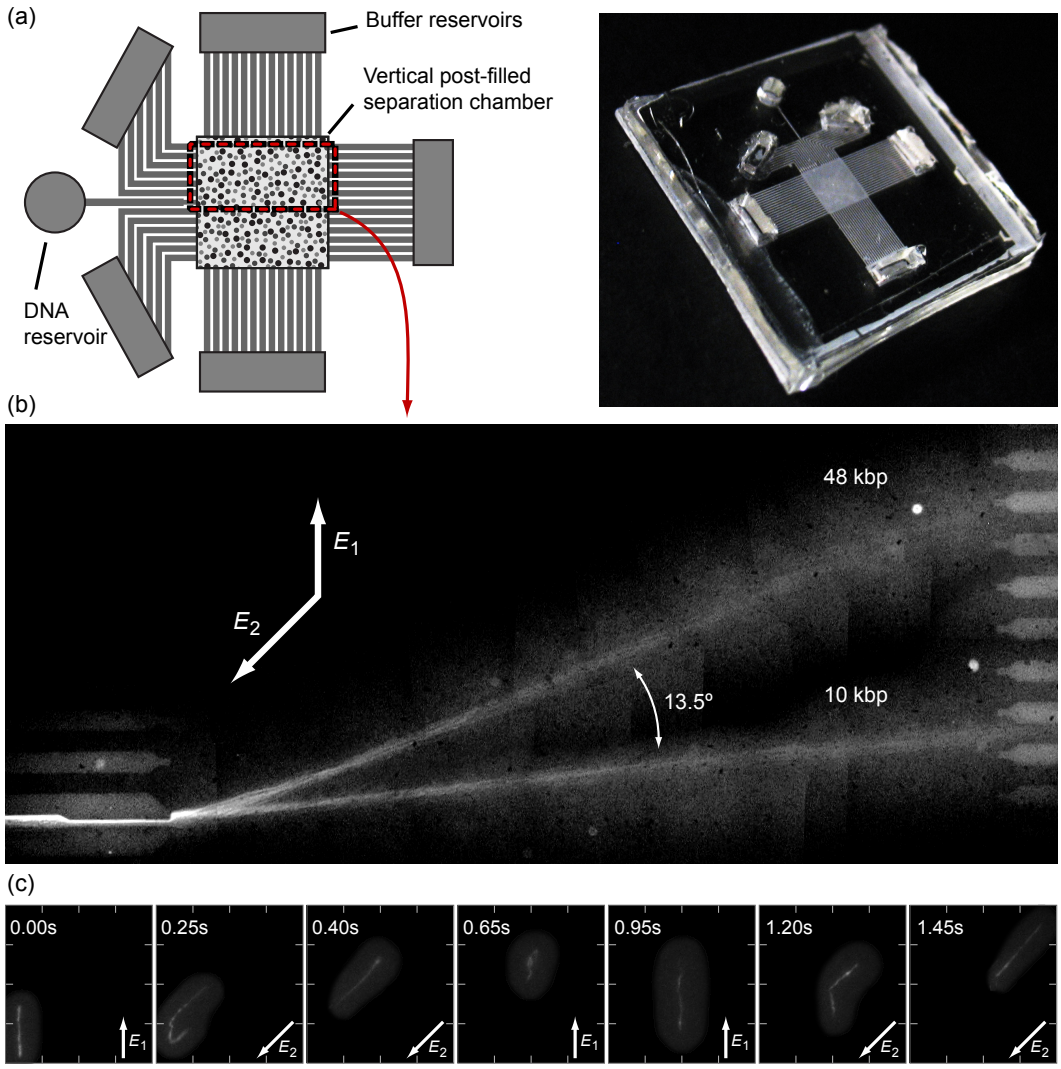

Figure 4.18: (a) Schematic (left) and photograph of a completed device (right) of the microfluidic chip fractionator used for separating DNA, filled with GLAD posts as a separation matrix. DNA mixture is injected from the reservoir into the separation chamber (left to right). Pulsed electric fields are applied across the chamber by platinum electrodes placed in the buffer reservoirs. (b) Fluorescence image of the separation chamber. Two different sizes of DNA, 10 kbp and 48 kbp, are injected into the chamber from the left and separate to form two different streams moving towards the collection channels at the end of the separation chamber. Applied electric fields were E_1 = 60 V cm^{-1} and E_2 = 84 V cm^{-1} as indicated by the arrows, switched at frequency 2 Hz. Image was assembled from multiple 320x200 px screen captures. The two white dots are debris, and the vertical steps in the DNA stream intensity are artifacts from assembling multiple screen captures. (c) Time elapsed fluorescence images (TIRF microscopy) of 48 kbp DNA molecules migrating in the separation chamber, with applied electric fields of E_1 = 80 V cm^{-1} and E_2 = 112 V cm^{-1} as indicated by the arrows, at frequency 1 Hz.

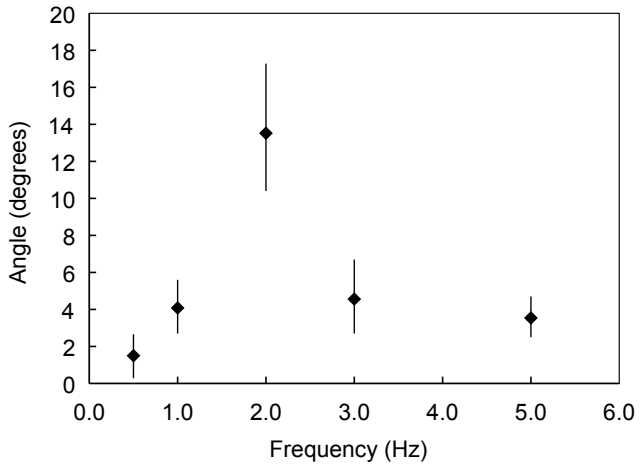

Figure 4.19: 10 kbp and 48 kbp DNA separation was highest at a frequency of ~ 2 Hz and angle of 13.5°.

field changes, the molecules are reoriented and backtrack away from the new direction, now led by the head that was previously the tail. Our observations show that the DNA migration mechanism under pulsed electric fields in GLAD post arrays is very similar to the migration mechanism of DNA molecules in nanoparticle arrays [83] and microfabricated post arrays [120].

This separation demonstrates that an unmodified GLAD film is effective as a separation matrix. We observed a small amount of dispersion in these preliminary separations, evident by broadening of the DNA streams as they progress through the array to the collection channels. This dispersion was quantified by calculating the fluorescence intensity profile peak variance σ of the 10 kbp stream shown in Fig. 4.18c. [127] Comparison of the variances at the injection point (σ_I) and at a point 2.6 mm downstream of the injection point (σ_T) allows for calculation of the

band broadening caused by contributing factors (σ_F) other than the injection, where $\sigma_T^2 = \sigma_I^2 + \sigma_F^2$. Such factors can include DNA diffusion, DNA size fluctuations, electric field gradient, and structural defects or disorders in the separation matrix. For the vertical post GLAD fractionator shown here, $\sigma_F = 20\ \mu\text{m} \pm 15\%$. This was the same as the dispersion, $\sigma_F = 18\ \mu\text{m} \pm 15\%$, on a similar device with a self-assembled nanosphere array matrix using the same size DNA and similar conditions [127] ($\sigma_T = 22\ \mu$m for both devices), despite distinct physical differences between the two matrices. The nanosphere array has a comparable porosity to the GLAD film (700 nm diameter silica spheres forming approximately 100 nm sized pores), but a very low amount of disorder and inhomogeneity in pore size and distribution in contrast to the GLAD film's high surface area and unoptimized larger pore size distribution.

The high surface areas present in nanopillar films can cause band broadening due to surface area dependent electroosmotic flow (EOF) [128]. The mobility for 48 kbp DNA in our device was $\mu = 2.5\text{x}10^{-5}\ \text{cm}^2\,\text{V}^{-1}\,\text{s}^{-1} \pm 15\%$, calculated using TIRF microscopy images ($E = 114\ \text{V cm}^{-1}$). This is comparable to the nanosphere array device, with similar porosity and negligible EOF, where $\mu = 2.8\text{x}10^{-5}\ \text{cm}^2\,\text{V}^{-1}\,\text{s}^{-1} \pm 15\%$ ($E = 114\ \text{V cm}^{-1}$). [127] Thus EOF was sufficiently suppressed by the buffer and is not expected to have played a role in band broadening.

Pore and column size inhomogeneity may cause dispersion during DNA fractionation [127]. As seen in Figure 4.17, there is a range of pore sizes present in GLAD

films as a result of column extinction and broadening during growth [21, 58]. The net effect is to create a pore gradient through the height of the film, with pore size increasing along the height of the film. This pore inhomogeneity is expected to have contributed to the observed dispersion in our device, and is likely also responsible for a significant portion of the background fluorescence observed during the separation – scattering of emitted light through the silica structures resulted in noticeable levels of background light.

Two strategies that have been shown to be effective in reducing this inhomogeneity within GLAD films could be used to optimize separations and minimize band-broadening dispersion: deposition onto pre-patterned substrates can create regularly spaced structures with very narrow and controllable pore size distributions [28, 129]; post-deposition ion milling can smooth columns while removing the remnant extinguished posts that contribute to the film pore gradient [124]. Both processes are compatible with the fabrication process described here.

4.4 Concluding Remarks

The increased surface area, controllable porous network structure, and varied morphologies of fabricated porous microchannels have found numerous uses in miniaturized systems. We have developed a fabrication method that provides a versatile technique for integrating nanostructures into microchannels, as demonstrated by

the various architectures and materials that can be integrated in channels using glancing angle deposition. Engineered three-dimensional Si, SiO_2, TiO_2, Al_2O_3, and Ag structures were grown with GLAD and incorporated into PDMS microchannels using a sacrificial etch technique. Separation of DNA mixtures (sizes between 6 kbp and 48 kbp) into individual streams in a fractionation array verified that this technique could be used to fabricate working microfluidic devices. To our knowledge, this is the first report of such a technique for creating microfluidic channels containing nano- and microstructures with engineered, controllable three-dimensional architectures.

LASER DESORPTION/IONIZATION COUPLED MASS SPECTROMETRY[1]

5

5.1 Introduction

Biomolecular separations are often coupled with mass spectrometry as a sophisticated method for identifying and quantifying the separated compounds. Matrix-assisted laser desorption/ionization (MALDI) is a widely used technique for introducing molecules into the mass spectrometer. A range of biomolecules, from small peptides to large molecules such as proteins (up to 100 kDa), can be analyzed by mass spectrometry with MALDI. An important advantage of MALDI as an LDI technique is that analyte molecules are minimally fragmented during the desorption and ionization process, permitting straightforward analysis and identification.

The two critical steps for obtaining mass spectra in laser desorption/ionization, as the name suggests, are desorption and subsequent ionization of the analyte molecules, a process that is faciliated by the matrix in MALDI. The presence of the energy absorbing matrix is critical in reducing analyte fragmentation. The desorption and ionization process is complicated and is still not completely understood [130, 131]. Briefly, the analytes are mixed in solution with a matrix compound, and co-crystallized

[1] A version of this chapter has been published in Ref. [108].

on a solid support. The matrix absorbs energy from an incident laser pulse (commonly used UV-wavelengths: 337 nm N_2 laser or 355 nm tripled frequency Nd:YAG laser), and the mixture is ejected into a vapor phase plume via a desorption or ablation process. Primary ionization events, either prior to crystallization or immediately after the laser pulse, and secondary ionization events during vapor phase expansion result in charge transfer to some of the analyte molecules. The charged molecules are pulled into the mass spectrometer by an electric field; in most cases a time-of-flight mass spectrometer (TOF-MS) – in which mass-based temporal separation over a known distance occurs – is used to detect the molecules.

A drawback of MALDI is the co-ionization of matrix molecules, which show up in the mass spectrum as low-mass noise (< 1 kDa). Small molecules such as drugs, peptides, and metabolic byproducts are of considerable interest to analysts; these molecules are masked by noise from the matrix, making analysis by LDI problematic. Other drawbacks of MALDI include the trial and error process used to select matrices, tedious sample preparation, and 'sweet spots' during LDI where the analyte is found only in discrete locations on the crystallized sample, separated by 'mute' spots, due to the crystallization process [132]. Wei *et al.* bypassed this problem by replacing the organic matrix with porous silicon, known as desorption ionization on silicon (DIOS) [133]. DIOS is one of the first and most widely used variations of surface-assisted laser desorption/ionization (SALDI) techniques, a technique first introduced by Sunner *et*

al. [132]. The laser energy in SALDI is absorbed by the substrate or some other dry, inorganic, non-desorbed particle instead of a matrix, and the analyte molecules are desorbed directly from the surface in a thermal process initiated by the light-absorbing surface structures. Figure 5.1 illustrates this key difference between MALDI and SALDI. The SALDI desorption process and the ionization mechanisms vary with the surface and are not yet fully understood, but it is generally accepted that the structural morphology, thermal properties, optical properties, porosity, and surface chemistry (among others) of the SALDI substrate all play a role in the mechanism [134–140].

SALDI has been reported on a wide range of materials structured with a variety of fabrication strategies, foremost of them silicon. Electrochemically etched porous silicon has been used by numerous groups after Wei *et al.*'s initial report [133, 134, 137, 141–152] Alternative methods for fabricating porous silicon, such as plasma enhanced chemical vapor deposition (PECVD) to create column/void nanostructures [153], and ordered nanocavity arrays etched into silicon via reactive ion etching (RIE) through self-ordered nanosphere arrays [154] or electron-beam lithography [137] etch masks, have also been employed. Reactive ion etching has also been used to make periodic silicon nanopost arrays [138]. Other silicon nanostructures (where the morphology is better defined by the structures rather than the porosity) for DIOS include nanowires grown by vapor-liquid-solid phase growth [155, 156], laser-induced silicon microcolumn arrays (LISMA) [157–159], Ag-colloid templated growth of

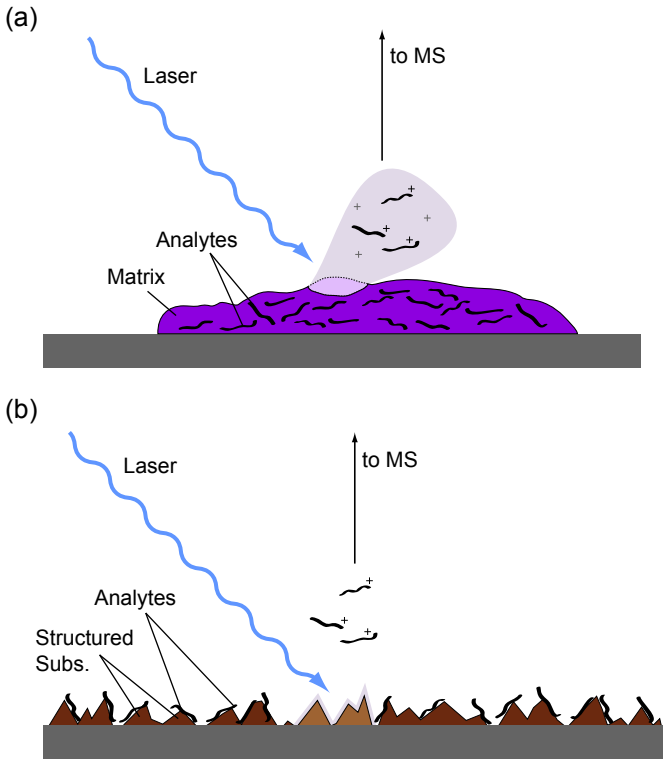

Figure 5.1: (a) Matrix and analyte molecules are ionized after laser-induced desorption of the matrix before being pulled into the mass spectrometer in MALDI-MS. (b) Analyte molecules are thermally desorbed from a structured surface and ionized before being pulled into the mass spectrometer in SALDI-MS.

nanowires [160], and thin PECVD-grown layers on various structured and insulating substrates [140].

Graphite flakes were the first substrate reported for SALDI activity [132]. Other carbon-based surfaces have included activated carbon powder [88], carbon nanotubes [161], a DVD coated with diamond-like carbon using pulsed laser deposition [162], and functionalized pyrolytic graphite polymer films [163]. SiO_2 has been used in the forms of silica gel [150], ordered nanoporous films structured by template removal

[164], and porous substrates made by complete thermal oxidation [165] or surface oxidation [146] of electrochemically etched porous Si. Electrochemically etched porous Al_2O_3 is not an effective substrate on its own, but has been shown to be a good scaffold for sputtered Au coatings [135, 136]; a nanoporous, nanopillar structure coated with atomic layer deposition (ALD) Al_2O_3 produced no signal in contrast to the same substrate coated with Si or TiO_2 [140]. TiO_2 has also been successfully used in the form of hollow nanotube arrays [166] and a mesoporous calcinated sol gel [167]. Au nanorods [168, 169] and a multilayer Au nanoparticle/polymer structure and thin sputtered Au films (where nucleation sites have not coalesced and are isolated) [170] have also been reported. A number of other structures and materials have been reported as effective SALDI substrates: wet chemistry prepared Pt 'nanoflowers' and sputtered Pt thin films [171] and nanoparticles formed by galvanic deposition and evaporation [172]; sputtered thin (70 nm) cobalt films [173]; porous, electrochemicially etched GaAs and GaN performance was compared to and found less efficient than porous Si [148]; Ge nanodots produced by molecular beam epitaxy (MBE) [139, 174]; ZnO nanowires/nanopillars fabricated by a vapor transport process [175]. Nanoparticles have also been reported as SALDI substrates, using materials including: Au [176–179], C [132, 180, 181], Ag [182], Si [183], Cu [179, 184], Ni [184], MnO [185], TiO2 [186], ZnO [187] and ZrO_2 [188]. Despite the wide range of materials and structures reported as effective SALDI agents, no single method has emerged as

superior to the others in terms of performance, stability, versatility, manufacturability, and ease of use. This has, in part, motivated continued research in this field.

Of these methods, porous silicon has received the greatest interest as a result of the good performance that can be achieved with DIOS substrates, along with the well characterized surface and microfabrication strategies that accompany the material. It seems that of all the materials, thus far silicon has had the optimal combination of high UV absorption, thermal and electrical conduction, surface chemistry, and "machineability" or methods of fabrication. Moreover, porous silicon surfaces allow integration with other functionalities such as in situ chromatographic separation [151] and analyte capture and purification steps prior to MS detection [189, 190]. The detection limits of DIOS-coupled mass spectrometry (DIOS-MS) for peptides are often comparable to MALDI (high attomoles), and in some cases can even greatly surpass them [189, 191]. Although the mechanism of DIOS is not fully understood, it is believed that porous silicon acts as a scaffold to retain the solvent and analyte molecules and also converts light into thermal energy, creating gas-phase ions upon laser irradiation [133–135, 147, 148, 192].

Electrochemical etching of silicon has been the predominant method used to prepare porous silicon surfaces for DIOS-MS applications [133, 143, 148, 151–153]. However, while achievable, obtaining reproducible surfaces using electrochemical etching techniques requires considerable care [193]. Alternative techniques such as

those mentioned above (PECVD [140,153], RIE [137,138,154], nanowires [155,156,160], LISMA [157–159]) have also been reported for generating porous silicon surfaces for DIOS applications. Some of these methods yield a broad range of pore sizes, depths, and densities on the same target surface and often lead to spot-to-spot and batch-to-batch performance variation. As in MALDI, the morphology of the porous substrate affects the ion yields in DIOS-MS [133–135,148,149,194].

Developing methods to reproducibly generate porous Si targets with optimal pore size, porosity and thickness is thus important and could have a significant impact on applying DIOS-MS to drug discovery, medicinal chemistry, metabolomics and proteomics screening [195]. This chapter describes how GLAD was used to fabricate nanostructured porous silicon thin films for DIOS-MS of small molecules. The surface structure, optical absorption and heat transfer properties of the target have been shown to be important influences on performance in DIOS [133,148,151,194], and all of these properties are easily manipulated in the GLAD process [20,34,36,38–40,196,197]. The fine control of substrate properties offered by GLAD techniques will offer opportunities for rationally designing the appropriate properties of the material as a DIOS substrate.

In the first part of this study [108], we examined the suitability of Si GLAD films for matrix-free detection of small peptides, drugs and metabolites in the mass range of 150-2500 *m/z* and compared the performance with MALDI and other LDI targets.

In the second part, we compared the performance of vertical post Si films deposited in the highly-oblique angle range of 79° - 87°. We also investigated the effect of tilting the GLAD columns with slanted post films, and looked at the response of other materials with GLAD-deposited Al, Ti, and Ni films.

The work presented in this chapter was originated by and performed in collaboration with Dr. D. Jed Harrison's lab in the Department of Chemistry at the University of Alberta. Abebaw Jemere assisted with mass spectrometry measurements, methods, experimental design and interpretation of the results. My contribution was the design and growth of the GLAD films, film characterization, design and implementation of experiments, and interpretation of the results as they relate to film structure and design.

5.2 Experimental

5.2.1 Materials and Reagents

Dopamine hydrochloride (MW 190), (±)-verapamil hydrochloride (MW 491), bradykinin, fragment 1-5 (MW 572), [Val^5]angiotensin-I (MW 1281), angiotensin-I (MW 1296), angiotensin-II (MW 1046), des-arg^9-bradykinin (MW 903), adrenocorticotropic hormone (ACTH) fragment (18-31) (MW 2464) and flavin mononucleotide (MW 455) were purchased from Sigma-Aldrich Chemical Co. (Milwaukee, WI, USA). Stock solutions were prepared by reconstituting lyophilized samples in water. Samples were

diluted in methanol/0.1% trifluoroacetic acid (TFA) (30:70, v/v) as needed and 0.5 mL aliquots were pipetted directly onto the GLAD films, then dried at room temperature to give spots ~2 mm in diameter. Up to five spots could be spotted on a 1 cm^2 GLAD film. The MALDI matrix α-cyano-4-hydroxycinnamic acid (CHCA), TFA and methanol were from Sigma-Aldrich. Solutions were prepared using ultrapure water prepared with a deionizing system (Millipore Canada, Mississauga, ON, Canada) from distilled water.

5.2.2 Porous Silicon Thin Film Fabrication

Nanostructured porous thin films were deposited by electron beam evaporation of the target material under vacuum (base pressure < 10^{-6} Torr) onto 3" and 4" diameter single crystal (100) silicon wafer substrates, which were subsequently cleaved by hand into 1 cm × 1 cm squares. Fused silica substrates (1" × 1") were also included in selected depositions for optical measurements on the thin films. Evaporation source material was puchased from Cerac Inc., Milwaukee, WI, USA: silicon (> 99.999% pure, 3-6mm pieces) and silicon dioxide (> 99.99% pure, 3-6mm pieces). All substrates were cleaned prior to deposition by submersion in piranha (3:1 sulfuric acid/hydrogen peroxide) for 20 min followed by a deionized water rinse, and dried by a nitrogen stream. Silicon vertical posts (columns) were deposited using GLAD at angles of either 1°, 70°, or in the range of 78.5° to 87° relative to the substrate normal, using

a substrate rotation rate of 1.2 rpm at a deposition rate of 0.4 nm s^{-1} - 0.9 nm s^{-1}. Slanted posts were deposited at angles of either 78°, 83° or 85°, with no substrate rotation at a deposition rate of 0.3 nm s^{-1}- 0.7 nm s^{-1}.

Optical transmission of selected films at 337 nm was measured at normal and 45° incidence to the substrate normal with a Lambda 900 UV/VIS/NIR spectrophotometer (PerkinElmer, Waltham, MA, USA). Scanning electron microscopy images were taken of uncoated samples using a Hitachi S-4800 field emission scanning electron microscope. Surface composition of aged Si GLAD films was measured using an AXIS 165 X-ray photoelectron spectrometer (XPS), equipped with a monochromatic Al Kα X-ray source (hν1486.6 eV). XPS atomic compositions and atomic ratios were calculated with the supplied AXIS software.

5.2.3 Mass Spectrometry

DIOS-MS measurements were made using an Applied Biosystems (Framingham, MA, USA) Voyager STR time-of- flight mass spectrometer operated with a pulsed N_2 laser at 337 nm at a repetition rate of 3.0 Hz. The beam is directed to the target by a mirror, and passes into the evacuated chamber through a fused silica window. It hits the target at an angle of approximately 45° relative to the substrate normal. The laser intensity of the Voyager STR mass spectrometer can be set between 0 and 4600 arbitrary units. The silicon substrates with nanostructured GLAD films (~1

cm^2) were attached to a modified MALDI target plate using a conductive carbon double-sided tape. Aged Si films were cleaned with a UV-O cleaner (model no. 42, Jelight Company, Inc., Irvine, CA, USA) for 15 min prior to sample deposition.

Positive ion mode mass spectra were acquired with the N_2 laser using the reflector, delayed extraction mode with an accelerating potential of 20 kV, a 74% grid potential, a 0.07% guide wire voltage and a delay time of 350 ns for peptides and drugs. Negative ion mass spectra were collected for flavin mononucleotide using the linear delayed extraction mode with an accelerating voltage of 18 kV, 96% grid potential, a 0.1% guide wire voltage and a delay time of 250 ns. Each spectrum is the result of 100 averaged laser pulses. Single laser shot spectra were also collected to determine the presence/absence of 'sweet-spots'. Signal-to-noise ratios were calculated using Voyager Data Explorer version 4.0 (Applied Biosystems, Framingham, MA, USA).

Where indicated, some DIOS-MS measurements were made using an AB SCIEX 4800 *Plus* MALDI TOF/TOF mass spectrometer, operated with a pulsed frequency-tripled Nd:YAG laser at 355 nm, at a repetition rate of 200 Hz. The beam is directed to the target via two 45° mirror reflections. In contrast to the Voyager mass spectrometer, the 4800+ beam hits the target at an approximately normal angle of incidence to the substrate. The laser intensity can be set between 400 and 7900 arbitrary units. As with the Voyager instrument, substrates with GLAD films were attached to a MALDI plate using conductive double-sided tape. Positive ion mode mass spectra

were acquired with the laser using the reflector, delayed extraction mode with an accelerating potential of 20 kV, an 80% grid potential and a delay time of 210 ns. Spectra were collected as an average of 400 laser pulses. Figure 5.2 shows plates mounted and spotted prior to mass spectrometry.

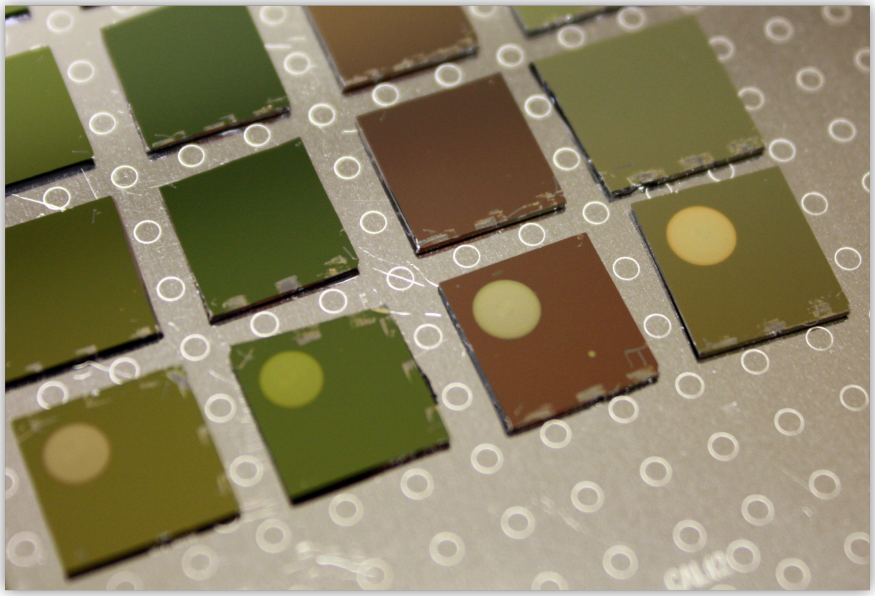

Figure 5.2: GLAD films with dried analyte spots mounted to a stainless steel MALDI plate with double-sided carbon tape prior to analysis. The films shown here are 500 nm thick Si vertical posts deposited at deposition angles of (L to R) 83°, 85°, 86°, and 87°.

5.3 Results and Discussion

5.3.1 Film Optimization

We first determined the material characteristics of Si GLAD films in terms of film density and porosity, by fabricating 500 nm thick films at various deposition angles

(1°, 70° and 85°), as seen in Fig. 5.3. The deposition angle determines the extent of self-shadowing that occurs, and consequently the film pore size and density [19,20,34]. From the SEM images, we estimate films deposited at 1° are composed of essentially solid structures and those prepared at 70° contain pores less than 5 nm in size. Films grown at 85° had pore sizes of tens of nanometers. Similar pore sizes have been reported for silicon films grown at these angles [198]. The densities of our films are estimated to be approximately 15-20% of bulk based on reported measurements of silicon and metal oxide GLAD films, using methods described elsewhere [58,199].

Our observations show that DIOS performance of the GLAD films was dependent on both film density and porosity. Figure 5.4 shows mass spectra obtained from various films for 5 pmol bradykinin fragment 1-5 and 120 pmol dopamine. Intense signals were observed from films deposited at 85°, but no analyte signal was observed from films deposited at 1° and 70° for up to 2 nmol of bradykinin fragment 1-5. Similar results were seen for 10 pmol [Val^5]angiotensin-I and 10 pmol angiotensin-II (data not shown). No peptide signal was detected from a bare silicon surface, demonstrating the importance of the porous film. The primary differences among the three Si GLAD films are the pore sizes, the pore distribution, and the overall film density. The results are consistent with observations regarding the critical role played by the overall porosity and pore sizes of porous silicon for UV-laser desorption/ionization [133–135,148,151,153,192]. The films grown at 85° have large enough pores (macropores)

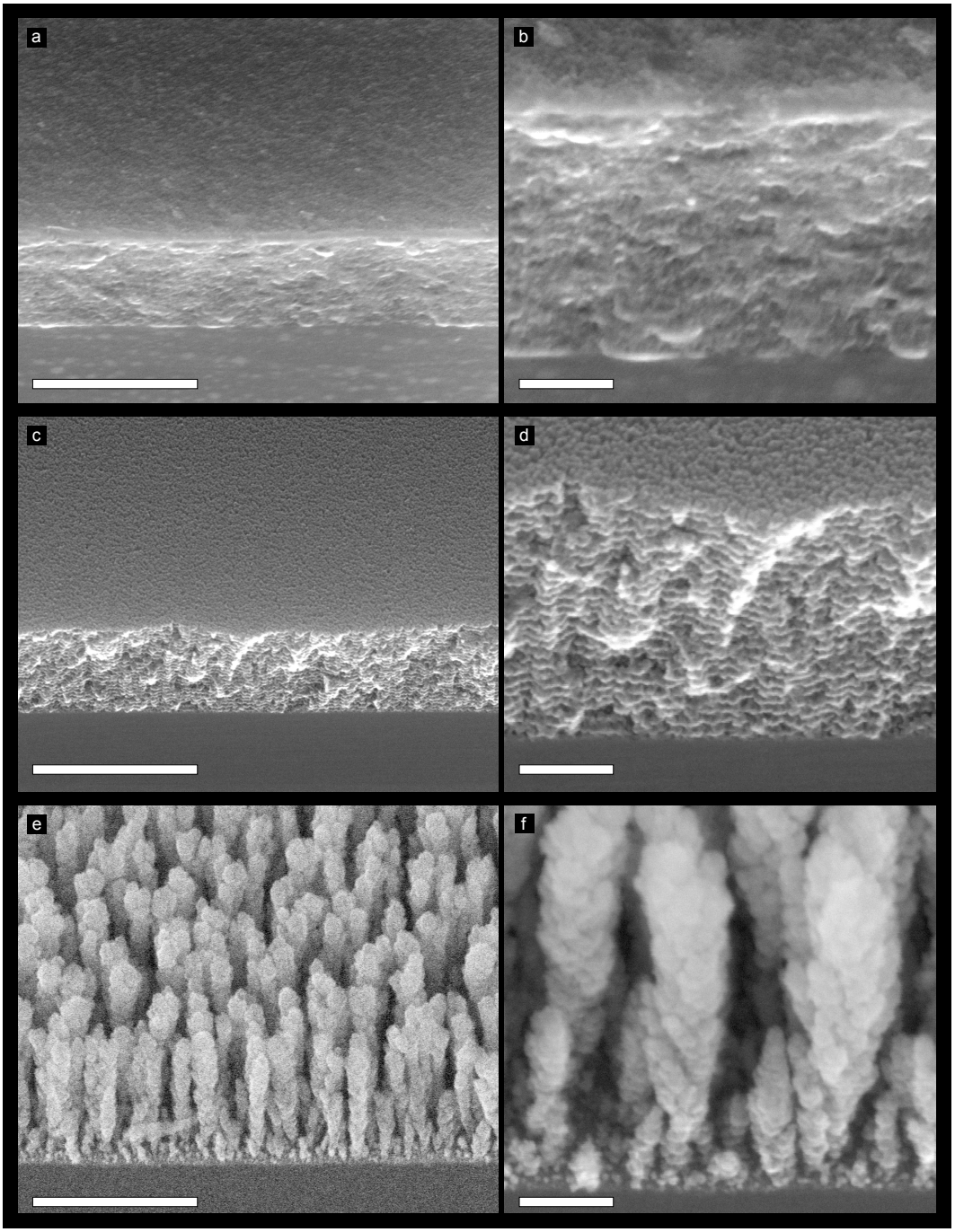

Figure 5.3: Oblique view scanning electron micrographs of 500 nm thick Si GLAD films grown for DIOS studies at 1° (top), 70° (middle) and 85° (bottom). The right column (b, d, f) shows a magnified view of the films shown in the left column (a, c, e). Scale bars indicate 500 nm (left) and 100 nm (right).

to provide the required platform to retain solvent and analyte molecules in order to allow efficient desorption/ionization. For subsequent studies, a deposition angle of 85° was used.

Previous studies have indicated that film thickness and structure height play a role in LDI performance [136–138, 140, 154, 155, 160, 169, 170, 175]. We evaluated a series of film thicknesses to determine if there is an optimal film thickness for our structures. The desorption/ionization response of verapamil (*m/z* 455.6), was measured on films deposited at 85° to thicknesses ranging from 100 nm to 1500 nm. Figure 5.5(a) shows the total ion counts obtained from these films for 10 pmol verapamil. With increasing film thickness, there was a strong increase in signal intensity up to 500 nm when the films were irradiated with the same laser fluence, followed by a near-plateau in signal intensity.

Figure 5.5(b) shows a plot of optical UV-absorption of the films as a function of film thickness. The result demonstrates that 90-95% of the light is not transmitted at a film thickness of 500 nm. We conclude that 500 nm films have enough material to absorb 90-95% of the UV light and convert the laser energy into sufficient thermal energy to efficiently desorb molecules. This observation is similar to that for electrochemically etched porous silicon [133–135, 148, 192, 200, 201], which commonly use pore depths of 250-700 nm, and for porous alumina thin films, which use ~600 nm films for optimal laser desorption/ionization performance [136].

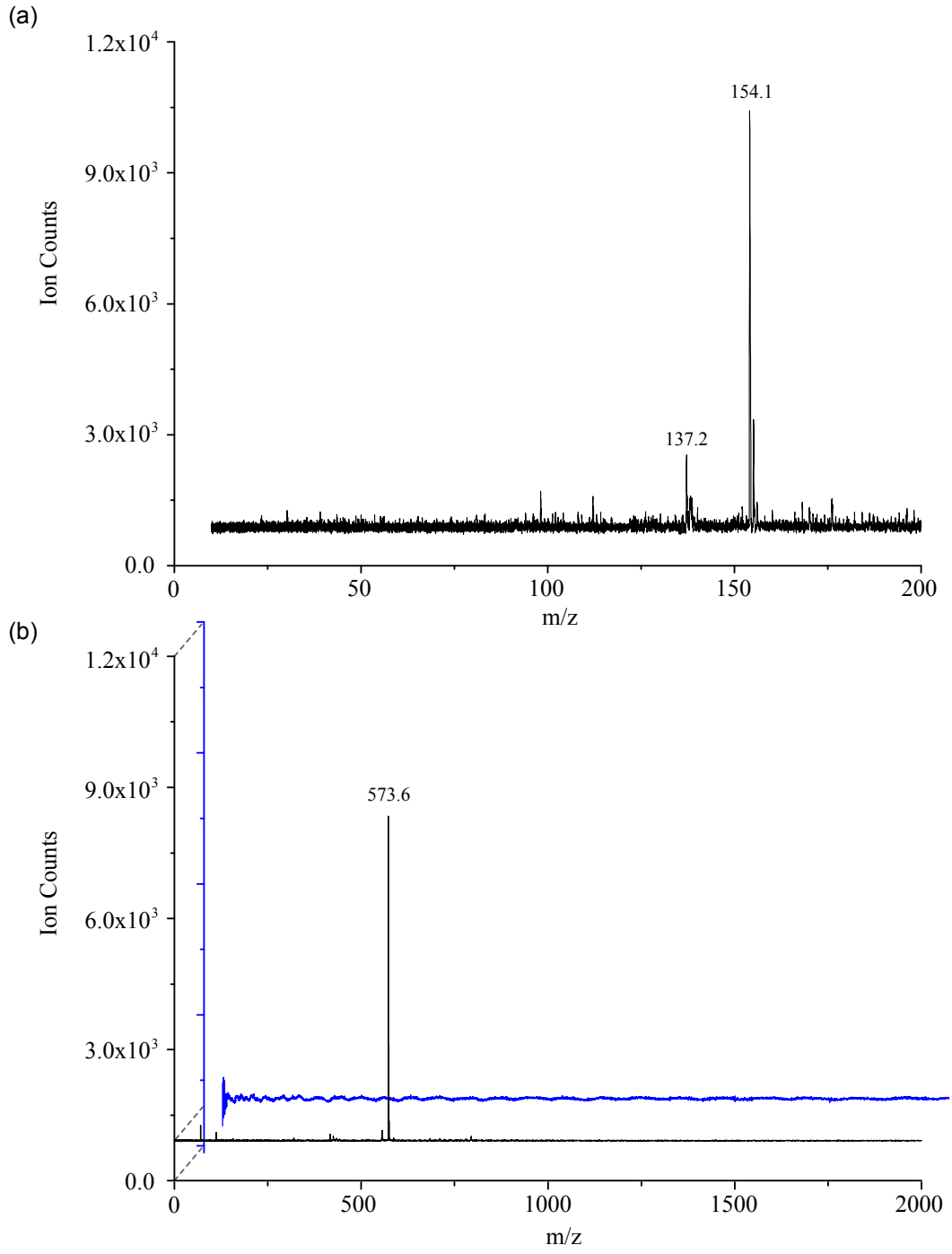

Figure 5.4: Desorption/ionization mass spectra of (a) 120 pmol dopamine and (Front, b) 5 pmol bradykinin fragment 1-5 using 500 nm Si GLAD films fabricated at 85°. (Offset blue line, b) Mass spectra of 2 nmol bradykinin using 500 nm Si GLAD film fabricated at 1° deposition angle. (Essentially the same result was obtained at 70° deposition angle (trace not shown) as at 1°.)

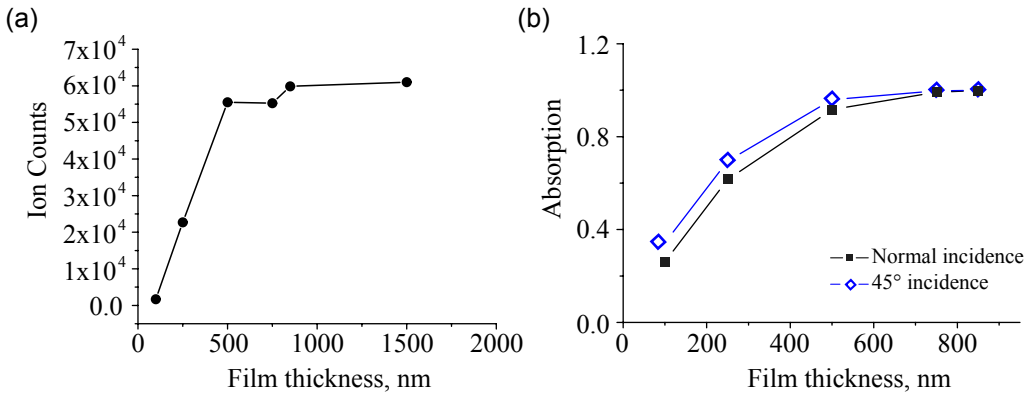

Figure 5.5: (a) Total ion counts of verapamil obtained from Si GLAD films of different thicknesses. 10 pmol was spotted on all the films and the same laser energy was used in all experiments. (b) UV absorption (1-transmission) of Si GLAD films at 337 nm wavelength as a function of film thickness. 500 nm Si films were deposited at 85° on fused- silica substrates for the absorption measurements.

5.3.2 Small Molecule Detection

DIOS provides a low background at low masses, making it particularly suited to investigation of small molecules that may be difficult to identify by MALDI due to matrix background peaks in the low molecular weight region. As a continuation of our initial study, dopamine, a naturally occurring neurotransmitter, produced a good quality spectrum containing the molecular ion at *m/z* 154.1 and its fragment at 137.2 *m/z* (Fig. 5.4(a)), likely originating from loss of the amine group [202]. The background noise and the fragmentation seen in Fig. 5.4 are similar to that reported for DIOS-MS of dopamine using etched porous silicon [203]. Figures 5.6(a) and 5.6(b) show negative ion mass spectra of 340 fmol flavin mononucleotide (FMN) metabolite using two different laser fluences. The $[M\text{-}H]^-$ signal of FMN at *m/z* 454

was dominant, and at lower laser fluence there was substantially less background chemical noise than at higher laser fluence. Higher laser fluence also gave FMN fragments at 375.5 *m/z* (loss of phosphate) and 436.4 *m/z* (loss of water). The sodium adduct of FMN was also detected at 478.1 *m/z*. The high-quality signal to background performance observed at both laser fluences demonstrates the suitability of Si GLAD films for the analysis of small molecules. The mass spectrum of picomole quantities of a mixture of bradykinin fragment 1-5, verapamil and [Val^5]angiotensin-I using 500 nm Si GLAD films in DIOS-MS gave far superior signal-to-noise performance than MALDI using an CHCA matrix (see Fig. 5.7).

To further characterize the effect of laser fluence on the performance of Si GLAD films, we evaluated the role of laser power on desorption/ionization of bradykinin fragment 1-5. Figure 5.8 shows the ion counts and S/N ratios as a function of laser power. (For the Voyager spectrometer available for this study, the absolute laser power values are not known.) At lower laser power, the bradykinin fragment 1-5 ion counts increased with increasing laser power. However, the S/N ratio reached a plateau, due to an increase in background signal. Additionally, for analytes which tend to fragment, more fragmentation was observed at higher laser power, as seen in Fig. 5.6. Figure 5.8 demonstrates that a laser power range between 2400 and 2500 (arbitrary units) on the Voyager gave optimal performance on Si GLAD films.

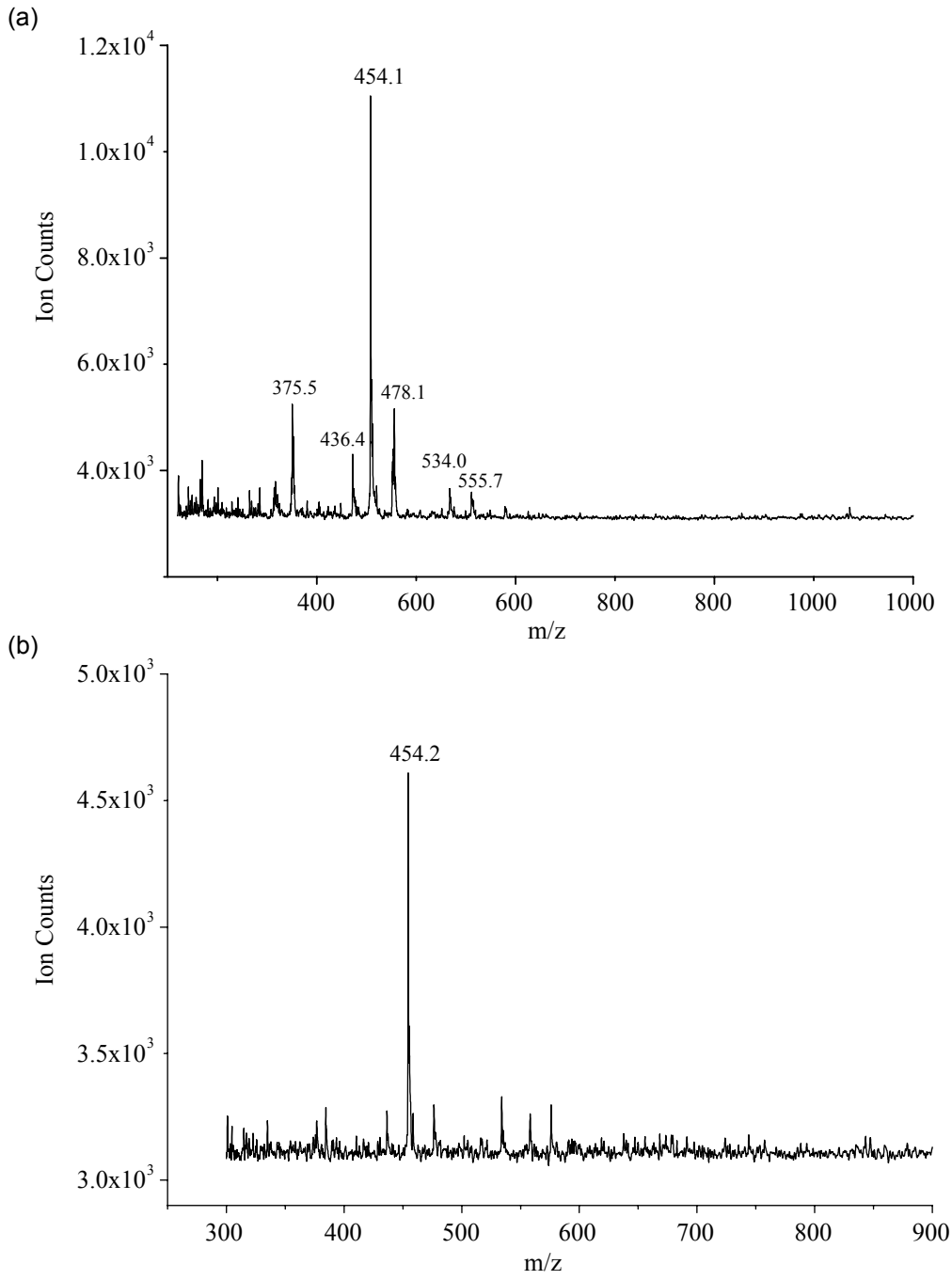

Figure 5.6: Negative ion ($[M\text{-}H]^-$ = 454.1) mass spectrum of 340 fmol flavin mononucleotide on a 500 nm thick Si GLAD film using a laser power of (a) 2450 a.u. and (b) 2400 a.u. Peaks at 534 *m/z* and 555 *m/z* are unknown.

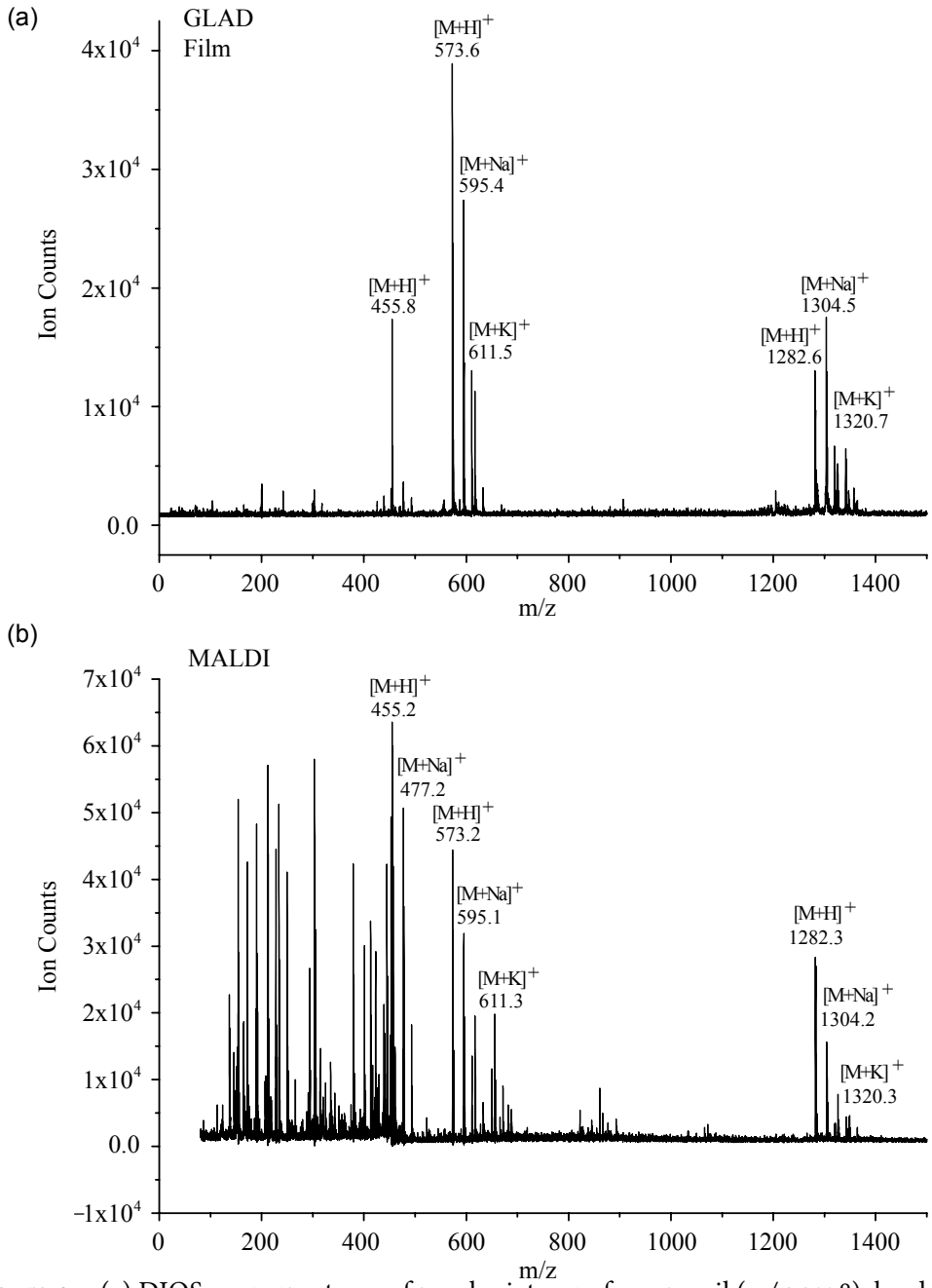

Figure 5.7: (a) DIOS-mass spectrum of pmol mixtures of verapamil (*m/z* 455.8), bradykinin fragment 1-5 (*m/z* 573.6) and angiotensin II (*m/z* 1282.6) using a 500 nm Si GLAD film at a laser intensity of 2400 a.u. and (b) MALDI-mass spectrum of the same mixture using a CHCA matrix at a laser intensity of 2950 a.u. In the Voyager instrument, a laser intensity of 2800 a.u. was required to see a signal with the CHCA matrix.. Mass differences of related peaks between the two spectra are due to omission of mass calibration, and are not considered significant for the purpose of comparing presence or absence of background signal.

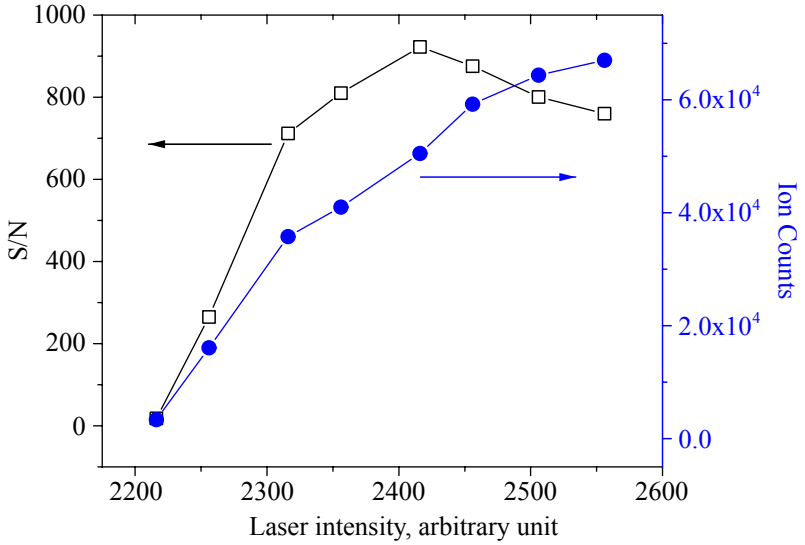

Figure 5.8: Plot of signal-to-noise ratio (open squares) and ion counts (solid circles) of 3 pmol bradykinin fragment 1-5 as a function of laser intensity using 500 nm Si GLAD films.

5.3.3 Detection Limits

The detection limit of 500 nm thick Si GLAD films was evaluated using an optimized laser power. Well-defined mass spectra were recorded for doses of 6.5 fmol of des-arg^9-bradykinin (S/N ratio = 742.8), 10 fmol ACTH (18-39) (S/N ratio = 411.9), 13 fmol angiotensin-I (S/N ratio = 5163.3) and 200 fmol verapamil (S/N ratio = 1924). Representative data is shown in Fig. 5.9. The calculated limits of detection (S/N ratio = 10) of our films are in the sub-fmol level (87 amol for des-arg^9-bradykinin, 243 amol for ACTH fragment, 25 amol for angiotensin-I and 1.0 fmol for verapamil). These limits of detection are as good as or better than reported values for DIOS-MS of small peptides using electrochemically etched porous silicon (700 amol and 4

pmol for des-arg^9-bradykinin) [133, 147], porous SiO_2 (50 fmol for the tripeptide LGG) [165], column/void-network-deposited silicon films (50 fmol for [des-pro^3-ala 2,6]-bradykinin) [153], porous alumina (4.3 pmol for bradykinin) [136], SiNWs (500 amol for des-arg^9-bradykinin and 5 fmol for verapamil) [155,160], Pt nanoflowers (700 amol for angiotensin-I) [171] and silicon nanoparticles (33 fmol for verapamil) [204]. While some of these differences may arise from differences in mass spectrometer performance, the results demonstrate the competitive performance of Si GLAD films for DIOS. Siuzdak's group has reported yoctomole detection limits for small molecules by functionalizing the surface of porous silicon [189, 191]. GLAD films are readily functionalized [205, 206] so their good performance compared to porous silicon surfaces made using other techniques suggests their detection limits could be further improved by similar surface functionalization.

5.3.4 Signal Reproducibility

To examine the shot-to-shot reproducibility of mass signals in DIOS-MS with the Si GLAD films, we collected intensities from single shot measurements of 5 pmol verapamil at different locations on the same target (Fig. 5.10). The signal peaks from verapamil were reproducible with an average signal intensity of 70%±19% (n=7, 100%=max signal observed). We also examined the spot-to-spot reproducibility of signals in our films by measuring the signal intensity (100 shots/spectrum) from

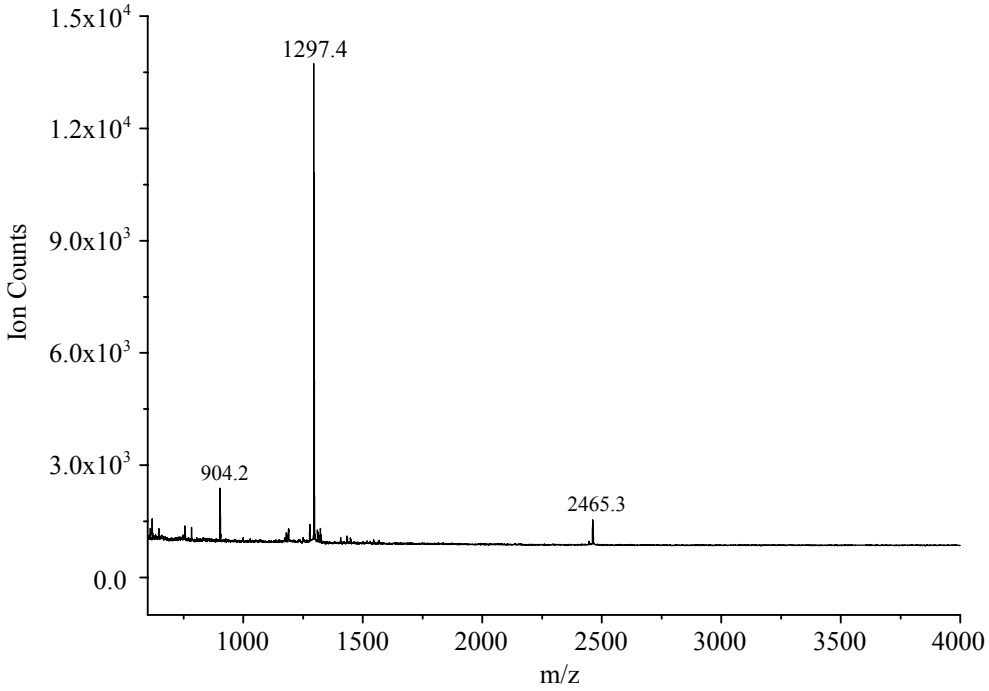

Figure 5.9: Mass spectrum of a mixture of 6.5 fmol des-arg^9- bradykinin (*m/z* 904.2), 13 fmol angiotensin-I (*m/z* 1297.4) and 10 fmol ACTH fragment (18-39) (*m/z* 2465.3) on a 500 nm thick Si GLAD film.

21 different targets. The average signal intensity was 79% with a relative standard deviation (RSD) of 13% (Fig. 5.10). There was no indication of either sweet spots or mute spots typically seen in MALDI [194], presumably due to the uniform distribution of sample on the nanostructured films.

5.3.5 Film Stability

The Si GLAD films, like other porous DIOS surfaces, have very high surface areas [58] and are prone to adsorbing contaminants from the air when stored at ambient conditions. Extensive reports have shown that the S/N ratio for the analysis of molecules

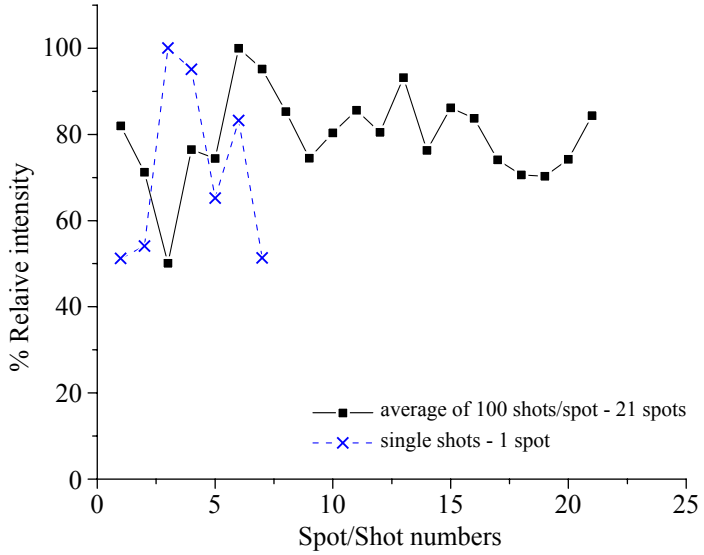

Figure 5.10: Plots of relative peak intensity (maximum intensity = 100%) of 5 pmol bradykinin fragment 1-5 obtained from single shot measurement (crosses) on a single spot and average of 100 shots/spot from 21 different sample spots (solid rectangles) using Si GLAD films.

<700 *m/z* using aged (a few days of dry storage at ambient conditions) porous silicon is compromised by the appearance of 'background' ions [133, 134, 148, 150, 151, 192]. We have observed similar low mass noise (100-300 *m/z*) when GLAD films were used after 3 months of storage at ambient conditions (Fig. 5.11(a)). The origin of these background ions is thought to be adsorbed hydrocarbons from air or outgassing of storage containers [133, 148, 150, 151, 192]. HF etching prior to use, or storage of freshly prepared porous silicon in ethanol or propanol, has been recommended to minimize these low molecular weight background ions and restore the DIOS performance [133, 134, 148, 150, 151, 192]. These steps, however, are detrimental, since further etching of the already etched porous Si structure alters the film morphology,

while storing porous Si in organic solvent adds packaging complexity to a commercial product. Instead, we employed a UV ozone (UV-O) cleaning method to remove adsorbed hydrocarbons from Si GLAD films, a procedure commonly used to clean many substrates [207]. Cleaning the Si GLAD films using a UV-O-cleaner for 15 min prior to DIOS experiments significantly reduced these low mass background ions (Fig. 5.11(b)). The low intensity peaks observed before and after cleaning have different masses, indicating they do not derive from the sample. UV-O treatment is known to cause oxidation of a surface layer in silicon to form SiO_2 [208]. However, pure silicon will oxidize within minutes of exposure to air to form a surface oxide layer, SiO_x, so that further treatment by UV-O cleaning will not greatly change the actual exposed surface of the GLAD Si films. XPS measurements confirm that aged Si GLAD films had atomic ratios of 41% Si, 52% O and 7% C at the surface. We note that the carbon content of the films had increased by about 6% during storage. Thus the Si GLAD films are already oxidized before any further cleaning treatment, and will already bear silanol and related silicate functionalities. UV-O treatment should not greatly change the surface silicate chemistry, beyond removal of surface contaminants. Shelf life tests, under ambient conditions, were performed over a 3-month period. After UV-O cleaning, the performance of GLAD films was essentially the same as freshly prepared surfaces. The aged GLAD films show an advantage compared to porous silicon. Kruse *et al.* [148] observed a significant analyte signal intensity deterioration

for porous Si following 6 days of dry storage at ambient condition, compared to a porous Si target soaked in methanol for 6 days. In contrast, the signal intensity of analyte on the GLAD films remained essentially the same (within 10%) whether or not the film was treated with UV-O prior to experiment; only the background signal was changed by cleaning (Fig. 5.11).

5.3.6 Highly Oblique-deposited Vertical and Slanted Posts

Our initial study focused on three regimes of obliquely-deposited films: a non-porous, dense film deposited at a normal angle (1° here), very high surface area, dense films with small pores deposited at 60° to 70° (70° here), and very porous, high surface area films deposited at 'glancing angles' of 80° to 90° (85° here). Given the superior performance of the latter films, the performance of films grown at glancing angles was further investigated.

Mass spectra of verapamil (32.6 fmol) and bradykinin fragment 1-5 (240 fmol) were collected by LDI from Si vertical post films deposited at angles of 79°, 81°, 83° and 85° (Fig. 5.12(a)), and at angles of 85°, 86° and 87° (Fig. 5.12(b)), at a laser power of 2650. The LDI performance noticeably improved with increasing deposition angle, with a three- to four-fold increase in signal between the films at 85° and 87°, and no observed signal for the films at 79° and 81° (at identical laser intensities).

The increasing signal count with deposition angle indicates a much higher effi-

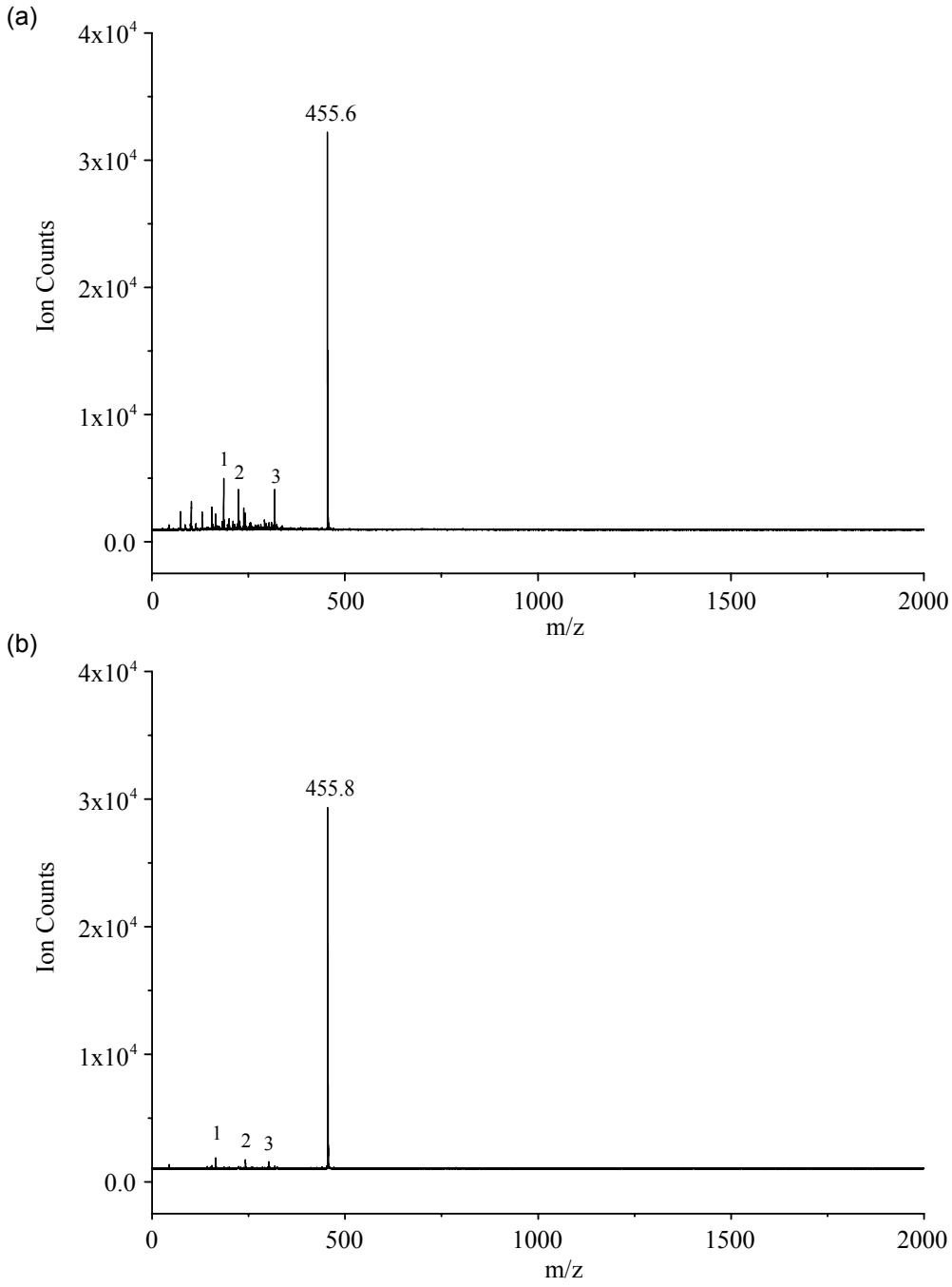

Figure 5.11: Mass spectrum of 4 pmol verapamil obtained from 500 nm film stored for 3 months at ambient conditions (a) without UV-O treatment and (b) after 15 min UV-O treatment. Background peaks marked in (a) are at m/z of 186.0 (1), 223.9 (2) and 317.8 (3) and background peaks marked in (b) are at m/z of (1) 165.1, (2) 241.9 and (3) 302.8.

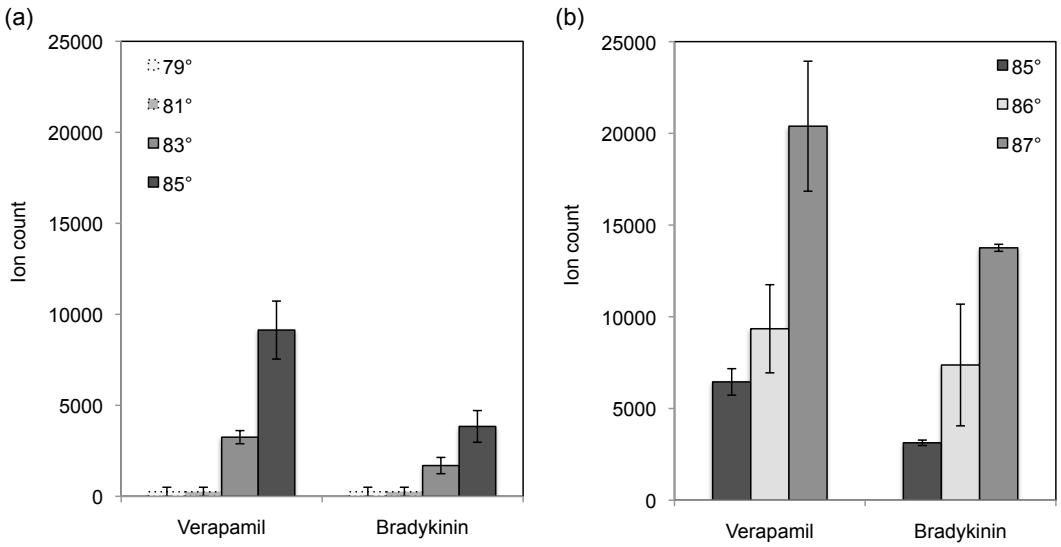

Figure 5.12: Ion counts of verapamil (32.6 fmol) and bradykinin fragment 1-5 (240 fmol) from LDI on Si vertical post films deposited at 79°, 81°, 83°, 85°, 86° and 87° in two separate experiments, (a) and (b), under identical conditions. Laser power was set at 2650. Error bars indicate 1 SD from the mean, n ≥ 3.

ciency for more obliquely-deposited films. The mechanism for this improved performance is not yet understood, but film porosity likely has an influence on LDI performance; pore-size dependence of DIOS and other SALDI substrates has been noted by numerous groups [136, 137, 148, 150, 154, 164]. We also qualitatively observed increased scattering of light as the deposition angle approached 87°, evident by a less reflective film surface. This scattering from a post redirects light towards adjacent posts rather than reflection away from the substrate, which could result in increased absorption of light and subsequent desorption of analytes.

Investigation of the film morphology provides insight into other possible factors (Figure 5.13). The power law scaling associated with GLAD film growth [13] produces

vertical posts that widen as they grow upwards from the substrate. This top-heavy, cone-like morphology produces columns that are susceptible to capillary forces from the receding meniscus of a drying droplet applied to the film surface [123, 125]. These forces are evident in the resulting 'clumping' of wetted posts, seen after being dried in the right-hand column of Figure 5.13. As the deposition angle increases, power-law scaling becomes more pronounced (the posts deposited at higher α widen faster in a given amount of vertical growth), and posts are spaced further apart. The net effect is more pronounced clumping, especially evident at 87° where the posts are pulled down and sideways, and lie almost flat against the substrate.

Clumping has two effects. The first is that pore size becomes more difficult to define, and further study is necessary to determine what influence, if any, the pore structures created by the clumping process have on the desorption and ionization processes. The second is a reorientation of the posts relative to the substrate, and also to the incoming laser beam. Walker *et al.* showed that polarized light incident at 45° coupled into posts with sub-μm diameters (50-600 nm) when the electric field was parallel to the posts (i.e. in line with, not perpendicular to, the posts), and that this coupling was essential to the LDI process in such structures. Okuno *et al.* similarly showed that reactive ion etched silicon 'lines' 150 nm wide and 300 nm high will provide better performance when oriented parallel to the electric field [135]; while the authors attribute the difference to reflections off the sub-wavelength front walls

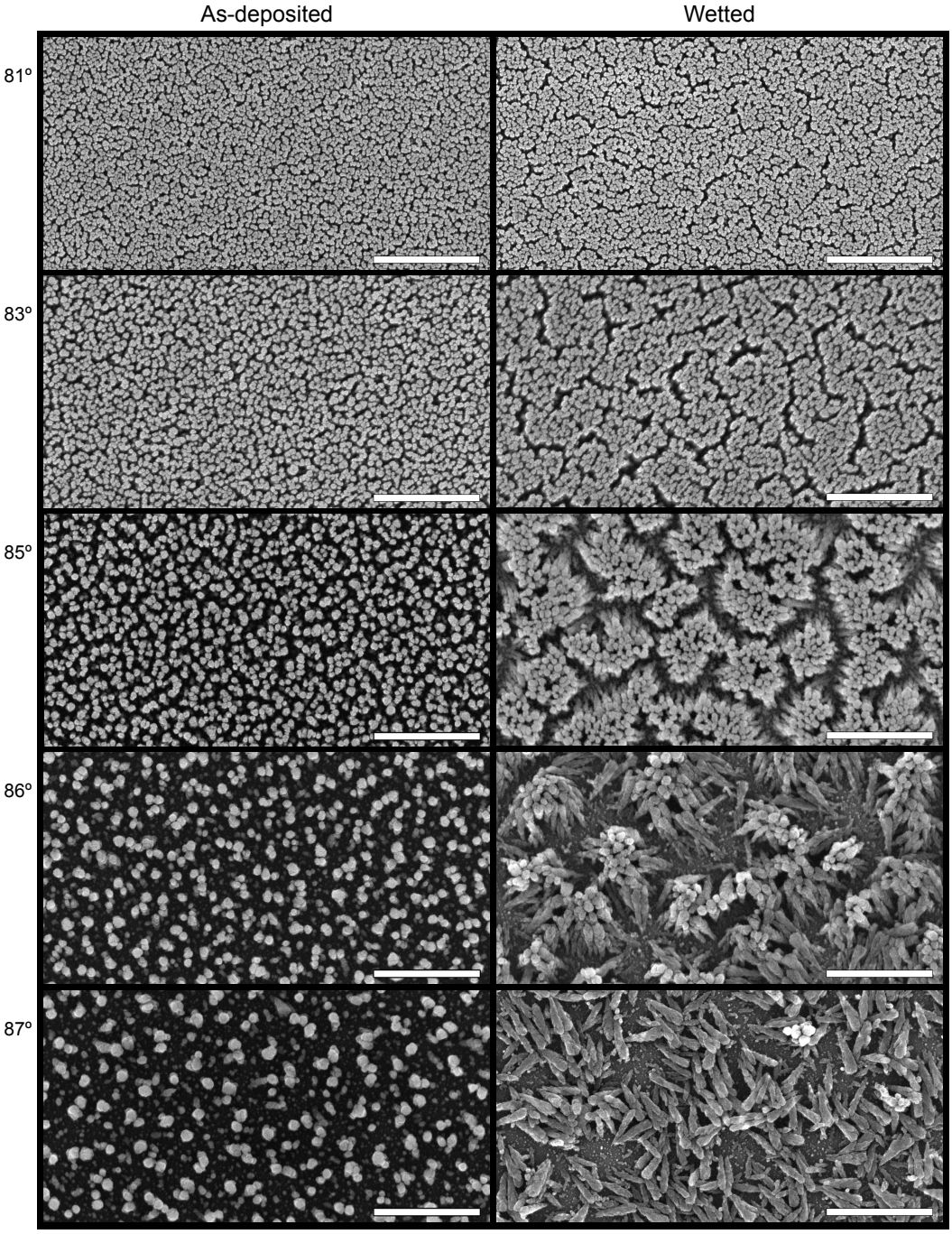

Figure 5.13: Top-view SEMs of Si vertical post films, deposited at the indicated angles, as-deposited (left column) and after being wetted with a 0.1%TFA solution droplet and allowed to dry (right column). Scale bars indicate 1 μm.

of the lines, a coupling effect similar to Walker *et al.* is a more likely explanation.

To study the effect of post orientation further, and to verify its role in the overall mechanism of SALDI on GLAD films, we tested LDI on slanted Si posts, shown in Figure 5.14. Slanted posts are all aligned to the same axis, are tilted relative to the substrate normal, and are pulled further towards the substrate once wetted and dried; thus they should be more susceptible to effects that arise due to orientation of the posts with the laser beam electric field. The signal strength and signal-to-noise ratio for des-arg^9-bradykinin desorbed from posts deposited at 78.5°, 83.5° and 85.5° using the ABS-MS is shown Fig. 5.15(a). As with vertical posts, the more widely-spaced, larger diameter posts grown at higher deposition angles produced a noticeably stronger signal accompanied by improved signal-to-noise ratios. The impact of coupling light into the posts is apparent when comparing the laser power threshold for acquiring a des-arg^9-bradykinin signal (Fig. 5.15(b)). The slanted posts required less energy for desorption to occur. It is reasonable to conclude that this is a result of light coupling into the aligned slanted posts, given that the major difference between the two structures (vertical and slanted post) is the alignment of the slanted posts with the electrical field.

Further evidence for the coupling effect was given by measuring the desorption of verapamil and bradykinin fragment 1-5 from a vertical post and a slanted post film, using the Voyager MS. The slanted post film was oriented in three directions relative

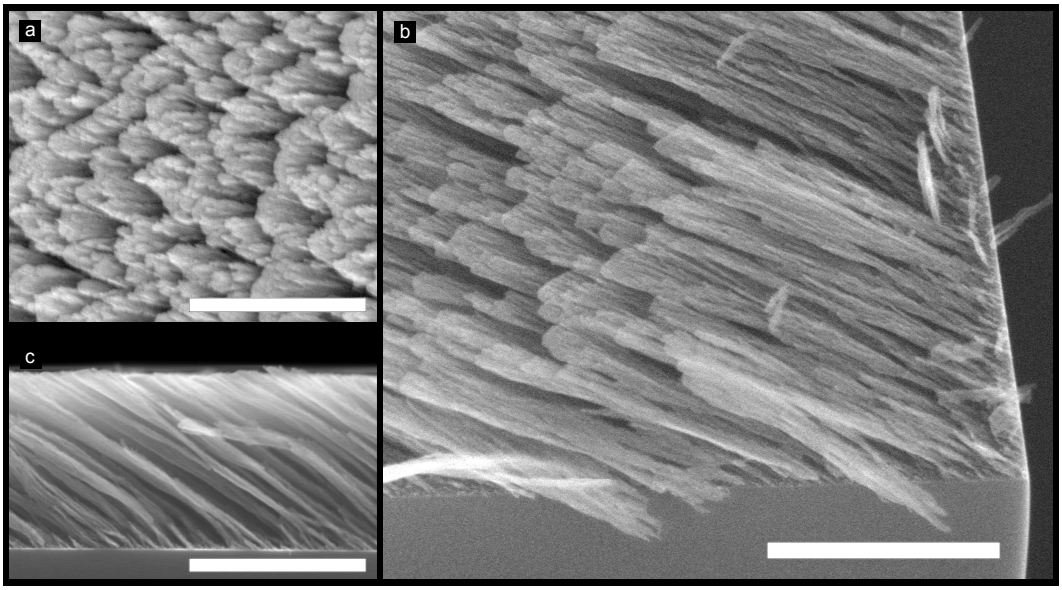

Figure 5.14: Top (a), oblique (b) and side (c) views of an Si slanted post film, grown at α = 85°. Scale bars indicate 500 nm.

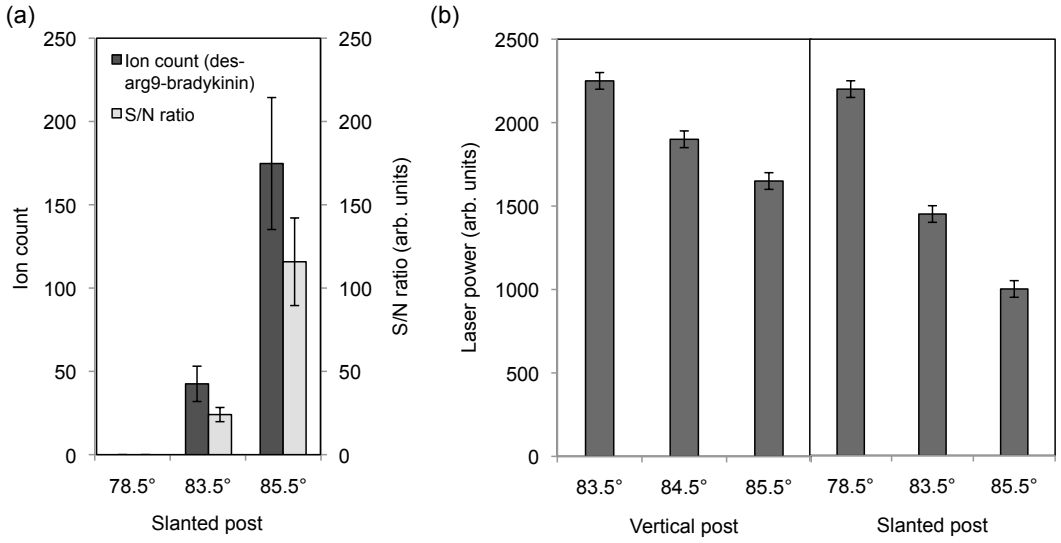

Figure 5.15: LDI response of slanted post Si GLAD films. (a) Ion counts and signal-to-noise ratio of des-arg^9-bradykinin (500 fmol) desorbed from slanted posts grown at 78.5°, 83.5° and 85.5°. (b) Minimum laser power required to acquire an ion count greater than 20 for the $[M+H]^+$ peak of des-arg^9-bradykinin (500 fmol) desorbed from vertical and slanted posts deposited at the indicated angles.

to the incoming laser beam, which arrives at the plate at an angle of 45° relative to the substrate normal (Fig. 5.16(b): B,C,D). The first orientation, where the beam is parallel to and points 'into' the posts, had the same signal strength as a vertical post film grown at the same deposition angle but the weakest signal of the three orientations (Fig. 5.16(a)). The second orientation, with the beam perpendicular to the posts, produced a stronger signal than the vertical post film. A very strong signal was produced by the last orientation, where the incoming beam is almost normal to the posts. Each orientation, from the first to the third, provides a progressively larger material cross-section to the electric field, which is perpendicular to the beam (and for unpolarized light in random orientation in that perpendicular plane). This transition, combined with the increased alignment between the posts and field, is consistent with light coupling into the posts. The third orientation provides the best alignment between the posts and the plane of the laser beam electric field. The above results strongly suggest that coupling of light into the GLAD posts has a strong positive effect on LDI performance and is a critical component of the desorption mechanism.

5.3.7 Insulating Subtrates

It is generally accepted that the thermal and electrical properties of the SALDI surface and substrate play a role in LDI performance, but it is not yet clearly understood how and when these properties come into play [135, 136, 138, 140, 148, 149, 156]. There

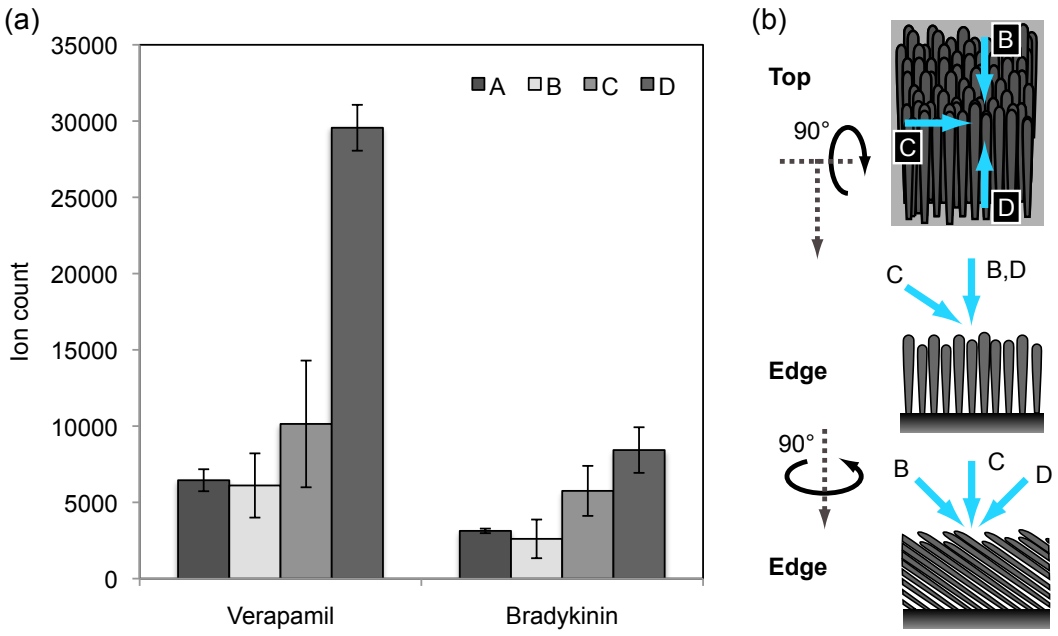

Figure 5.16: (a) Ion counts of verapamil (32.6 fmol) and bradykinin fragment 1-5 (240 fmol) on vertical posts (A) and slanted posts aligned parallel and pointing towards (B), perpendicular to (C) and parallel and pointing away from (D) the incoming laser beam, as shown in (b), where the blue arrows indicate the incoming laser beam (see text for details). Both films were grown at $\alpha = 85°$. All measurements were made at laser power 2650.

have been reports of SALDI from insulating substrates, such as a nanoporous SiO_2 scaffold [164], oxidized porous Si [165], SiO_2 gel [150] and TiO_x nanotubes prepared from sol gel [166]. However, other groups have reported poor to no response from insulating materials, including porous Al_2O_3 (anoded aluminum) [135, 136], SiO_2 (thermal oxide) [140], polymer micropillars coated with Al_2O_3 or TiO_2 by atomic layer deposition (ALD) or with SiN by plasma-enhanced chemical vapor deposition (PECVD) [140], and oxidized crystalline Si nanowires [160].

While insulating materials by themselves appear to work only under select con-

ditions, Okuno *et al.* [135] and Nayak *et al.* [136] observed strong LDI perfomance by coating LDI-inactive porous Al_2O_3 with 30–120 nm sputtered Au. Jokinen *et al.* [140] found that a 40-80 nm coating of PECVD-deposited amorphous Si over planar insulating polymer and thermal oxide substrates produced a strong signal, whereas the same coating on an uncoated Si wafer produced no signal. An even stronger signal was obtained by coating non-planar, nanostructured polymer surfaces with the same Si layer. These results suggest that an insulating layer below the SALDI layer can enhance SALDI performance, possibly as a result of greater localized heating due to the thermal barrier formed by the insulating layer.

We performed a preliminary investigation into the effects of substrate insulation on GLAD-LDI. Verapamil, bradykinin, angiotensin, and ACTH (18-39) were desorbed from 500 nm thick Si vertical posts (α = 85°) deposited onto three different substrates (Fig. 5.17): an uncoated Si wafer, an Si wafer with a 600 nm solid layer of SiO_2 deposited at 1°, and an Si wafer with a 600 nm vertical post SiO_2 GLAD film deposited at 85°. The porous SiO_2 substrate provided noticeably poorer performance compared to the other two substrates (Fig. 5.18(a)). The difference between the solid SiO_2 and crystalline Si substrates was not significant. A separate measurement confirmed the poorer performance of silicon deposited on the porous substrate compared to the solid substrate: verapamil and bradykinin were both desorbed less efficiently from silicon on a porous SiO_2 layer than the solid SiO_2 layer (Fig. 5.18(b)).

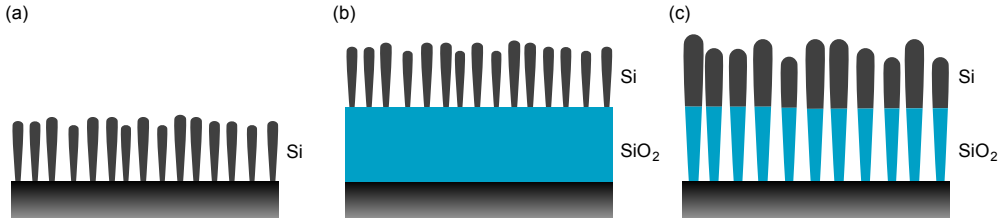

Figure 5.17: Three film configurations used to investigate the effect of an insulating substrate: 500 nm Si GLAD film (α = 85°) deposited on top of (a) bare Si wafer, (b) 600 nm solid evaporated SiO_2 layer, (c) 600 nm SiO_2 GLAD film (α = 85°).

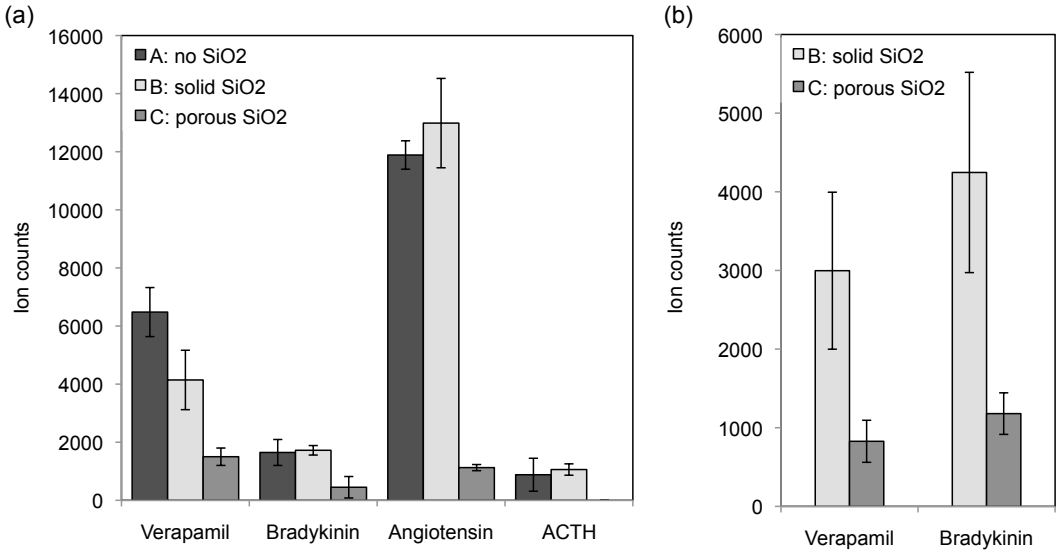

Figure 5.18: (a) Desorption of verapamil (324 fmol), bradykinin (1 pmol), angiontensin (1 pmol), and ACTH (18-39) (1 pmol) from the three films, A, B and C as described in Fig. 5.17. Laser power was set at 2855. (b) Desorption of verapamil (65.8 fmol) and bradykinin fragment 1-5 (2.82 pmol) in a separate experiment from the two films with insulating substrates, B and C, used in (a). Laser power was set at 2415.

The behaviour of our films was anomalous in light of the results in the literature cited above. The solid oxide layer made little difference to the LDI performance of the Si structures. A possible explanation for this lies in the thermal conductivity of amorphous silicon, which at 1.7 $W\,m^{-1}\,K^{-1}$ [209] is not much higher than silicon dioxide (1.38 $W\,m^{-1}\,K^{-1}$) [210] and two orders of magnitude lower than crystalline silicon (124 $W\,m^{-1}\,K^{-1}$) [210]. The amorphous Si layer reported by Jokinen *et al.* may have been thin enough that heat loss by conduction to the substrate beneath the silicon was high enough to play a role in the desorption process; consequently an insulating SiO_2 or polymer layer resulted in improved desorption. The GLAD vertical posts, at 500 nm, have a significantly longer thermal path; as a result, reduced thermal conductivity at the substrate would have less effect due to lower heat flow at the interface within the desorption time frame. This effect could also have played a role in the saturation in film performance as the thickness increased, discussed in section 5.3.1. The light absorption depth combined with heat confinement in the post limits performance improvements when the posts are grown taller.

The poor performance of the porous SiO_2 substrate is not yet understood. The effect on the film morphology of depositing the Si posts on top of SiO_2 posts instead of a planar substrate can not be discounted. The resulting film will have a morphology more similar to an Si film grown to a height of 1100 nm than 500 nm, and as a result the Si layers are not directly comparable. Figure 5.19 shows top view SEMs of three

films (no SiO_2 layer, solid SiO_2 layer and porous SiO_2 layer) before and after wetting, and edge views of as-deposited films. The differences in film morphology are clear: the 500 nm Si layers on top of solid substrates (Si and SiO_2) exhibit similar morphology before and after clumping, whereas the third film has broadened more, as would be expected of a thicker film, resulting in larger pores in both the as-deposited and clumped states.

This change in film morphology is likely *not* responsible for the decreased performance, however, as the difference in moving from the solid to the porous SiO_2 layer is akin to that of moving to higher deposition angles (Fig. 5.13), which in that case led to improved performance. In comparison, based on morphology alone, one would also expect improved performance from the porous insulating layer. The change in thickness is also likely not reponsible for the decreased performance, given that 1.5 μm thick Si films did not have decreased performance relative to thinner films (Fig. 5.5). The edge-view SEMs confirm that the post structure was not interrupted by the change in material from Si to SiO_2, confirming that this is a valid comparison. Given our current knowledge of LDI performance on GLAD films, in addition to results presented in the literature, the 600 nm SiO_2 / 500 nm Si vertical post heterostructure should have given similar, if not superior, performance to the other two films discussed. One possible factor may have been the hydrophilicity of the SiO_2 layer that could lead to increased spreading of the applied analyte droplet through

the underlying porous layer, effectively decreasing the analyte concentration at the surface during LDI. Elucidation of the mechanism responsible for the decreased performance would aid in understanding all the factors necessary for LDI on GLAD and lead to improved device design.

5.4 Concluding Remarks

This study has demonstrated the feasibility of using silicon nanostructured films fabricated by the GLAD technique for matrix-free detection of small molecules by laser desorption/ionization mass spectrometry. The morphology of these films consists of nanometer-sized vertical or slanted posts with highly controlled porosity, thickness and pore sizes.

We observed a correlation between film thickness, film porosity, pore size and desorption/ionization MS efficiency. GLAD films showed excellent sensitivity (amol levels) for small peptides and drugs. Unlike conventional MALDI, the Si GLAD films showed no sweet-spot and mute spot problems. After 3 months of storage at ambient conditions, UV-ozone cleaned Si GLAD films were readily used for analysis of small molecules without detrimental effects from absorbed contaminants. This simple cleaning step is an advantage compared to the methanol and propanol procedures frequently used with porous silicon. Depositing Si GLAD films on a solid insulating SiO_2 substrate had an insignificant effect on LDI efficiency, while a porous SiO_2

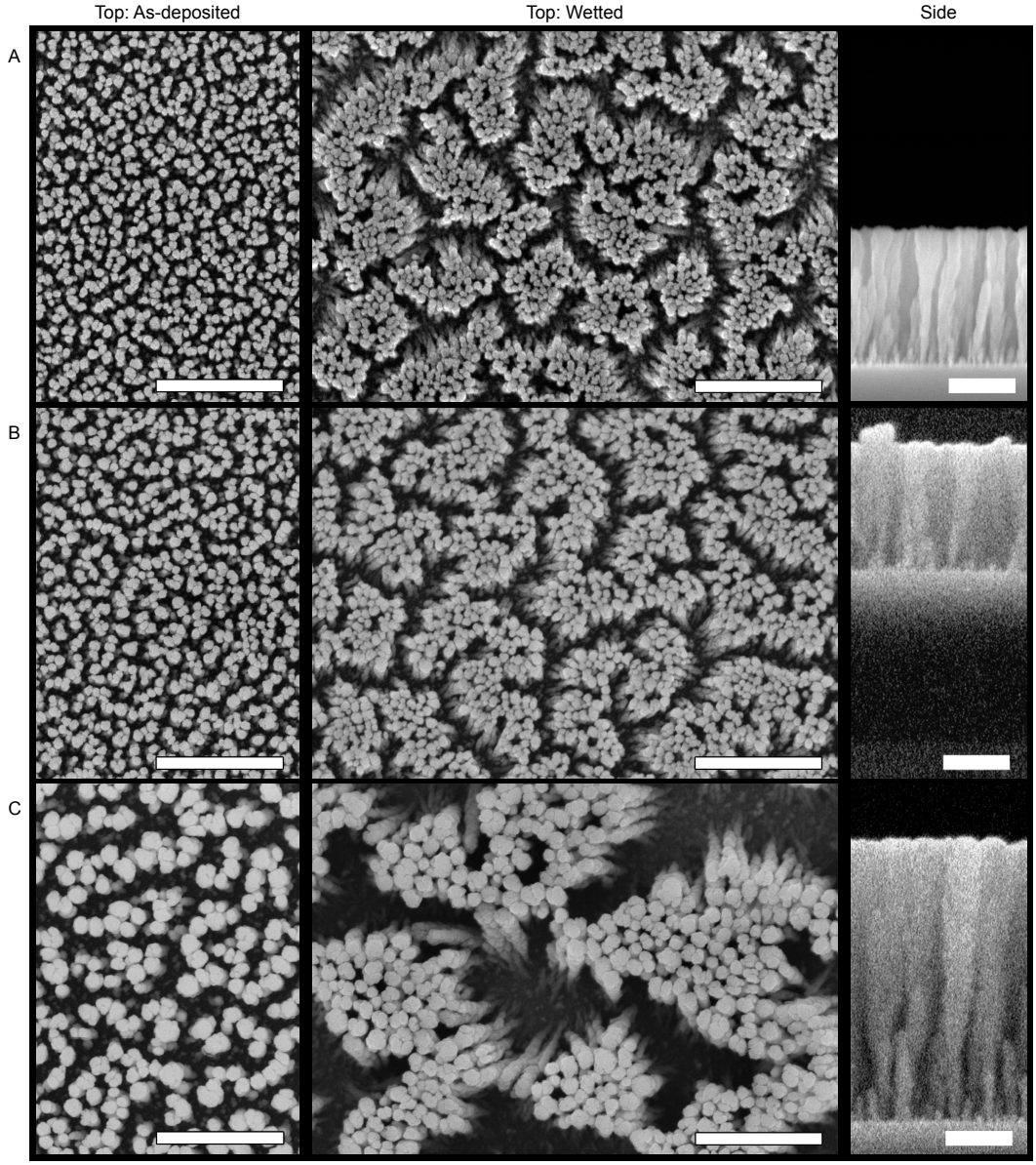

Figure 5.19: Top and side view SEMs of a 500 nm Si vertical post layer deposited on top of (A) a bare Si wafer, (B) a 600 nm solid SiO_2 layer and (C) 600 nm SiO_2 vertical posts, used to study the effect of insulating substrates. Films are shown as-deposited (top view in left column, side view in right column) and after being wetted with a 0.1% TFA solution droplet and allowed to dry (middle column). All porous films grown at $\alpha = 85°$. Scale bars indicate 1 μm in the top views (left and middle columns) and 250 nm in the side views (right column).

substrate decreased the efficiency.

The advantages of GLAD include the ability to produce large surface area silicon films with controlled pore size and porosity in a one-step deposition process at potentially low cost. Moreover, the vacuum preparation of GLAD films avoids the contamination issues that are involved in etching and exposure to wet solutions. The ability to deposit a wide range of materials and structures, with varying optical and thermal properties, by the GLAD technique may allow for the optimization of these parameters for even more efficient desorption/ionization. A simple change in morphology, from vertical posts to slanted posts, showed improved LDI performance and encourages further optimization. The GLAD technique is simple yet reproducible and represents a new approach to controllable fabrication of efficient DIOS targets.

CONCLUSION 6

6.1 Concluding Remarks

The demand for new technologies in bioseparations remains strong, fueled by our increasing knowledge of human physiology, and the demand for yet more knowledge. There has also been a marked shift over the past few decades from knowledge acquisition to knowledge application, where medical diagnostics and treatments centered on separation-based information have seen increasing importance. This is one of many areas that fuels research in biomolecular separations technology. The work presented here investigated the use of porous nanostructured thin films deposited with the glancing angle deposition (GLAD) technique in molecular separations.

Ultrathin-layer chromatography separation of a dye mixture on GLAD stationary phases proved that such films could be used as chromatographic media. More significantly, anisotropic structures were used for the first time in a planar separation, and we showed that the morphology of such films had a direct impact on the separations, with the flow front decoupled from the separation direction. Continuing work by our group has shown that the performance of unoptimized GLAD plates is comparable

to existing techniques. This encourages further work, especially when considering more advanced techniques that can be used to shape and mold the nanostructures for optimized and novel UTLC separation applications.

GLAD structures were subsequently encapsulated in microchannels, using a sacrificial resist technique developed specifically for this purpose. The ability to integrate a wide variety of structures and materials in microfluidic channels was demonstrated. This allows one to fully capitalize on the advantages offered by the GLAD process in fabricating nanostructures when applied to microfluidics. Electrophoretic separation of DNA in a fractionator device verified that the uniformity and integrity of GLAD structures was maintained in the microchannels, and proved that GLAD-based devices could be effectively integrated in working microfluidic devices.

While not a separation technique in the strictest sense, laser desorption/ionization mass spectrometry is akin to biomolecular separations in that it can be used to accurately identify the compounds in a mixture. Mass spectrometry with exceptionally clean low-mass spectra was achieved by surface assisted laser desorption/ionization from GLAD silicon vertical posts. These posts were also found to have very high sensitivity, enabling detection of peptides at attomol concentrations. Initial optimization results showed that slanted posts had even lower desorption thresholds, providing motivation for further development of GLAD-based LDI targets.

This work has demonstrated that GLAD is a viable platform for biomolecular separations. Chromatographic and electrophoretic separations were performed for the first time using GLAD films, a versatile platform for producing GLAD-filled microfluidic devices was developed, and the efficacy of Si films in laser desorption/ionization mass spectrometry was shown. The performance of GLAD films in these three varied applications is encouraging, presenting the first step in establishing GLAD as a versatile platform for biomolecular separations and analysis.

6.2 Future Work

Integration of functionalities on one chip was part of the basis for the micro-total analysis system (lab on a chip) concept [211,212]. The ability of GLAD films to function in three separation modalities (chromatography and electrophoresis, both in-channel and planar, and mass spectrometry) immediately suggests facile integration of systems using GLAD.

The simplest, most straightforward combination is TLC coupled into mass spectrometry. UTLC plates have already been used for coupling separations into MALDI-MS [55, 213]. Silicon nanowires have been used for TLC separation of a drug mixture and were directly used for SALDI-MS [155]. Coupling TLC with MS provides a sensitive, accurate method for identifying compounds, for quantifying separations, and for increasing resolution when there are unresolved spots (i.e. multiple components

per spot). The open top-down structure of GLAD films and the ultra-thin layer make most of the analyte accessible to the surface. This, combined with the strong performance of both GLAD UTLC plates and SALDI substrates, suggests that GLAD may be an ideally suited technology for integration of TLC and MS.

A further extension of this concept is the integration of GLAD films with digital microfluidics [214]. In digital microfluidics [215, 216], individual droplets are manipulated on a hydrophobic/hydrophilic surface using electric fields. This enables precise handling of very small volumes, and can be used for a range of processes including contained microreactions, dilutions, and DNA amplification (polymerase chain reaction). GLAD films could be easily integrated into these systems thanks to the planar topography, and would add a versatile tool to such a chip, providing a platform for high-surface area microreactions, affinity capture units (concentrators), planar separations, and coupling into mass spectrometers. One can envision such a device where products from a reaction are offloaded onto a GLAD section for either separation or mass spectrometry, or both.

The tunable porosity and varied morphologies and materials available makes GLAD an appropriate platform for investigating other separations. Protein separations are presently still a challenge due to their complex structure and behaviour and large size distribution; this is the kind of problem that GLAD porous media may be able to address [214]. As with thin layer chromatography, microfluidic separations

could then be integrated with mass spectrometry for proteomics analysis [217]. Small pores (nanopores) are easily made with GLAD. The ease with which such pores can be made and with which their architecture can be engineered is a strong advantage of GLAD devices over other strategies for creating porous separation devices. This warrants further investigation into on- and off-chip separation of small biomolecules.

Graded density films, where the pore size varies along the surface of the substrate [218], coupled with careful design that appropriately directs the different-sized molecules without pore clogging, could potentially widen the range of molecules that can be resolved in a single separation. Figure 6.1 illustrates a possible design for such a device. Analyte mixture flows through the device via electrophoretic or pressure driven migration. The mixture would conceivably first separate due to the changing height of the channel; clogging is mitigated by the continous movement of molecules diagonal to the flow, permitting obstacles to be cleared by migration back into a less confined space. A second degree of separation would occur due to the porous bed by a size-exclusion principle [94, 219]; the graded density film will present appropriate porosity in the bed for each 'channel' of molecule sizes. The 'staircase' ceiling is not essential for a functioning device, but would add a defined degree of separation while simultaneously helping minimize clogging in the device. The elements for a device like this have already been demonstrated: the graded porosity across the plane of the substrate was developed by Krause *et al.* [218], the porous bed

size exclusion chromatography concept proven by Sano *et al.* [94] while the process for fabricating channels with multiple heights was demonstrated in Chapter 4 (e.g. ref. Fig. 4.10). With careful design of the channel heights and graded density film porosity distribution, separation of a large variety of mixtures on the same chip may be achievable on such a device.

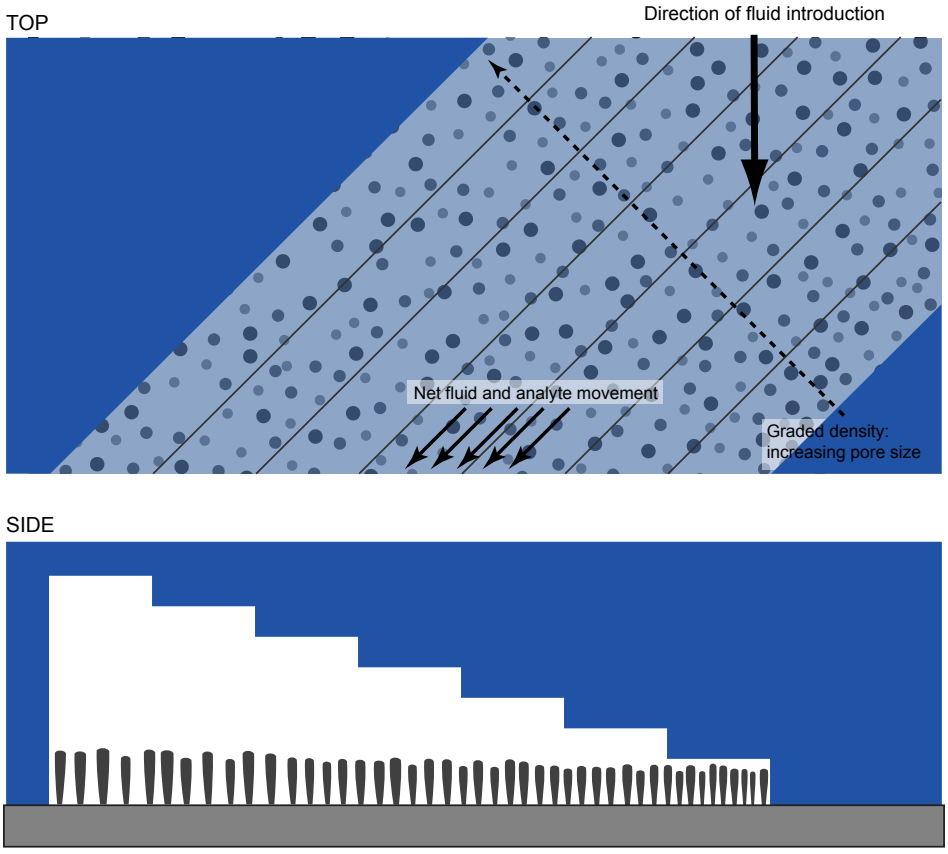

Figure 6.1: Schematic of a potential graded-density GLAD film-based flow-through size exclusion chromatography separation device.

There is still substantial room for improvement in the performance and understanding of SALDI substrates. The LDI process is still not completely understood,

making it difficult to engineer optimized structures. The literature is still divided on what is and is not important, and how it all works. GLAD can be used to study materials and structures independently in a much more controlled manner than is available with other methods. Further insight into LDI mechanisms could be gained by guided, directed study of the performance of GLAD-deposited LDI structures of different materials and architectures. This in turn could lead to purposeful engineering of optimized LDI materials. In addition, extension to substrates suitable for visible and IR wavelength lasers should be straightforward with the tunable properties of GLAD films, and would also be a valuable contribution [194].

The process presented here for integrating nanostructures into microchannels is versatile but is also time-consuming as a result of the required sacrificial etch. This is especially true when compared to other, existing processes such as self-assembled colloidal spheres or porous polymer monolith films. The main advantage of the GLAD-based system, then, is not the fabrication process (which is merely a byproduct of the film fabrication requirements), but rather the type of three dimensional structures and anisotropic morphologies constructed from a range of materials that can be built into channels. We have not yet identified an application that takes advantage of these benefits. A significant breakthrough for GLAD-based microfluidic devices will occur when the right team identifies such an application where the unique advantages of GLAD structures can be leveraged for novel or enhanced microfluidic systems.

REFERENCES

[1] F. S. Collins, E. S. Lander, J. Rogers, R. H. Waterston, and I. Conso, "Finishing the euchromatic sequence of the human genome," *Nature* **431**, 931–945 (2004). (Cited on page 1.)

[2] S. Levy and R. L. Strausberg, "Individual genomes diversify," *Nature* **456**, 6 (2008). (Cited on page 1.)

[3] M. L. Metzker, "Emerging technologies in DNA sequencing," *Genome Research* **15**, 1767–1776 (2005). (Cited on page 1.)

[4] J. West, M. Becker, S. Tombrink, and A. Manz, "Micro total analysis systems: Latest achievements," *Analytical Chemistry* **80**, 4403–4419 (2008). (Cited on pages 2 and 45.)

[5] G. M. Whitesides, "The origins and the future of microfluidics," *Nature* **442**, 368 (2006). (Cited on pages 2 and 45.)

[6] J. Fu, P. Mao, and J. Han, "Artificial molecular sieves and filters: a new paradigm for biomolecule separation," *Trends in Biotechnology* **26**, 311–320 (2008). (Cited on pages 2 and 45.)

[7] M. R. Mohamadi, L. Mahmoudian, N. Kaji, M. Tokeshi, H. Chuman, and Y. Baba, "Nanotechnology for genomics & proteomics," *Nano Today* **1**, 38–45 (2006). (Cited on page 2.)

[8] O. Gustafsson and J. P. Kutter, *Microfluidic technologies for miniaturized analysis systems*, Springer Verlag (2007). (Cited on page 2.)

[9] J. Nilsson, M. Evander, B. Hammarström, and T. Laurell, "Review of cell and particle trapping in microfluidic systems," *Analytica Chimica Acta* **649**, 141–157 (2009). (Cited on page 2.)

[10] M. De Pra, W. Th. Kok, and P. J. Schoenmakers, "Topographic structures and chromatographic supports in microfluidic separation devices," *Journal of Chromatography* **1184**, 560–572 (2008). (Cited on pages 2 and 45.)

[11] J. C. T. Eijkel and A. van den Berg, "The promise of nanotechnology for separation devices – from a top-down approach to nature-inspired separation devices," *Electrophoresis* **27**, 677–685 (2006). (Cited on pages 2 and 45.)

[12] A.-M. Siouffi, "From paper to planar: 60 years of thin layer chromatography," *Sep. Purif. Rev.* **34**, 155–180 (2005). (Cited on pages 3 and 23.)

[13] M. T. Taschuk, M. M. Hawkeye, and M. J. Brett, *Handbook of Deposition Technologies for Films and Coatings: Science, Applications and Technology*, ch. Glancing Angle Deposition, Elsevier Inc., Oxford, United Kingdom, third ed. (2010). (Cited on pages 6, 16, 17, 19, 48, and 117.)

[14] K. Robbie, L. J. Friedrich, S. K. Dew, T. Smy, and M. J. Brett, "Fabrication of thin films with highly porous microstructures," *Journal of Vacuum Science and Technology A* **13**, 1032–1035 (1995). (Cited on page 6.)

[15] K. Robbie, M. J. Brett, and A. Lakhtakia, "First thin film realization of a helicoidal bianisotropic medium," *Journal of Vacuum Science and Technology A* **13**, 2991–2993 (1995). (Cited on page 6.)

[16] J. A. Thornton, "High rate thick film growth," *Annual Review of Material Science* **7**, 239–260 (1977). (Cited on pages x, 7, and 8.)

[17] S. A. Campbell, *The Science and Engineering of Microelectronic Fabrication*, Oxford University Press (2001). (Cited on pages 7 and 10.)

[18] D. A. Gish, M. A. Summers, and M. J. Brett, "Morphology of periodic nanostructures for photonic crystals grown by glancing angle deposition," *Photonics and Nanostructures - Fundamentals and Applications* **4**, 23 – 29 (2006). (Cited on pages 11 and 16.)

[19] K. Robbie and M. J. Brett, "Sculptured thin films and glancing angle deposition: growth mechanics and applications," *Journal of Vacuum Science and Technology A* **15**, 1460–1465 (1997). (Cited on pages 11 and 101.)

[20] M. M. Hawkeye and M. J. Brett, "Glancing angle deposition: Fabrication, properties, and applications of micro-and nanostructured thin films," *Journal of Vacuum Science & Technology A* **25**, 1317–1335 (2007). (Cited on pages 11, 19, 96, and 101.)

[21] D. Vick, T. Smy, and M. J. Brett, "Growth behavior of evaporated porous thin films," *Journal of Material Research* **17**, 2904–2911 (2002). (Cited on pages 15, 32, and 88.)

[22] T. Karaback, J. P. Singh, Y.-P. Zhao, G.-C. Wang, and T.-M. Lu, "Scaling during shadowing growth of isolated nanocolumns," *Physical Review B* **69**, 125408 (2003). (Cited on page 15.)

[23] M. Pelliccione and T.-M. Lu, "Self-shadowing in ballistic fan formation from point seeds," *Physical Review B* **75**, 245431 (2007). (Cited on page 16.)

[24] F. Tang, T. Karaback, L. Li, M. Pelliccione, G.-C. Wang, and T.-M. Lu, "Power-law scaling during shadowing growth of nanocolumns by oblique angle deposition," *Journal of Vacuum Science and Technology* **25**, 160–166 (2007). (Cited on page 16.)

[25] S. Mukherjee and D. Gall, "Power law scaling during physical vapor deposition under extreme shadowing conditions," *Journal of Applied Physics* **107**, 084301 (2010). (Cited on page 16.)

[26] M. O. Jensen and M. J. Brett, "Porosity engineering in glancing angle deposition thin films," *Applied Physics A* **80**, 763–768 (2005). (Cited on pages 16, 25, 32, and 48.)

[27] M. Malac, R. F. Egerton, B. Dick, and M. J. Brett, "Fabrication of submicrometer regular arrays of pillars and helices," *Journal of Vacuum Science and Technology B* **17**, 2671–2674 (1999). (Cited on page 17.)

[28] M. O. Jensen and M. J. Brett, "Periodically structured glancing angle deposition thin films," *IEEE Transactions on Nanotechnology* **4**, 269–277 (2005). (Cited on pages 17, 18, and 88.)

[29] M. O. Jensen, *Photonic Crystal Engineering in Glancing Angle Deposition Thin Films*, PhD thesis, University of Alberta, Edmonton, Alberta, Canada (2005). (Cited on pages xi and 18.)

[30] M. A. Summers, *Periodic thin films by glancing angle deposition*, PhD thesis, University of Alberta, Edmonton, Alberta, Canada (2009). (Cited on pages xi and 18.)

[31] M. J. Brett and M. M. Hawkeye, "New materials at a glance," *Science* **319**, 1192–1193 (2008). (Cited on page 19.)

[32] J. J. Steele and M. J. Brett, "Nanostructure engineering in porous columnar thin films: recent advances," *Journal of Materials Science: Materials in Electronics* **18**, 367–379 (2007). (Cited on page 19.)

[33] A. Lakhtakia and R. Messier, *Sculptured thin films: nanoengineered morphology and optics*, SPIE – The International Society for Optical Engineering (2005). (Cited on page 19.)

[34] Y. Zhao, D. Ye, G.-C. Wang, and T.-M. Lu, "Designing nanostructures by glancing angle deposition," in [*Proceedings of SPIE 2003*], **5219**, 59–73, SPIE, Bellingham, WA (2003). (Cited on pages 19, 96, and 101.)

[35] M. M. Hawkeye and M. J. Brett, "Narrow bandpass optical filters fabricated with one-dimensionally periodic inhomogeneous thin films," *Journal of Applied Physics* **100**, 044322 (2006). (Cited on pages 19 and 81.)

[36] J. J. Steele, A. C. van Popta, M. M. Hawkeye, J. C. Sit, and M. J. Brett, "Nanostructured gradient index optical filter for high-speed humidity sensing," *Sensors & Actuators: B. Chemical* **120**, 213–219 (2006). (Cited on pages 19, 81, and 96.)

[37] M. A. Summers, K. Tabunshchyk, A. Kovalenko, and M. J. Brett, "Fabrication of 2D-3D photonic crystal heterostructures by glancing angle deposition," *Photonics and Nanostructures - Fundamentals and Applications* **7**, 76–84 (2009). (Cited on page 19.)

[38] K. D. Harris, D. Vick, E. J. Gonzalez, T. Smy, K. Robbie, and M. J. Brett, "Porous thin films for thermal barrier coatings," *Surface & Coatings Technology* **138**, 185–191 (2001). (Cited on pages 19 and 96.)

[39] J. N. Broughton and M. J. Brett, "Electrochemical capacitance in manganese thin films with chevron microstructure," *Electrochemical and Solid-State Letters* **5**, A279–A282 (2002). (Cited on pages 19 and 96.)

[40] K. D. Harris, J. R. McBride, K. E. Nietering, and M. Brett, "Fabrication of porous platinum thin films for hydrocarbon sensor applications," *Sensors and Materials* **13**, 225–234 (2001). (Cited on pages 19 and 96.)

[41] A. Dolatshahi-Pirouz, C. P. Pennisi, S. Skeldal, M. Foss, J. Chevallier, V. Zachar, P. Andreasen, K. Yoshida, and F. Besenbacher, "The influence of glancing angle deposited nano-rough platinum surfaces on the adsorption of fibrinogen and the proliferation of primary human fibroblasts," *Nanotechnology* **20**, 095101 (2009). (Cited on page 19.)

[42] M. Demirel, E. So, T. Ritty, S. Naidu, and A. Lakhtakia, "Fibroblast cell attachment and growth on nanoengineered sculptured thin films," *Journal of Biomedical Materials Research Part B: Applied Biomaterials* **81B**, 219 – 223 (2006). (Cited on page 19.)

[43] J. J. Steele, M. T. Taschuk, and M. J. Brett, "Nanostructured metal oxide thin films for humidity sensors," *IEEE Sensors Journal* **8**, 1422–1429 (2008). (Cited on pages 19 and 48.)

[44] D. A. Gish, F. Nsiah, M. T. McDermott, and M. Brett, "Localized surface plasmon resonance biosensor using silver nanostructures fabricated by glancing angle deposition," *Analytical Chemistry* **79**, 4228–4232 (2007). (Cited on page 19.)

[45] J. Fu and Y. Zhao, "Au nanoparticle based localized surface plasmon resonance substrates fabricated by dynamic shadowing growth," *Nanotechnology* **21**, 175303 (2010). (Cited on page 20.)

[46] S. Shanmukh, J. Driskell, Y. Zhao, R. Dluhy, and R. A. Tripp, "Rapid and sensitive detection of respiratory virus molecular signatures using a silver nanorod array SERS substrate," *Nano Letters* **6**, 2630–2636 (2006). (Cited on pages 20 and 48.)

[47] I. Abdulhalim, A. Karabchevsky, C. Patzig, B. Rauschenbach, B. Fuhrmann, E. Eltzov, R. Marks, J. Xu, F. Zhang, and A. Lakhtakia, "Surface-enhanced fluorescence from metal sculptured thin films with application to biosensing in water," *Applied Physics Letters* **94**, 063106 (2009). (Cited on pages 20 and 48.)

[48] P. Kao, N. A. Malvadkar, M. Cetinkaya, H. Wang, D. L. Allara, and M. C. Demirel, "Surface-enhanced raman detection on metalized nanostructured

poly(p-xylylene) films," *Advanced Materials* **20**, 3562 – 3565 (2008). (Cited on page 20.)

[49] L. W. Bezuidenhout and M. J. Brett, "Ultrathin layer chromatography on nanostructured thin films," *Journal of Chromatography A* **1183**, 179–185 (2008). (Cited on page 21.)

[50] C. F. Poole, "Thin-layer chromatography: challenges and opportunities," *Journal of Chromatography A* **1000**, 963–984 (2003). (Cited on pages 21 and 24.)

[51] C. F. Poole, "Chromatography," in [*Encyclopedia of Separation Science*], I. D. Wilson, ed., 40–64, Academic Press, Oxford (2000). (Cited on page 21.)

[52] C. F. Poole, "Planar chromatography at the turn of the century," *Journal of Chromatography A* **856**, 399–427 (1999). (Cited on pages 23 and 24.)

[53] H. E. Hauck, O. Bund, W. Fischer, and M. Schulz, "Ultra-thin layer chromatography (UTLC) - a new dimension in thin-layer chromatography," *Journal of Planar Chromatography* **14**, 234–236 (2001). (Cited on page 23.)

[54] H. E. Hauck and M. Schulz, "Ultrathin-layer chromatography," *Journal of Chromatogric Science* **40**, 1–3 (2002). (Cited on pages 23 and 40.)

[55] P. K. Salo, H. Salomies, K. Harju, R. A. Ketola, T. Kotiaho, J. Yli-Kauhaluoma, and R. Kostiainen, "Analysis of small molecules by ultra thin-layer chromatography-atmospheric pressure matrix-assisted laser desorption/ionization mass spectrometry," *Journal of the American Society of Spectrometry* **16**, 906–915 (2005). (Cited on pages 23, 41, and 133.)

[56] M. Malac and R. F. Egerton, "Observations of the microscopic growth mechanism of pillars and helices formed by glancing-angle thin-film deposition," *Journal of Vacuum Science and Technology A* **19**, 158–166 (1999). (Cited on page 32.)

[57] M. Suzuki and Y. Taga, "Numerical study of the effective surface area of obliquely deposited thin films," *Journal of Applied Physics* **90**, 5599–5605 (2001). (Cited on page 36.)

[58] K. M. Krause, M. T. Taschuk, K. D. Harris, D. A. Rider, N. G. Wakefield, J. C. Sit, J. M. Buriak, M. Thommes, and M. J. Brett, "Surface area characterization

of obliquely deposited metal oxide nanostructured thin films," *Langmuir* **24**, 4368 (2010). (Cited on pages 36, 39, 47, 63, 79, 88, 102, and 112.)

[59] S. Nyiredy, "Planar chromatographic method development using the PRISMA optimization system and flow charts," *Journal of Chromatographic Science* **40**, 1–11 (2002). (Cited on page 39.)

[60] L. R. Snyder, "Classification of the solvent properties of common liquids," *Journal of Chromatographic Science* **16**, 223–234 (1978). (Cited on page 39.)

[61] K. M. Krause, D. W. Vick, M. Malac, and M. J. Brett, "Taking a little off the top: Nanorod array morphology and growth studied by focused ion beam tomography," *Langmuir* **26**, 17558–17567 (2010). (Cited on page 40.)

[62] C. F. Poole and S. K. Poole, "Multidimensionality in planar chromatography," *Journal of Chromatography A* **703**, 573–612 (1995). (Cited on page 41.)

[63] G. E. Morlock, C. Oellig, L. W. Bezuidenhout, M. J. Brett, and W. Schwack, "Miniaturized planar chromatography using office peripherals," *Analytical Chemistry* **82**, 2940–2946 (2010). (Cited on page 41.)

[64] S. R. Jim, M. T. Taschuk, G. E. Morlock, L. W. Bezuidenhout, W. Schwack, and M. J. Brett, "Engineered anisotropic microstructures for ultrathin-layer chromatography," *Analytical Chemistry* **82**, 5394–5356 (2010). (Cited on pages ix, 42, 43, and 48.)

[65] J. E. Clark and S. V. Olesik, "Technique for ultrathin layer chromatography using an electrospun nanofibrous stationary phase," *Analytical Chemistry* **81**, 4121–4129 (2009). (Cited on page 42.)

[66] L. W. Bezuidenhout, N. Nazemifard, A. B. Jemere, D. J. Harrison, and M. J. Brett, "Microchannels filled with diverse micro- and nanostructures fabricated by glancing angle deposition," *Lab on a Chip* **Submitted**, 1–9 (2010). (Cited on page 45.)

[67] A. van den Berg, H. G. Craighead, and P. Yang, "From microfluidic applications to nanofluidic phenomena," *Chemical Society Reviews* **39**, 899–900 (2010). (Cited on page 45.)

[68] K. Ohno, K. Tachikawa, and A. Manz, "Microfluidics: applications for analytical purposes in chemistry and biochemistry," *Electrophoresis* **29**, 4443–4453 (2008). (Cited on page 45.)

[69] N. Kaji, Y. Okamoto, M. Tokeshi, and Y. Baba, "Nanopillar, nanoball, and nanofibers for highly efficient analysis of biomolecules," *Chemical Society Reviews* . (Cited on page 45.)

[70] M. De Pra, W. De Malsche, G. Desmet, P. J. Schoenmakers, and W. Th. Kok, "Pillar-structured microchannels for on-chip liquid chromatography: Evaluation of the permeability and separation performance," *Journal of Separation Science* **30**, 1453–1460 (2007). (Cited on pages 45 and 47.)

[71] J. Fu, R. B. Schoch, A. L. Stevens, S. R. Tannenbaum, and J. Han, "A patterned anisotropic nanofluidic sieving structure for continuous-flow separation of DNA and proteins," *Nature Nanotechnology* **2**, 121–128 (2007). (Cited on pages 45, 46, and 81.)

[72] M. Cabodi, Y.-F. Chen, S. W. P. Turner, H. G. Craighead, and R. H. Austin, "Continuous separation of biomolecules by the laterally asymmetric diffusion array with out-of-plane sample injection," *Electrophoresis* **23**, 3496–3503 (2002). (Cited on page 45.)

[73] L. R. Huang, E. C. Cox, R. H. Austin, and J. C. Sturm, "Continuous particle separation through deterministic lateral displacement," *Science* **304**, 987 (2004). (Cited on pages 45 and 46.)

[74] W. D. Volkmuth and R. H. Austin, "DNA electrophoresis in microlithographic arrays," *Nature* **358**, 600–602 (1992). (Cited on page 45.)

[75] T. A. J. Duke and R. H. Austin, "Microfabricated sieve for the continuous sorting of macromolecules," *Physical Review Letters* **80**, 1552–1555 (1998). (Cited on pages 45 and 46.)

[76] K. Inatomi, S. Izuo, S. Lee, H. Ohji, and S. Shiono, "Electrophoresis of DNA in micropillars fabricated in polydimethylsiloxane," *Microelectronic Engineering* **70**, 13–18 (2003). (Cited on page 46.)

[77] Y. C. Chan, Y. K. Lee, and Y. Zohar, "High-throughput design and fabrication of an integrated microsystem," *Journal of Micromechanics and Microengineering* **16**, 699–707 (2006). (Cited on page 46.)

[78] O. Bakajin, T. A. J. Duke, J. Tegenfeldt, C. F. Chou, S. S. Chan, R. H. Austin, and E. C. Cox, "Separation of 100-kilobase DNA molecules in 10 seconds," *Analytical Chemistry* **73**, 6053–6056 (2001). (Cited on page 46.)

[79] S. Yi, K. S. Seo, and Y. H. Cho, "A DNA trapping and extraction microchip using periodically crossed electrophoresis in a micropillar array," *Sensors & Actuators: A. Physical* **120**, 429–436 (2005). (Cited on page 46.)

[80] Y. C. Chan, Y. Zohar, and Y.-K. Lee, "Effects of embedded sub-micron pillar arrays in microfluidic channels on large DNA electrophoresis," *Electrophoresis* **30**, 3242–3249 (2009). (Cited on page 46.)

[81] R. Ogawa, H. Ogawa, A. Oki, S. Hashioka, and Y. Horiike, "Fabrication of nano-pillar chips by a plasma etching technique for fast DNA separation," *Thin Solid Films* **515**, 5167–5171 (2007). (Cited on page 46.)

[82] P. S. Doyle, J. Bibette, A. Bancaud, and J.-L. Viovy, "Self-assembled magnetic matrices for DNA separation chips," *Science* **295**, 2237 (2002). (Cited on page 46.)

[83] Y. Zeng, M. He, and D. J. Harrison, "Microfluidic self-patterning of large-scale crystalline nanoarrays for high-throughput continuous DNA fractionation," *Angewandte Chemie* **120**, 6488–6491 (2008). (Cited on pages 46, 63, 64, 67, and 86.)

[84] M. Baba, T. Sano, N. Iguchi, K. Iida, T. Sakamoto, and H. Kawaura, "DNA size separation using artificially nanostructured matrix," *Applied Physics Letters* **83**, 1468 (2003). (Cited on pages 46 and 47.)

[85] N. Kaji, Y. Tezuka, Y. Takamura, M. Ueda, T. Nishimoto, H. Nakanishi, Y. Horiike, and Y. Baba, "Separation of long DNA molecules by quartz nanopillar chips under a direct current electric field," *Analytical Chemistry* **76**, 15–22 (2004). (Cited on page 46.)

[86] S. W. P. Turner, M. Cabodi, and H. G. Craighead, "Confinement-induced entropic recoil of single DNA molecules in a nanofluidic structure," *Physical Review Letters* **88**, 128103 (2002). (Cited on page 46.)

[87] M. Cabodi, S. W. P. Turner, and H. G. Craighead, "Entropic recoil separation of long DNA molecules," *Analytical Chemistry* **74**, 5169–5174 (2002). (Cited on page 46.)

[88] J. Han and H. G. Craighead, "Separation of long DNA molecules in a microfabricated entropic trap array," *Science* **288**, 1026 (2000). (Cited on pages 46 and 93.)

[89] J. Fu, P. Mao, and J. Han, "Continuous-flow bioseparations using microfabricated anisotropic nanofluidic sieving structures," *Nature Protocols* **4**, 1681–1698 (2009). (Cited on page 46.)

[90] C. F. Chou, O. Bakajin, S. W. P. Turner, T. A. J. Duke, S. S. Chan, E. C. Cox, H. G. Craighead, and R. H. Austin, "Sorting by diffusion: An asymmetric obstacle course for continuous molecular separation," *Proceedings of the National Academy of Sciences* **96**, 13762 (1999). (Cited on page 46.)

[91] L. R. Huang, E. C. Cox, R. H. Austin, and J. C. Sturm, "Tilted brownian ratchet for DNA analysis," *Analytical Chemistry* **75**, 6963–6967 (2003). (Cited on page 46.)

[92] D. W. Inglis, J. A. Davis, R. H. Austin, and J. C. Sturm, "Critical particle size for fractionation by deterministic lateral displacement," *Lab on a Chip* **6**, 655–658 (2006). (Cited on page 46.)

[93] J. Han and H. G. Craighead, "Characterization and optimization of an entropic trap for DNA separation," *Analytical Chemistry* **74**, 394–401 (2002). (Cited on page 47.)

[94] T. Sano, N. Iguchi, K. Iida, T. Sakamoto, M. Baba, and H. Kawaura, "Size-exclusion chromatography using self-organized nanopores in anodic porous alumina," *Applied Physics Letters* **83**, 4438 (2003). (Cited on pages 47, 135, and 136.)

[95] B. He, N. Tait, and F. Regnier, "Fabrication of nanocolumns for liquid chromatography," *Analytical Chemistry* **70**, 3790–3797 (1998). (Cited on page 47.)

[96] B. He, J. Ji, and F. E. Regnier, "Capillary electrochromatography of peptides in a microfabricated system," *Journal of Chromatography A* **853**, 257–262 (1999). (Cited on page 47.)

[97] B. E. Slentz, N. A. Penner, and F. E. Regnier, "Protein proteolysis and the multi-dimensional electrochromatographic separation of histidine-containing peptide fragments on a chip," *Journal of Chromatography A* **984**, 97–107 (2003). (Cited on page 47.)

[98] W. De Malsche, H. Eghbali, D. Clicq, J. Vangelooven, H. Gardeniers, and G. Desmet, "Pressure-driven reverse-phase liquid chromatography separations in ordered nonporous pillar array columns," *Analytical Chemistry* **79**, 5915–5926 (2007). (Cited on page 47.)

[99] H. Eghbali, S. Matthijs, V. Verdoold, H. Gardeniers, P. Cornelis, and G. Desmet, "Use of non-porous pillar array columns for the separation of Pseudomonas pyoverdine siderophores as an example of a real-world biological sample," *Journal of Chromatography A* **1216**, 8603–8611 (2009). (Cited on page 47.)

[100] Z. He, Y. Li, Q. Zhang, and H. Wang, "Capillary microchannel-based microreactors with highly durable ZnO/TiO_2 nanorod arrays for rapid, high efficiency and continuous-flow photocatalysis," *Applied Catalysis B: Environmental* **93**, 376–382 (2009). (Cited on page 47.)

[101] G. Chen, G. T. McCandless, R. L. McCarley, and S. A. Soper, "Integration of large-area polymer nanopillar arrays into microfluidic devices using in situ polymerization cast molding," *Lab on a Chip* **7**, 1424–1427 (2007). (Cited on pages 47, 49, and 82.)

[102] B. J. Hindson, D. M. Gutierrez, K. D. Ness, A. J. Makarewicz, T. R. Metz, U. S. Setlur, W. B. Benett, J. M. Loge, J. B. W. Colston, P. S. Francis, N. W. Barnett, and J. M. Dzenitis, "Development of an automated DNA purification module using a microfabricated pillar chip," *The Analyst* **133**, 248–255 (2008). (Cited on page 47.)

[103] T. Nissilä, L. Sainiemi, S. Franssila, and R. Ketola, "Fully polymeric integrated microreactor/electrospray ionization chip for on-chip digestion and mass spectrometric analysis," *Sensors and Actuators B* **143**, 414–420 (2009). (Cited on page 47.)

[104] G. K. Kiema, M. O. Jensen, and M. J. Brett, "Glancing angle deposition thin film microstructures for microfluidic applications," *Chemistry of Materials* **17**, 4046–4048 (2005). (Cited on pages 47 and 48.)

[105] K. D. Harris, M. J. Brett, T. J. Smy, and C. Backhouse, "Microchannel surface area enhancement using porous thin films," *Journal of The Electrochemical Society* **147**, 2002–2006 (2000). (Cited on pages 47, 48, and 54.)

[106] K. Kaminska, T. Brown, G. Beydaghyan, and K. Robbie, "Vacuum evaporated porous silicon photonic interference filters," *Applied Optics* **42**, 4212–4219 (2003). (Cited on page 48.)

[107] A. K. Kar, P. Morrow, X. Tang, T. C. Parker, H. Li, J. Dai, M. Shima, and G. Wang, "Epitaxial multilayered Co/Cu ferromagnetic nanocolumns grown by oblique angle deposition," *Nanotechnology* **18**, 295702 (2007). (Cited on page 48.)

[108] A. B. Jemere, L. W. Bezuidenhout, M. J. Brett, and D. J. Harrison, "Matrix-free laser desorption/ionization mass spectrometry using silicon glad films," *Rapid Communications in Mass Spectrometry* **24**, 2305–2311 (2010). (Cited on pages 48, 90, and 96.)

[109] S. W. Turner, A. M. Perez, A. Lopez, and H. G. Craighead, "Monolithic nanofluid sieving structures for DNA manipulation," *Journal of Vacuum Science and Technology B* **16**, 3835–3840 (1998). (Cited on page 49.)

[110] D. S. Kim, H. U. Lee, N. H. Kim, K. Lee, D. Cho, and T. H. Kwon, "Fabrication of microchannel containing nanopillar arrays using micromachined AAO (anodic aluminum oxide) mold," *Microelectronic Engineering* **84**, 1532–1535 (2007). (Cited on page 49.)

[111] K.-S. Yun and E. Yoon, "Fabrication of complex multilevel microchannels in PDMS by using three-dimensional photoresist masters," *Lab on a Chip* **8**, 245–250 (2007). (Cited on page 49.)

[112] A. L. Elias, K. D. Harris, C. W. M. Bastiaansen, D. J. Broer, and M. J. Brett, "Large-area microfabrication of three-dimensional, helical polymer structures," *Journal of Micromechanics and Microengineering* **15**, 49–54 (2005). (Cited on page 54.)

[113] K. Robbie, M. J. Brett, and A. Lakhtakia, "Chiral sculptured thin films," *Nature* **384**, 616 (1996). (Cited on page 58.)

[114] M. Seto, K. Westra, and M. Brett, "Arrays of self-sealed microchambers and channels," *Journal of Materials Chemistry* **12**, 2348–2351 (2002). (Cited on page 58.)

[115] H. Leplan, B. Geenen, J. Y. Robic, and Y. Pauleau, "Residual stresses in evaporated silicon dioxide thin films: Correlation with deposition parameters and aging behavior," *Journal of Applied Physics* **78**, 962–968 (1995). (Cited on pages 59 and 60.)

[116] K. Scherer, L. Nouvelot, P. Lacan, and R. Bosmans, "Optical and mechanical characterization of evaporated sio$_2$ layers. long-term evolution," *Applied Optics* **35**, 5067–5072 (1996). (Cited on page 59.)

[117] M. R. Kupsta, M. T. Taschuk, M. J. Brett, and J. C. Sit, "Overcoming cap layer cracking for glancing-angle deposited films," *Submitted to Soild Thin Films* (2010). (Cited on page 61.)

[118] N. Nazemifard, S. Bhattacharjee, J. H. Masliyah, and D. J. Harrison, "DNA dynamics in nanoscale confinement under asymmetric pulsed field electrophoresis," *Angewandte Chemie* **122**, 3398–3401 (2010). (Cited on pages xiv, 64, 67, and 68.)

[119] G. B. Salieb-Buegelaar, K. D. Dorfman, A. van den Berg, and J. C. T. Eijkel, "Electrophoretic separation of dna gels and nanostructures," *Lab on a Chip* **9**, 2508–2523 (2009). (Cited on pages xiv, 65, 66, and 67.)

[120] L. R. Huang, J. O. Tegenfeldt, J. J. Kraeft, J. C. Sturm, R. H. Austin, and E. C. Cox, "A DNA prism for high-speed continuous fractionation of large DNA molecules," *Nature Biotechnology* **20**, 1048–1051 (2002). (Cited on pages 67 and 86.)

[121] D. E. Haas, J. N. Quijada, S. J. Picone, and D. P. Birnie, "Effect of solvent evaporation rate on "skin" formation during spin coating of complex solutions," in [*Sol-Gel Optics V*], **3943**, 280–284, SPIE (2000). (Cited on page 77.)

[122] S. Hirasawa, Y. Saito, H. Nezu, N. Ohashi, and H. Maruyama, "Analysis of drying shrinkage and flow due to surface tension of spin-coated films on topographic substrates," *IEEE Transactions on Semiconductor Manufacturing* **10**, 438–444 (1997). (Cited on page 77.)

[123] Y.-P. Zhao and J.-G. Fan, "Clusters of bundled nanorods in nanocarpet effect," *Applied Physics Letters* **88**, 103123 (2006). (Cited on pages 82 and 118.)

[124] J. K. Kwan and J. C. Sit, "The use of ion-milling to control clustering of nanostructured, columnar thin films," *Nanotechnology* **21**, 295301 (2010). (Cited on pages 82 and 88.)

[125] J.-G. Fan, J.-X. Fu, A. Collins, and Y.-P. Zhao, "The effect of the shape of nanorod arrays on the nanocarpet effect," *Nanotechnology* **19**, 045713 (2008). (Cited on pages 82 and 118.)

[126] J. N. Lee, C. Park, and G. M. Whitesides, "Solvent compatibility of poly(dimethylsiloxane)-based microfluidic devices," *Analytical Chemistry* **75**, 6544–6554 (2003). (Cited on page 83.)

[127] N. Nazemifard, L. Wang, W. Ye, S. Bhattacharjee, J. H. Masliyah, and D. J. Harrison, "A systematic evaluation of the role of crystalline order in nanoporous materials on DNA separation," *Analytical Chemistry, submitted* . (Cited on pages 86 and 87.)

[128] N. Kaji, A. Oki, R. Ogawa, Y. Takamura, T. Nishimoto, H. Nakanishi, Y. Horiike, M. Tokeshi, and Y. Baba, "Influences of electroosmotic flows in nanopillar chips on DNA separation: Experimental results and numerical simulations," *Israel Journal of Chemistry* **47**, 161–169 (2007). (Cited on page 87.)

[129] C. Patzig, C. Khare, B. Fuhrmann, and B. Rauschenbach, "Periodically arranged Si nanostructures by glancing angle deposition on patterned substrates," *Physica Status Solidi B* **247**, 1322–1334 (2010). (Cited on page 88.)

[130] K. Dreisewerd, "The desorption process in maldi," *Chemistry Reviews* **103**, 395–425 (2003). (Cited on page 90.)

[131] R. Knochenmuss, "Ion formation mechanisms in UV-MALDI," *Analyst* **131**, 966–986 (2006). (Cited on page 90.)

[132] J. Sunner, E. Dratz, and Y.-C. Chen, "Graphite surface-assisted laser desorption/ionization time-of-flight mass spectrometry of peptides and proteins from liquid solutions," *Analytical Chemistry* **67**, 4335–4332 (1995). (Cited on pages 91, 92, 93, and 94.)

[133] J. Wei, J. M. Buriak, and G. Siuzdak, "Desorption/ionization mass spectrometry on porous silicon," *Nature* **399**, 243–246 (1999). (Cited on pages 91, 92, 95, 96, 102, 105, 111, and 113.)

[134] S. Alimpiev, A. Grechnikov, J. Sunner, V. Karavanskii, Y. Simanovsky, S. Zhabin, and S. Nikiforov, "On the role of defects and surface chemistry for surface-assisted laser desorption ionization from silicon," *The Journal of Chemical Physics* **128**, 014711 (2008). (Cited on pages 92, 95, 96, 102, 105, and 113.)

[135] S. Okuno, R. Arakawa, K. Okamoto, Y. Matsui, S. Seki, T. Kozawa, S. Tagawa, and Y. Wada, "Requirements for laser-induced desorption/ionization on sub-micrometer structures," *Analytical Chemistry* **77**, 5364–5369 (2005). (Cited on pages 92, 94, 95, 96, 102, 105, 118, 122, and 123.)

[136] R. Nayak and D. R. Knapp, "Effects of thin-film structural parameters on laser desorption/ionization from porous alumina," *Analytical Chemistry* **79**, 4950–4956 (2007). (Cited on pages 92, 94, 105, 111, 117, 122, and 123.)

[137] Y. Xiao, S. T. Retterer, D. K. Thomas, J.-Y. Tao, and L. He, "Impacts of surface morphology on ion desorption in desorption ionization on porous silicon (DIOS) mass spectrometry," *Journal of Physical Chemistry C* **113**, 3076–3083 (2009). (Cited on pages 92, 95, 105, and 117.)

[138] B. N. Walker, J. A. Stolee, D. L. Pickel, S. T. Retterer, and A. Vertes, "Tailored silicon nanopost arrays for resonant nanophotonic ion production," *Journal of Physical Chemistry C* **114**, 4835–4840 (2010). (Cited on pages 92, 95, 105, and 122.)

[139] K. P. Law, "Laser desorption/ionization mass spectrometry on nanostructured semiconductor substrates: DIOS and QuickMass," *International Journal of Mass Spectrometry* **290**, 72–84 (2010). (Cited on pages 92 and 94.)

[140] V. Jokinen, S. Aura, L. Luosujärvi, L. Sainiemi, T. Kotiaho, S. Franssila, and M. Baumann, "Surface assisted laser desorption/ionization on two-layered amorphous silicon coated hybrid nanostructures," *Journal of the American Society for Mass Spectrometry* **20**, 1723–1730 (2009). (Cited on pages 92, 93, 94, 95, 105, 122, 123, and 124.)

[141] Y. Chen, H. Chen, A. Aleksandrov, and T. M. Orlando, "Roles of water, acidity, and surface morphology in surface-assisted laser desorption/ionization of

amino acids," *Journal of Physical Chemistry C* **112**, 6953–6960 (2008). (Cited on page 92.)

[142] K. P. Law, "Surface-assisted laser desorption/ionization mass spectrometry on nanostructured silicon substrates prepared by iodine-assisted etching," *International Journal of Mass Spectrometry* **290**, 47–59 (2010). (Cited on page 92.)

[143] W. G. Lewis, Z. Shen, M. G. Finn, and G. Siuzdak, "Desorption/ionization on silicon (DIOS) mass spectrometry: background and applications," *International Journal of Mass Spectrometry* **226**, 107–116 (2003). (Cited on pages 92 and 95.)

[144] G. Luo, Y. Chen, G. Siuzdak, and A. Vertes, "Surface modification and laser pulse length effects on internal energy transfer in DIOS," *Journal of Physical Chemistry B* **109**, 24450–24456 (2005). (Cited on page 92.)

[145] I. V. Shmigol, S. A. Alekseev, O. Y. Lavrynenko, N. S. Vasylieva, V. N. Zaitsev, D. Barbier, and V. A. Pokrovskiy, "Chemically modified porous silicon for laser desorption/ionization mass spectrometry of ionic dyes," *Journal of Mass Spectrometry* **44**, 1234–1240 (2008). (Cited on page 92.)

[146] I. V. Shmigol, S. A. Alekseev, O. Y. Lavrynenko, V. N. Zaitsev, D. Barbier, and V. A. Pokrovskiy, *Nanomaterials and Supramolecular Structures*, ch. 4. Surface-assisted laser desorption/ionization of low molecular organic substances on oxidized porous silicon, 45–50, Springer Science and Business Media B. V. (2009). (Cited on pages 92 and 94.)

[147] S. Tuomikoski, K. Huikko, K. Grigoras, P. Östman, R. Kostiainen, M. Baumann, J. Abian, T. Kotiaho, and S. Franssila, "Preparation of porous n-type silicon sample plates for desorption/ionization on silicon mass spectrometry (DIOS-MS)," *Lab on a Chip* **2**, 247–253 (2002). (Cited on pages 92, 95, and 111.)

[148] R. A. Kruse, X. Li, P. W. Bohn, and J. V. Sweedler, "Experimental factors controlling analyte ion generation in laser desorption/ionization mass spectrometry on porous silicon," *Analytical Chemistry* **73**, 3639–3645 (2001). (Cited on pages 92, 94, 95, 96, 102, 105, 113, 114, 117, and 122.)

[149] S. Alimpiev, S. Nikiforov, V. Karavanskii, T. Minton, and J. Sunner, "On the mechanism of laser-induced desorption-ionization of organic compounds from etched silicon and carbon surfaces," *The Journal of Chemical Physics* **115**, 1891–1901 (2001). (Cited on pages 92, 96, and 122.)

[150] Q. Zhang, H. Zou, Z. Guo, Q. Zhang, X. Chen, and J. Ni, "Matrix-assisted laser desorption/ionization mass spectrometry using porous silicon and silica gel as matrix," *Rapid Communications in Mass Spectrometry* **15**, 217–223 (2001). (Cited on pages 92, 93, 113, 117, and 123.)

[151] Z. Shen, J. J. Thomas, C. Averbuj, K. M. Broo, M. Engelhard, J. E. Crowell, M. G. Finn, and G. Siuzdak, "Porous silicon as a versatile platform for laser desorption/ionization mass spectrometry," *Analytical Chemistry* **73**, 612–619 (2001). (Cited on pages 92, 95, 96, 102, and 113.)

[152] J. Li, C. Lu, X. K. Hu, X. Yang, A. V. Loboda, and R. H. Lipson, "Nanostructured porous silicon by laser assisted electrochemical etching," *International Journal of Mass Spectrometry* **285**, 137–142 (2009). (Cited on pages 92 and 95.)

[153] J. D. Cuiffi, D. J. Hayes, S. J. Fonash, K. N. Brown, and A. D. Jones, "Desorption/ionization mass spectrometry using deposited nanostructured silicon films," *Analytical Chemistry* **73**, 1292–1295 (2001). (Cited on pages 92, 95, 102, and 111.)

[154] N. H. Finkel, B. G. Prevo, O. D. Velev, and L. He, "Ordered silicon nanocavity arrays in surface-assisted desorption/ionization mass spectrometry," *Analytical Chemistry* **77**, 1088–1095 (2005). (Cited on pages 92, 95, 105, and 117.)

[155] E. P. Go, J. V. Apon, G. Luo, A. Saghatelian, R. H. Daniels, V. Sahi, R. Dubrow, B. F. Cravatt, A. Vertes, and G. Siuzdak, "Desorption/ionization on silicon nanowires," *Analytical Chemistry* **77**, 1641–1646 (2005). (Cited on pages 92, 95, 105, 111, and 133.)

[156] G. Luo, Y. Chen, H. Daniels, R. Dubrow, and A. Vertes, "Internal energy transfer in laser desorption/ionization from silicon nanowires," *Journal of Physical Chemistry B* **110**, 13381–13386 (2006). (Cited on pages 92, 95, and 122.)

[157] B. N. Walker, T. Razunguzwa, M. Powell, R. Knochenmuss, and A. Vertes, "Nanophotonic ion production from silicon microcolumn arrays," *Angewandte Chemie Int. Ed.* **48**, 1669–1672 (2009). (Cited on pages 92 and 95.)

[158] J. A. Stolee, Y. Chen, and A. Vertes, "High-energy fragmentation in nanophotonic ion production by laser-induced silicon microcolumn arrays," *Journal of Physical Chemistry C* **114**, 5574–5581 (2010). (Cited on pages 92 and 95.)

[159] Y. Chen and A. Vertes, "Adjustable fragmentation in laser desorption/ionization from laser-induced silicon microcolumn arrays," **78**, 5835–5844 (2006). (Cited on pages 92 and 95.)

[160] G. Piret, H. Drobecq, Y. Coffinier, O. Melnyk, and R. Boukherroub, "Matrix-free laser desorption/ionization mass spectrometry on silicon nanowire arrays prepared by chemical etching of crystalline silicon," *Langmuir* **26**, 1354–1361 (2010). (Cited on pages 93, 95, 105, 111, and 123.)

[161] S. Xu, Y. Li, H. Zou, J. Qiu, Z. Guo, and B. Guo, "Carbon nanotubes as assisted matrix for laser desorption/ionization time-of-flight mass spectrometry," *Analytical Chemistry* **75**, 6191–6195 (2003). (Cited on page 93.)

[162] M. Najam-ul haq, M. Rainer, C. W. Huck, P. Hausberger, H. Kraushaar, and K. B. Günther, "Nanostructured diamond-like carbon on digital versatile disc as a matrix-free target for laser desorption/ionization mass spectrometry," *Analytical Chemistry* **80**, 7467–7472 (2008). (Cited on page 93.)

[163] H. Kawasaki, N. Takahashi, H. Fujimori, K. Okumura, T. Watanabe, C. Matsumura, S. Takemine, T. Nakano, and R. Arakawa, "Functionalized pyrolytic highly oriented graphite polymer film for surface-assisted laser desorption/ionization mass spectrometry in environmental analysis," *Rapid Communications in Mass Spectrometry* **23**, 3323–3332 (2009). (Cited on page 93.)

[164] A. M. Dattelbaum, R. K. Hicks, J. Shelley, A. T. Koppisch, and S. Iyer, "Surface assisted laser desorptionâĂŞionization mass spectrometry on patterned nanoporous silica thin films," *Microporous and mesoporous materials* **114**, 192–200 (2008). (Cited on pages 93, 117, and 122.)

[165] A. Górecka-Drzazga, S. Bargiel, R. Walczak, J. A. Dziuban, A. Kraj, T. Dylag, and J. Silberring, "Desorption/ionization mass spectrometry on porous silicon dioxide," *Sensors & Actuators: B. Chemical* **103**, 206–212 (2004). (Cited on pages 94, 111, and 123.)

[166] C.-Y. Lo, J.-Y. Lin, W.-Y. Chen, C.-T. Chen, and Y.-C. Chen, "Surface-assisted laser desorption/ionization mass spectrometry on titania nanotube arrays," *Journal of the American Society for Mass Spectrometry* **19**, 1014–1020 (2008). (Cited on pages 94 and 123.)

[167] C.-t. Chen and Y.-c. Chen, "Desorption/ionization mass spectrometry on nanocrystalline titania solâĂŞ gel-deposited films," *Rapid Communications in Mass Spectrometry* **18**, 1956–1964 (2004). (Cited on page 94.)

[168] E. T. Castellana, R. C. Gamez, M. E. Gómez, and D. H. Russell, "Longitudinal surface plasmon resonance based gold nanorod biosensors for mass spectrometry," *Langmuir* **26**, 6066–6070 (2010). (Cited on page 94.)

[169] L. C. Chen, J. Yonehama, T. Ueda, H. Hori, and K. Hiraoka, "Visible-laser desorption/ionization on gold nanostructures," *Journal of Mass Spectrometry* **42**, 346–353 (2007). (Cited on pages 94 and 105.)

[170] H. Kawasaki, T. Sugitani, T. Watanabe, T. Yonezawa, H. Moriwaki, and R. Arakawa, "Layer-by-layer self-assembled mutilayer films of gold nanoparticles for surface-assisted laser desorption/ionization mass spectrometry," *Analytical Chemistry* **80**, 7524–7533 (2008). (Cited on pages 94 and 105.)

[171] H. Kawasaki, T. Yonezawa, T. Watanabe, and R. Arakawa, "Platinum nanoflowers for surface-assisted laser desorption/ionization mass spectrometry of biomolecules," *Journal of Physical Chemistry C* **111**, 16278–16283 (2007). (Cited on pages 94 and 111.)

[172] T. Yao, H. Kawasaki, T. Watanabe, and R. Arakawa, "Effectiveness of platinum particle deposition on silicon surfaces for surface-assisted laser desorption/ionization mass spectrometry of peptides," *International Journal of Mass Spectrometry* **291**, 145–151 (2010). (Cited on page 94.)

[173] T. Yalcin and L. Li, "Cobalt coated substrate for matrix-free analysis of small molecules by laser desorption/ionization mass spectrometry," *Applied Surface Science* **256**, 1309–1312 (2009). (Cited on page 94.)

[174] T. Seino, H. Sato, A. Yamamoto, A. Nemoto, M. Torimura, and H. Tao, "Matrix-free laser desorption/ionization-mass spectrometry using self-assembled germanium nanodots," *Analytical Chemistry* **79**, 4827–4832 (2007). (Cited on page 94.)

[175] W. J. Shin, J. H. Shin, J. Y. Song, and S. Y. Han, "Effects of ZnO nanowire length on surface-assisted laser desorption/ionization of small molecules," *Journal of the American Society for Mass Spectrometry* **21**, 989–992 (2010). (Cited on pages 94 and 105.)

[176] K. A. Stumpo and D. H. Russell, "Anion effects on ionization efficiency using gold nanoparticles as matrices for LDI-MS," *Journal of Physical Chemistry C* **113**, 1642–1647 (2009). (Cited on page 94.)

[177] E. T. Castellana and D. H. Russell, "Tailoring nanoparticle surface chemistry to enhance laser desorption ionization of peptides and proteins," *Nano Letters* **7**, 3023–3025 (2007). (Cited on page 94.)

[178] J. A. Mclean, K. A. Stumpo, and D. H. Russell, "Size-selected (2-10 nm) gold nanoparticles for matrix assisted laser desorption/ionization of peptides," *Journal of the American Chemical Society* **127**, 5304–5305 (2005). (Cited on page 94.)

[179] T. Yonezawa, H. Kawasaki, A. Tarui, T. Watanabe, R. Arakawa, T. Shimada, and F. Mafuné, "Detailed investigation on the possibility of nanoparticles of various metal elements for surface-assisted laser desorption/ionization mass spectrometry," *Analytical Sciences* **25**, 339–345. (Cited on page 94.)

[180] S. Cha and E. S. Yeung, "Colloidal graphite-assisted laser desorption/ionization mass spectrometry and ms^n of small molecules. 1. imaging of cerebrosides directly from rat brain tissue," **79**, 2373–2385 (2007). (Cited on page 94.)

[181] M. V. Ugarov, T. Egan, D. V. Khabashesku, J. A. Schultz, H. Peng, V. N. Khabashesku, H. Furutani, K. S. Prather, H.-w. J. Wang, S. N. Jackson, and A. S. Woods, "Maldi matrices for biomolecular analysis based on functionalized carbon nanomaterials," *Analytical Chemistry* **76**, 6734–6742 (2004). (Cited on page 94.)

[182] T.-c. Chiu, L.-c. Chang, C.-k. Chiang, and H.-t. Chang, "Determining estrogens using surface-assisted laser desorption/ionization mass spectrometry with silver nanoparticles as the matrix," *Journal of the American Society for Mass Spectrometry* **2008**, 1343–1346 (2008). (Cited on page 94.)

[183] X. Wen, S. Dagan, and V. H. Wysocki, "Small-molecule analysis with silicon-nanoparticle-assisted laser desorption/ionization mass spectrometry," *Analytical Chemistry* **79**, 434–444 (2007). (Cited on page 94.)

[184] T. Yalcin, W. E. Wallace, C. M. Guttman, and L. Li, "Metal powder substrate-assisted laser desorption/ionization mass spectrometry for polyethylene analysis," *Analytical Chemistry* **74**, 4750–4756 (2002). (Cited on page 94.)

[185] S. Taira, K. Kitajima, H. Katayanagi, and E. Ichiishi, "Manganese oxide nanoparticle-assisted laser desorption/ionization mass spectrometry for medical applications," *Science and Technology Advanced Materials* **10**, 034602 (2009). (Cited on page 94.)

[186] C.-T. Chen and Y.-c. Chen, "Fe_3O_4/TiO_2 core/shell nanoparticles as affinity probes for the analysis of phosphopeptides using TiO_2 surface-assisted laser desorption/ionization mass spectrometry," *Analytical Chemistry* **77**, 5912–5919 (2005). (Cited on page 94.)

[187] T. Watanabe, H. Kawasaki, T. Yonezawa, and R. Arakawa, "Surface-assisted laser desorption/ionization mass spectrometry (saldi-ms) of low molecular weight organic compounds and synthetic polymers using zinc oxide (ZnO) nanoparticles," *Journal of Mass Spectrometry* **43**, 1063–1071 (2008). (Cited on page 94.)

[188] S. K. Kailasa and H.-f. Wu, "Multifunctional ZrO_2 nanoparticles and ZrO_2-SiO_2 nanorods for improved MALDI-MS analysis of cyclodextrins , peptides , and phosphoproteins," *Analytical and Bioanalytical Chemistry* **396**, 1115–1125 (2010). (Cited on page 94.)

[189] S. A. Trauger, E. P. Go, Z. Shen, J. V. Apon, B. . Compton, E. S. P. Bouvier, M. G. Finn, and G. Siuzdak, "High sensitivity and analyte capture with desorption/ionization mass spectrometry on silylated porous silicon," *Analytical Chemistry* **76**, 4484–4489 (2004). (Cited on pages 95 and 111.)

[190] E. P. Go, W. Uritboonthai, J. V. Apon, S. A. Trauger, A. Nordstrom, G. O'Maille, S. M. Brittain, E. C. Peters, and G. Siuzdak, "Selective metabolite and peptide capture/mass detection using fluorous affinity tags," *Journal of Proteome Research* **6**, 1492–1499 (2007). (Cited on page 95.)

[191] T. R. Northen, O. Yanes, M. T. Norten, D. Marrinucci, W. Uritboonthai, J. Apon, S. L. Golledge, A. Nordström, and G. Siuzdak, "Clathrate nanostructures for mass spectrometry," *Nature* **449**, 1033–1036 (2007). (Cited on pages 95 and 111.)

[192] C. S. Lee, E. M. Kim, S. H. Lee, M. S. Kim, Y. K. Kim, and B. G. Kim, "Enhancement of analyte ionization in desoprtion/ionization on porous silicon (DIOS)-mass spectrometry (MS)," *Biotechnology and Bioprocess Engineering* **10**, 212–217 (2005). (Cited on pages 95, 102, 105, and 113.)

[193] L. Buckberry and S. C. Bayliss, "Porous silicon as a biomaterial," *Materials World* **7**, 213 (1999). (Cited on page 95.)

[194] D. S. Peterson, "Matrix-free methods for laser desorption/ionization mass spectrometry," *Mass Spectrometry Reviews* **26**, 19–34 (2007). (Cited on pages 96, 112, and 137.)

[195] M. P. Stewart and J. M. Buriak, "Chemical and biological applications of porous silicon technology," *Advanced Materials* **12**, 859–869 (2000). (Cited on page 96.)

[196] G. K. Kiema, M. J. Colgan, and M. J. Brett, "Dye sensitized solar cells incorporating obliquely deposited titanium oxide layers," *Solar Energy Materials & Solar Cells* **85**, 321–331 (2005). (Cited on page 96.)

[197] J. J. Steele, J. P. Gospodyn, J. C. Sit, and M. J. Brett, "Impact of morphology on high-speed humidity sensor performance," *IEEE Sensors Journal* **6**, 24–27 (2006). (Cited on page 96.)

[198] C. Buzea, G. Beydaghyan, C. Elliot, and K. Robbie, "Control of power law scaling in the growth of silicon nanocolumn pseudo-regular arrays deposited by glancing angle deposition," *Nanotechnology* **16**, 1986 (2005). (Cited on page 102.)

[199] C. Buzea, K. Kaminska, G. Beydaghyan, T. Brown, C. Elliott, C. Dean, and K. Robbie, "Thickness and density evaluation for nanostructured thin films by glancing angle deposition," *Journal of Vacuum Science and Technology B* **23**, 2545–2552 (2005). (Cited on page 102.)

[200] V. V. Laiko, N. I. Taranenko, V. D. Berkout, B. D. Musselman, and V. M. Doroshenko, "Atmospheric pressure laser desorption/ionization on porous silicon," *Rapid Communications in Mass Spectrometry* **16**, 1737–1742 (2002). (Cited on page 105.)

[201] G. Credo, H. Hewitson, C. Benevides, and E. S. P. Bouvier, "Development of a porous silicon product for small molecule mass spectrometry," in [*Materials Research Society Symposium Proceedings*], **808**, 471–476, MRS (2004). (Cited on page 105.)

[202] A. Bertazzo, C. V. L. Costa, G. Allegri, D. Favretto, and P. Traldi, "Application of matrix-assisted laser desorption/ionization mass spectrometry to the detection

of melanins formed from dopa and dopamine," *Journal of Mass Spectrometry* **34**, 922–929 (1999). (Cited on page 106.)

[203] A. Kraj, T. Dylag, A. Gorecka-Drzazga, S. Bargiel, J. A. Dziuban, and J. Silberring, "Desorption/ionization on silicon for small molecules: A promising alternative to MALDI TOF," *Acta Biochimica Polonica* **50**, 783–787 (2003). (Cited on page 106.)

[204] X. Wen, S. Dagan, and V. H. Wysocki, "Small-molecule analysis with silicon-nanoparticle-assisted laser desorption/ionization mass spectrometry," *Analytical Chemistry* **79**, 434–444 (2007). (Cited on page 111.)

[205] S. Tsoi, E. Fok, J. C. Sit, and J. G. C. Veinot, "Superhydrophobic, high surface area, 3-D SiO_2 nanostructures through siloxane-based surface functionalization," *Langmuir* **20**, 10771–10774 (2004). (Cited on page 111.)

[206] S. Tsoi, E. Fok, J. C. Sit, and J. G. C. Veinot, "Surface functionalization of porous nanostructured metal oxide thin films fabricated by glancing angle deposition," *Chemical Materials* **18**, 5260 (2006). (Cited on page 111.)

[207] S. R. Kasi and M. Liehr, "Vapor phase hydrocarbon removal for Si processing," *Applied Physics Letters* **57**, 2095 (1990). (Cited on page 114.)

[208] M. Ouyang, C. Yuan, R. J. Muisener, A. Boulares, and J. T. Koberstein, "Conversion of some siloxane polymers to silicon oxide by UV/ozone photochemical processes," *Chemical Materials* **12**, 1591 (2000). (Cited on page 114.)

[209] B. L. Zink, R. Pietri, and F. Hellman, "Thermal conductivity and specific heat of thin-film amorphous silicon," *Physical Review Letters* **96**, 05592 (2006). (Cited on page 126.)

[210] F. Cardarelli, "Materials handbook," (2008). (Cited on page 126.)

[211] D. J. Harrison, A. Manz, Z. Fan, H. Lüdi, and H. M. Widmer, "Capillary electrophoresis and sample injection systems integrated on a planar glass chip," *Analytical Chemistry* **64**, 1926–1932 (1992). (Cited on page 133.)

[212] A. Manz, D. J. Harrison, E. M. J. Verpoorte, J. C. Fettinger, A. Paulus, H. Lüdi, and H. M. Widmer, "Planar chips technology for miniaturization and integration of separation techniques into monitoring systems: Capillary electrophore-

sis on a chip," *Journal of Chromatography* **593**, 253–258 (1992). (Cited on page 133.)

[213] B. Fuchs, R. Süß, A. Nimptsch, and J. Schiller, "MALDI-TOF-MS directly combined with TLC: a review of the current state," *Chromatographia* **69**, S95–S105 (2009). (Cited on page 133.)

[214] *Personal communication with Dr. Abebaw B. Jemere*. (Cited on page 134.)

[215] M. J. Jebrail and A. R. Wheeler, "Let's get digital: digitizing chemical biology with microfluidics," *Current Opinion in Chemical Biology* , Article in Press (2010). (Cited on page 134.)

[216] R. B. Fair, "Digital microfluidics: is a true lab-on-a-chip possible?," *Microfluidics and Nanofluidics* **3**, 245–281 (2007). (Cited on page 134.)

[217] J. Lee, S. A. Soper, and K. K. Murray, "Microfluidics with MALDI analysis for proteomics – a review," *Analytica Chimica Acta* **649**, 180–190 (2009). (Cited on page 135.)

[218] K. M. Krause and M. J. Brett, "Spatially graded nanostructured chiral films as tunable circular polarizers," *Advanced Functional Materials* **18**, 3111–3118 (2008). (Cited on page 135.)

[219] J. Janča, "Particle size separations," in [*Encyclopedia of Separation Science*], I. D. Wilson, ed., 217 – 220, Academic Press, Oxford (2000). (Cited on page 135.)